ERRATA

Page 70, line 6: Change line-per-inch to line-per-mm.

Page 153, line 3: Change (2.6) to (A.6).

Page 153, line 8: Change (2.10) to (A.10).

Page 156, line 5: Change enthalpy to entropy.

Page 156, line 6: Change enthalpy to entropy.

ENGINEERING RESEARCH INSTITUTE
THE UNIVERSITY OF MICHIGAN
ANN ARBOR

THE PRODUCTION OF VERY HIGH TEMPERATURES IN THE SHOCK TUBE WITH AN APPLICATION TO THE STUDY OF SPECTRAL LINE BROADENING

AFOSR TN-56-150
ASTIA Document No. AD 86309

Eugene Bonner Turner

Supervisor
Otto Laporte

Project 2189

DEPARTMENT OF THE AIR FORCE
AIR RESEARCH AND DEVELOPMENT COMMAND
PHYSICS DIVISION, AIR FORCE OFFICE OF SCIENTIFIC RESEARCH
CONTRACT NO. AF 18(600)-983, PROJECT NO. R-357-40-6

May 1956

This report has also been submitted as a dissertation in partial fulfillment of the requirements for the degree of Doctor of Philosophy in The University of Michigan, 1956.

PREFACE

In June, 1952, it was announced by the Shock-Tube Laboratories of both Cornell University and The University of Michigan that high-temperature spectra could be obtained from strong shocks.

This constitutes the first major report giving complete experimental techniques and results since the inception of the project in October, 1953.

It is believed that the work is of interest to the physicist, to the missile engineer, and to the astronomer. For the first time it has become possible to reach, in the laboratory, well-controlled temperatures which compare with those attained on stars. The considerable interest this subject is currently arousing is demonstrated by the great amount of research which is being started in this field by many laboratories all over the country.

It is intended to continue this work.

Otto Laporte

ACKNOWLEDGMENTS

The author wishes to express his gratitude to Professor Otto Laporte for suggesting the study of luminous shock waves and for his valuable assistance, and to Professor Lawrence H. Aller for his cooperation and helpful advice.

The author wishes to thank his colleagues, namely, Alan C. Kolb, for many stimulating discussions, and Lowell R. Doherty, without whose assistance the work on hydrogen line broadening could not have been done.

The author also wishes to express his gratitude to the Linde Air Products Co. for their generous gift of rare gases.

The financial support for this research was provided by the Air Research and Development Command, Office of Scientific Research, under Contract No. AF 18(600)-983.

E. B. Turner

TABLE OF CONTENTS

LIST OF TABLES

LIST OF FIGURES

LIST OF FIGURES (Continued)

LIST OF FIGURES (Concluded)

OBJECTIVE

The objective of research under ARDC Contract No. AF 18(600)-983 is the study of the hydrodynamics of and the spectra behind very strong shock waves produced in a shock tube.

ABSTRACT

A small rectangular shock tube has been constructed expressly for the production of very strong shock waves in the rare gases. The tube is vacuum tight and driver gas pressures of up to 100 atmospheres can be used. Wave-speed photographs of shock waves in the tube were made with a revolving drum camera for a large range of initial pressure ratios and the primary shock velocities were found to be considerably less than the theoretical values. The interaction of the reflected shock with the interface was studied both experimentally and theoretically. The delay time for ionization was studied in xenon, and an explanation was found for the shock front appearing as a thin luminous line.

Spectra were taken of the shock-tube luminosity and such features as lines of metallic impurities, recombination continuum, and Stark broadening of the rare-gas lines were observed. It was found that intense Balmer lines of hydrogen can be produced behind the reflected shock at the end of the tube by adding about 1% hydrogen to neon. Time-resolved spectra were made of H_β and the conditions of temperature, ion density, etc., were calculated from the measured shock velocity. Comparison with the Holtsmark theory for first-order Stark broadening showed the experimental profiles to be about 20% wider.

BIBLIOGRAPHICAL CONTROL SHEET

1. Originating agency and/or monitoring agency:

O.A.: Engineering Research Institute, The University of Michigan, Ann Arbor, Michigan
M.A.: Physics Division, Air Force Office of Scientific Research

2. Originating agency and/or monitoring agency report number:

O.A.: Project 2189-2-T
M.A.: OSR Technical Note 56-150

3. Title and classification of title: THE PRODUCTION OF VERY HIGH TEMPERATURES IN THE SHOCK TUBE WITH AN APPLICATION TO THE STUDY OF SPECTRAL LINE BROADENING. (UNCLASSIFIED)

4. Personal author: Turner, Eugene Bonner

5. Date of report: May, 1956

6. Pages: 170 + 13 preliminary

7. Illustrative material: 42 figures, 5 tables

8. Prepared for Contract No.: AF 18(600)-983

9. Prepared for Project Code and/or No.: R-357-40-6

10. Security classification: UNCLASSIFIED

11. Distribution limitations: None

12. Abstract: A small rectangular shock tube has been constructed expressly for the production of very strong shock waves in the rare gases. The tube is vacuum tight and driver gas pressures of up to 100 atmospheres can be used. Wave-speed photographs of shock waves in the tube were made with a revolving drum camera for a large range of initial pressure ratios and the primary shock velocities were found to be considerably less than the theoretical values. The interaction of the reflected shock with the interface was studied both experimentally and theoretically. The delay time for ionization was studied in xenon, and an explanation was found for the shock front appearing as a thin luminous line.

Spectra were taken of the shock-tube luminosity and such features as lines of metallic impurities, recombination continuum, and Stark broadening of the rare-gas lines were observed. It was found that intense Balmer lines of hydrogen can be produced behind the reflected shock at the end of the tube by adding about 1% hydrogen to neon. Time-resolved spectra were made of H_β and the conditions of temperature, ion density, etc., were calculated from the measured shock velocity. Comparison with the Holtsmark theory for first-order Stark broadening showed the experimental profiles to be about 20% wider.

DISTRIBUTION LIST FOR
CONTRACT NO. AF 18(600)-983

Agency	No. of Copies
Commander Air Force Office of Scientific Research Air Research and Development Command ATTN: SROPP P.O. Box 1395 Baltimore 3, Maryland	5
Commander Wright Air Development Center ATTN: WCOSI-3 Wright-Patterson Air Force Base Ohio	4
Commander Air Force Cambridge Research Center ATTN: Technical Library L. G. Hanscom Field Bedford, Massachusetts	1
Commander Rome Air Development Center ATTN: RCSST-4 Griffiss Air Force Base Rome, New York	1
Director, Office for Advanced Studies Air Force Office of Scientific Research Air Research and Development Command P.O. Box 2035 Pasadena 2, California	1
Commander European Office Air Research and Development Command 60 rue Ravenstein Brussels, Belgium (Air Mail)	4
Chief Document Service Center Knott Building Dayton 2, Ohio	5
Director of Research and Development Headquarters, USAF Washington 25, D. C.	1
Chief of Naval Research Department of the Navy ATTN: Code 421 Washington 25, D. C.	1
Director, Naval Research Laboratory ATTN: Technical Information Officer Washington 25, D. C.	1
Director, Research and Development Division General Staff Department of the Army Washington 25, D. C.	1
Chief, Physics Branch U. S. Atomic Energy Commission 1901 Constitution Avenue, NW Washington 25, D. C.	1
U. S. Atomic Energy Commission Technical Information Service P.O. Box 62 Oak Ridge, Tennessee	1
National Bureau of Standards Library Room 203, Northwest Building Washington 25, D. C.	1
National Science Foundation 2144 California Street Washington 25, D. C.	1
Director, Office of Ordnance Research Box CM, Duke Station Durham, North Carolina	1
Chairman, Research and Development Board Pentagon Building Washington 25, D. C.	1

DISTRIBUTION LIST (Continued)

Agency	No. of Copies
Office of Technical Services Department of Commerce Washington 25, D. C.	1
Commander Western Development Division Air Research and Development Command ATTN: WDSIT P.O. Box 262 Inglewood, California	1
Commander Hq, Air Force Special Weapons Center Kirtland Air Force Base Albuquerque, New Mexico	1
Dr. W. A. Wildhack, Chief Office of Basic Instrumentation National Bureau of Standards Washington 25, D. C.	1
Professor H. Margenau Physics Department Yale University New Haven, Connecticut	1
Professor E. Gross Department of Physics Syracuse University Syracuse 10, New York	1
Dr. Peter C. Bergmann Department of Physics Syracuse University Syracuse 10, New York	1
Dr. P. Kusch Department of Physics Columbia University New York 27, New York	1
Dr. E. Montroll Institute for Fluid Mechanics and Applied Mathematics University of Maryland College Park, Maryland	1
Dr. Roland Meyerott Rand Corporation 1700 Main Street Santa Monica, California	1
Dr. Edward F. Greene Department of Chemistry Brown University Providence 12, Rhode Island	1
Dr. A. Hertzberg Cornell Aeronautical Laboratory, Inc. 4455 Genesee Street Buffalo 21, New York	1
Dr. Hans Griem Physics Department University of Maryland College Park, Maryland	1
Dr. R. G. Fowler Physics Department University of Oklahoma Nonnan, Oklahoma	1
Dr. Zack I. Slawsky U. S. Naval Ordnance Laboratory Silver Spring 19, Maryland	1
Dr. Raymond J. Emrich Department of Physics Lehigh University Bethlehem, Pennsylvania	1
Dr. B. Strömgren Yerkes Observatory Williams Bay, Wisconsin	1
Dr. Otto Struve Department of Astronomy University of California Berkeley, California	1
Dr. Graydon Synder Poulter Laboratories Stanford Research Institute Menlo Park, California	1

DISTRIBUTION LIST (Continued)

Agency	No. of Copies
Dr. J. Evans Upper Air Research Laboratory Sacramento Peak, New Mexico	1
Dr. Donald H. Menzel Harvard College Observatory Cambridge, Massachusetts	1
Dr. Lyman Spitzer Department of Astronomy Princeton University Princeton, New Jersey	1
Dr. J. Greenstein Department of Astronomy California Institute of Technology Pasadena, California	1
Dr. Marshall Wrubel Kirkwood Observatory Indiana University Bloomington, Indiana	1
The Shock Tube Laboratory Pennsylvania State College State College, Pennsylvania	1
Dr. Henry Nagamatsu General Electric Research Laboratory Schenectady, New York	1
Guggenheim Aeronautical Laboratory California Institute of Technology Pasadena, California	1
Dr. S. S. Penner California Institute of Technology Pasadena, California	1
Dr. Robert N. Hollyer Applied Physics Laboratory The Johns Hopkins University 8621 Georgia Avenue Silver Spring, Maryland	1
Alan C. Kolb Navy Department Naval Research Laboratory Radiation Division, Code 7410 Washington 25, D. C.	2
Dr. Bennett Kivel Research Laboratories Advanced Development Division AVCO Manufacturing Corporation 2385 Revere Beach Parkway Everett 49, Massachusetts	1
Dr. Shao-Chi Lin Research Laboratories Advanced Development Division AVCO Manufacturing Corporation 2385 Revere Beach Parkway Everett 49, Massachusetts	1
E. John Eastmond Physics Department Brigham Young University Provo, Utah	
Cornell University Graduate School of Aeronautical Engineering Ithaca, New York ATTN: Prof. Arthur Kantrowitz	1
Princeton University Palmer Physical Laboratory Princeton, New Jersey ATTN: Dr. Walter Bleakney	2
New York University Institute of Mathematics and Mechanics 45 Fourth Street University Heights New York 53, New York	1
Institute for Fluid Dynamics and Applied Mathematics University of Maryland College Park, Maryland ATTN: Dr. E. L. Resler	1
Dr. R. W. Perry ARO, Inc. Arnold Engineering Development Center Tullahoma, Tennessee	1

DISTRIBUTION LIST (Concluded)

Agency	No. of Copies	Agency	No. of Copies
Special Defense Products Dept. General Electric Company 2900 Campbell Avenue Schenectady 6, New York ATTN: Dr. Emmet Lubke	1	Mr. Jacob Pomerantz Hyperballistics Division Room 4-172 U. S. Naval Ordnance Laboratory Silver Spring, White Oak, Maryland	1
Prof. Robert B. King Norman Bridge Laboratory of Physics California Institute of Technology Pasadena, California	1	Dr. Russell E. Duff P.O. Box 1663 Los Alamos, New Mexico	2

CHAPTER I

INTRODUCTION

1. History and Development of the Luminous Shock Tube

Although the widespread use of shock tubes for hydrodynamic studies is a rather recent development, the history of shock tubes goes back to Vieille[1] who in 1899 showed experimentally that the compression wave produced by breaking a diaphragm separating regions of different pressure travels faster than sound. The shock-tube theory was developed by Kobes[2] in 1910 and extended by Schardin[3] in 1932, but several scientists who later derived the ideal shock-tube equations were unaware of this work.

The shock tube came into more general use during World War II. In England, Payman and Shepherd[4] recorded the time history of the processes in a shock tube by means of a revolving drum camera. In the United States the work on shock tubes was first carried out at Princeton University by Walter Bleakney and his co-workers. Reynolds[5] used a shock tube in 1943 for the calibration of blast gauges. In 1945 Lincoln G. Smith,[6] also working at Princeton University, studied regular and Mach reflections of shock waves in a shock tube which he brought to The University of Michigan in 1947, where parts of it are still being used. Supervision of the shock-tube laboratory at The University of Michigan was undertaken by Professor Otto Laporte in 1948. At this laboratory Geiger and Mautz[7,8,9] investigated the possibilities of using the shock tube for the study of supersonic flow patterns. Later Duff[10] considered the effects of nonconstant specific heats of various gases and Hollyer[11] showed that boundary layer and heat conduction to the walls would cause an attenuation of the primary shock wave. These reports contain extensive bibliographies of work in the field.

In April, 1952, Hollyer noticed, in connection with aerodynamic studies that were being carried on in the 2" x 7" shock tube, that a faint yellow flash could be seen at the end of the tube when a moderately strong shock wave was produced in nitrogen. The luminosity was found to be greater in argon, and when shock waves were produced by expanding hydrogen at several atmospheres pressure into krypton and xenon* at about 1 cm Hg pressure, the resulting flash was extremely brilliant and white. A brief but intensive preliminary investigation was made of the phenomena, using a revolving drum camera and a spectrograph. The results were reported at the Fluid Dynamics Division of the American Physical Society at Salt Lake City, Utah, in June, 1952.[12] These results were also published in a letter to Nature.[13]

At the same time work was going on independently at Cornell University under the direction of Arthur Kantrowitz,[14] at Los Alamos Scientific Laboratory by Shreffler and Christian,[15] and at the University of Oklahoma under Fowler.[16] Reports of research by the first two of these groups were also presented at the Salt Lake City meeting. The workers at Cornell University produced very strong shock waves in argon at low pressures by using high-pressure hydrogen and also explosive mixtures of hydrogen and oxygen as the driver gas. They studied the conductivity and the spectra of the ionized gas. At Los Alamos a solid explosive driver was used to produce a strongly luminous shock wave in argon at the local atmospheric pressure, and rather strong boundary effects were produced. Fowler, on the other hand, used a high-energy electrical discharge from a bank of condensers to

---

*We are indebted to Linde Air Products for their generous gift of these rare gases.

produce strong shock waves in hydrogen and helium at a few mm Hg pressure.

The 2" x 7" shock tube was not well suited to the production of very strong shock waves, so it was decided to build a small, strong, vacuum-tight tube expressly designed for this purpose. The construction of the tube was financed by a grant from the Regents of The University of Michigan. In November, 1953, a contract was negotiated with the Air Research and Development Command for the support of this research, and in December, 1953, the tube was assembled and fired for the first time.

2. Description of the Flow

A shock tube is essentially a tube which is divided into two chambers by a breakable diaphragm with two gases at different pressures on either side. When the diaphragm is broken, the gas in the high-pressure chamber expands into the low-pressure chamber, compressing the second gas through a shock wave which moves down the tube with constant velocity. An x-t diagram shown in Figure 1 is especially useful in describing the processes which occur following the rupture of the diaphragm. Pressures are shown when $t = 0$, when the diaphragm breaks, and at later times t_1 and t_2. The two gases are separated by an interface which, of course, must move with the flow velocity. On the left side of the interface is the gas which has expanded and thereby is cooled. This region is therefore called the "cold flow." The gas between the shock wave and the interface has been heated by compression and is termed the "hot flow." The flow in the tube is the same as if the interface were replaced by a piston moving down the tube with constant velocity. Therefore, the high-pressure gas will often be referred to as the "pusher gas." At the end of the tube the gas behind the shock is brought to rest and the kinetic energy of ordered motion is

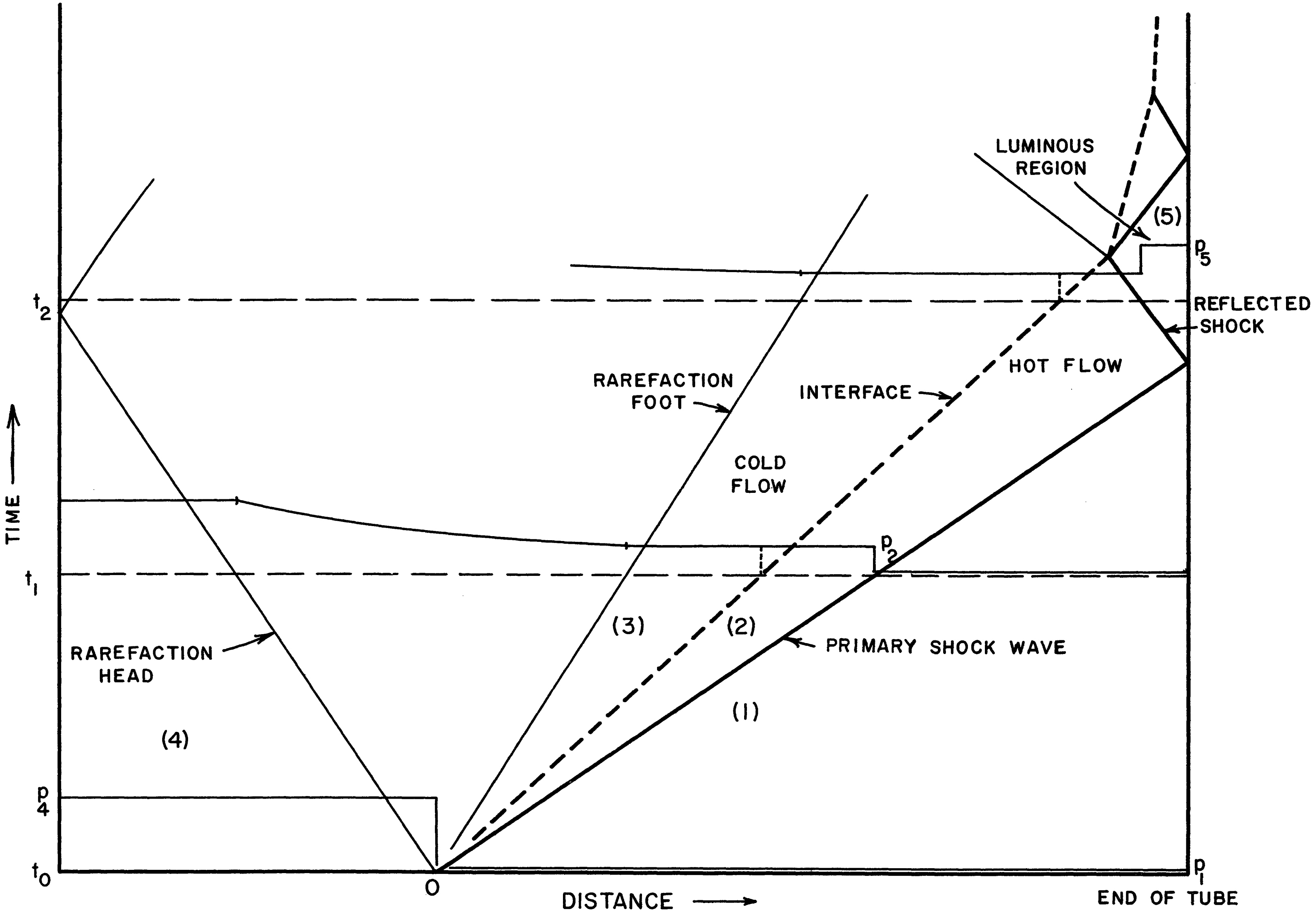

Figure 1. Distance-time diagram of processes in the shock tube.

converted to thermal motion resulting in an additional temperature rise behind the reflected shock.

It will be shown in Chapter II that the pressure ratio across the primary shock, called the shock strength, increases with the initial pressure ratio and essentially with the ratio of sound speeds of the pusher gas to the compressed gas. This can also be understood from the following reasoning. The velocity at which the pusher gas expands is proportional to its sound speed, so a gas like hydrogen, with a low molecular weight, expands much faster than nitrogen, for example. For a shock wave moving into a gas at rest the shock strength necessary to produce a given flow velocity, which must be the same as the velocity of the pusher gas, increases with a decrease in the sound speed ahead of the shock. Thus to produce strong shocks one would use a light gas in the high-pressure chamber and a heavy gas in the low-pressure chamber. To attain the maximum possible temperatures, it is best to use a gas where energy does not have to be used in exciting vibrational degrees of freedom or in the dissociation of molecules. For this reason the rare gases are usually used, of which xenon is the most efficient because it has the lowest sound speed. By shooting hydrogen into xenon, for example, a shock strength of approximately 100 can be produced with an initial pressure ratio of only 900. A somewhat higher initial pressure ratio is required to produce the same shock strength in argon. The temperatures that can be produced in the shock tube are limited mainly by the ionization potentials of the gases. Beyond a certain temperature, which is proportional to the ionization potential, increasing amounts of energy are used to ionize the gas as the temperature is increased.

Since, except for a thin boundary layer on the walls, the gas flow is one-dimensional, the temperature, density, etc., are constant across any cross section of the tube. This homogeneity is of great importance in the analysis of spectra since one does not have to use the radiative transfer integral as for arcs and sparks. The absence of a cool boundary is shown experimentally by the fact that there is no self-reversal or absorption lines in the spectra.

By the proper choice of the initial pressures and gases, almost any temperature up to about 18,000°K and any ion density from 10^{15} ions per cc to 10^{18} ions per cc can be produced. At the lower limit of ion densities the time for the establishment of thermal equilibrium may be too long, while at the upper limit the radiation of the continuum is so strong that the gas cools very rapidly. The fact that makes the shock tube unique among spectroscopic light sources is that the conditions such as temperature and ion density behind the primary and reflected shocks may be calculated from the velocity of the primary shock wave, which can be easily measured. The luminosity lasts only a few hundred microseconds since the gas cools by radiation and by turbulent diffusion of the cold gas through the interface.

3. Statement of the Problems

The development of the luminous shock tube has given the experimenter a powerful laboratory instrument for the study of many problems concerning the physics of high-temperature, partially ionized gases. It is first necessary, however, to have a thorough understanding of the hydrodynamics of very strong shock waves in the shock tube. Much work has been done on this problem by Kantrowitz and his co-workers[14,17,18] at Cornell University. They have considered theoretically the effect of ionization on the hydrodynamics of strong shock waves in argon. Experimentally they have produced very strong shock waves in argon and have studied such problems as the approach to ionization equilibrium behind the shock and the effect of radiation cooling. Agreement between the observed red shift of the argon lines behind the shock and the shift predicted from second-order Stark broadening theories for the calculated ion densities have indicated that the calculated equilibrium ion density is indeed reached if the shock is strong enough. An outstanding success of their work has been the verification of recent theories of electrical conductivity. The work at Cornell, however, has been concerned almost entirely with the primary shock wave.

Our work has been mainly concerned with the reflected shock waves at the end of the tube. It is somewhat easier to obtain high temperatures behind the reflected shocks than behind the primary shock wave, so most of the spectroscopic observations were made in this region. It was therefore necessary that the hydrodynamics of the processes at the end of the tube be understood. A theory has been developed by which the interactions of the reflected shock with the interface can be explained. Included also is a development of the hydrodynamic equations for partially ionized gases along with methods for obtaining numerical solutions. Experimentally it has been found that the predicted interactions do indeed occur, and also the effect of ionization on the reflected shock velocity has been observed.

One of the major efforts of this thesis has been the utilization of the shock tube as a spectrographic light source with which one can study spectral line broadening, etc., under known conditions of temperature and ion density. Several time-average spectra have been obtained which, although they cannot be used for quantitative measurements, do show the qualitative features of the luminosity very well. In the present work, however, shapes of spectral lines generated in the shock tube have been observed quantitatively. This has necessitated the use of a revolving drum camera for time resolution. Hydrogen lines were chosen for study because of their astrophysical importance and because of the rather large first-order Stark broadening.* A. C. Kolb, who has worked quite closely with the author, has developed a theory[19] to explain the discrepancies found with the line shapes predicted by the Holtsmark theory. The quantitative measurements of spectral line shapes have made necessary the use of a new film calibrating technique developed with the help of Mr. Lowell Doherty.

In addition to the experimental observations of the luminosity behind the reflected shocks at the end of the tube, some work has also been done on the primary shock wave. Measurements have been made on the delay time for ionization behind the shock in xenon for various shock strengths and initial xenon densities. The shock front is plainly visible as a thin luminous line even though there may be no luminosity behind the front. An experimental study was made of this phenomenon and the luminosity was found to be due to C_2 and CN bands presumably arising from the breaking up of complex molecular vapors.

A large part of the work on this thesis problem has been the design and construction of the equipment. This included the shock tube itself, which was built expressly for the production of strong shocks, the revolving drum cameras, the vacuum and pressure systems, and much auxiliary apparatus.

---

*In order to obtain high temperatures, about 1% hydrogen was mixed with neon.

The dissertation is organized as follows: Chapter II is devoted entirely to the hydrodynamic theory, including the effect of ionization and mixtures of small fractions of diatomic gases in rare gases. Chapter III contains a complete description of the experimental apparatus, including the shock tube. Chapter IV is concerned with the hydrodynamic experiments and Chapter V with the spectroscopic observations. Chapter VI contains the conclusions and a critique of the work.

4. Other Problems Amenable to Solution in the Shock Tube

As far as the author knows, this work represents the first attempt to obtain quantitative line profiles in the shock tube. So far, only the first-order Stark broadening of hydrogen has been studied and then only for one line, H_β. Therefore, there is still much work to be done on the other hydrogen lines. Also, a study of the Balmer limit and the Balmer decrement should prove fruitful. In addition, line-broadening profiles can be obtained for other gases such as argon which are subject to second-order Stark broadening.

A project which is being proposed in this laboratory in cooperation with the Astronomy Department is the measurement of relative or perhaps even absolute oscillator strengths, or f-values, of the spectral lines of gases. Since the temperature is known, the Boltzmann distribution of the atoms in the excited states can be determined and thus the oscillator strengths can be calculated from measured line intensities. If a suitable method can be found for introducing metallic impurities into the flow, one might also measure their f-values. Such atoms as carbon and sulfur can be easily introduced as CO, CO_2, SO_2, etc., which are dissociated.

Other problems which could be studied with the shock tube are the effects of magnetic field on the flow of the ionized gas, i.e., magnetohydrodynamics. Also, it has been known for some time that ionized gases have a natural frequency of oscillation called the plasma oscillation. For the range of ion densities obtained in the shock tube the wavelengths would range from about 50μ to 500μ, according to the formula of Tonks and Langmuir.[20] This is the sub-millimeter wavelength range that is just beyond the limit of electronic techniques and is in the so-called far infrared where the intensity of thermal sources is very low.

The solution of these problems is of great interest in many fields of physics and astrophysics. The broadening of spectral lines, principally hydrogen, is used for the determination of stellar atmospheres.[21] The new theory of hydrogen line broadening by A. C. Kolb has been found to fit observed absorption profiles of hot stars much better than the Holtsmark theory.* The f-values of spectral lines are of great use in the determination of stellar abundances of various elements. A study of plasma oscillations would perhaps help explain radio noise from the sun and might also offer new possibilities for the generation of submillimeter electromagnetic waves. It is obvious, therefore, that the potentialities for research in the luminous shock tube are very great indeed.

---

*See _Sky and Telescope_, XV, 4, Feb., 1956, p. 170.

CHAPTER II

HYDRODYNAMIC THEORY

1. Development of the Ideal Shock-Tube Equations

Although the hydrodynamic theory of the shock tube has been derived in several other papers,[7,8,10] it will again be given in this dissertation for two reasons. First, many of these papers are not readily accessible, and second, the theory will be given from a different point of view which can be easily extended to include the theory of reflected shock waves at the end of the tube. We will use a method developed by Courant and Friedrichs [22] (Chapter III, D) for the analysis of interactions between shock waves, interfaces, and rarefaction waves. In the first two sections of this chapter the theory will deal with ideal gases of constant specific heat. The effect of ionization on the hydrodynamics will be discussed in the third section, while the fourth section deals with mixtures of gases which may also be partially ionized.

The theory of a normal shock wave will be considered first and then the theory of a rarefaction wave. The results of the two will then be combined to give the ideal shock-tube equations. Most of the derivation of the basic equations for a normal shock wave and for a rarefaction wave will be relegated to Appendices A and B, respectively.

In Appendix A relations are derived between the flow variables on either side of a shock wave in a one-dimensional channel. The two states are designated by the subscripts (a) and (b). The relation between the absolute flow velocities u_a and u_b is then given by equation (A.11) in Appendix A as

$$u_b = u_a \pm \frac{(\mu-1)\left(\frac{p_b}{p_a}-1\right)c_a}{\sqrt{(\mu+1)\left(1+\mu\frac{p_b}{p_a}\right)}}.$$

Following Courant and Friedrichs we write this equation as

(2.1) $$u_b = u_a \pm \phi_a(p_b)$$

where

$$\phi_a(p) = \frac{(\mu-1)\left(\frac{p}{p_a}-1\right)c_a}{\sqrt{(\mu+1)\left(1+\mu\frac{p}{p_a}\right)}}.$$

The plus sign is used for a shock wave facing toward the right and the minus sign for a shock wave facing toward the left. We say a shock wave is facing toward the right if the gas moves into the front from the right and is facing toward the left if the gas enters the front from the left. Then, for example, if $p_b > p_a$ and the shock is facing toward the right, the shock wave must be moving toward (a) and the velocity of the gas is increased in the positive direction as indicated by the use of the plus sign. If, on the other hand, $p_b < p_a$, the shock wave must be moving away from state (a) into gas (b) which then must be on the right. The curve $\phi_a(p)/c_a$ is plotted in Figure 2 for $\mu = 4$, a monatomic gas, and some of the properties of $\phi(p)$ are derived in Appendix C. This function will be used both for the solution of the shock-tube problem and in the theory of the reflected shock waves at the end of the tube.

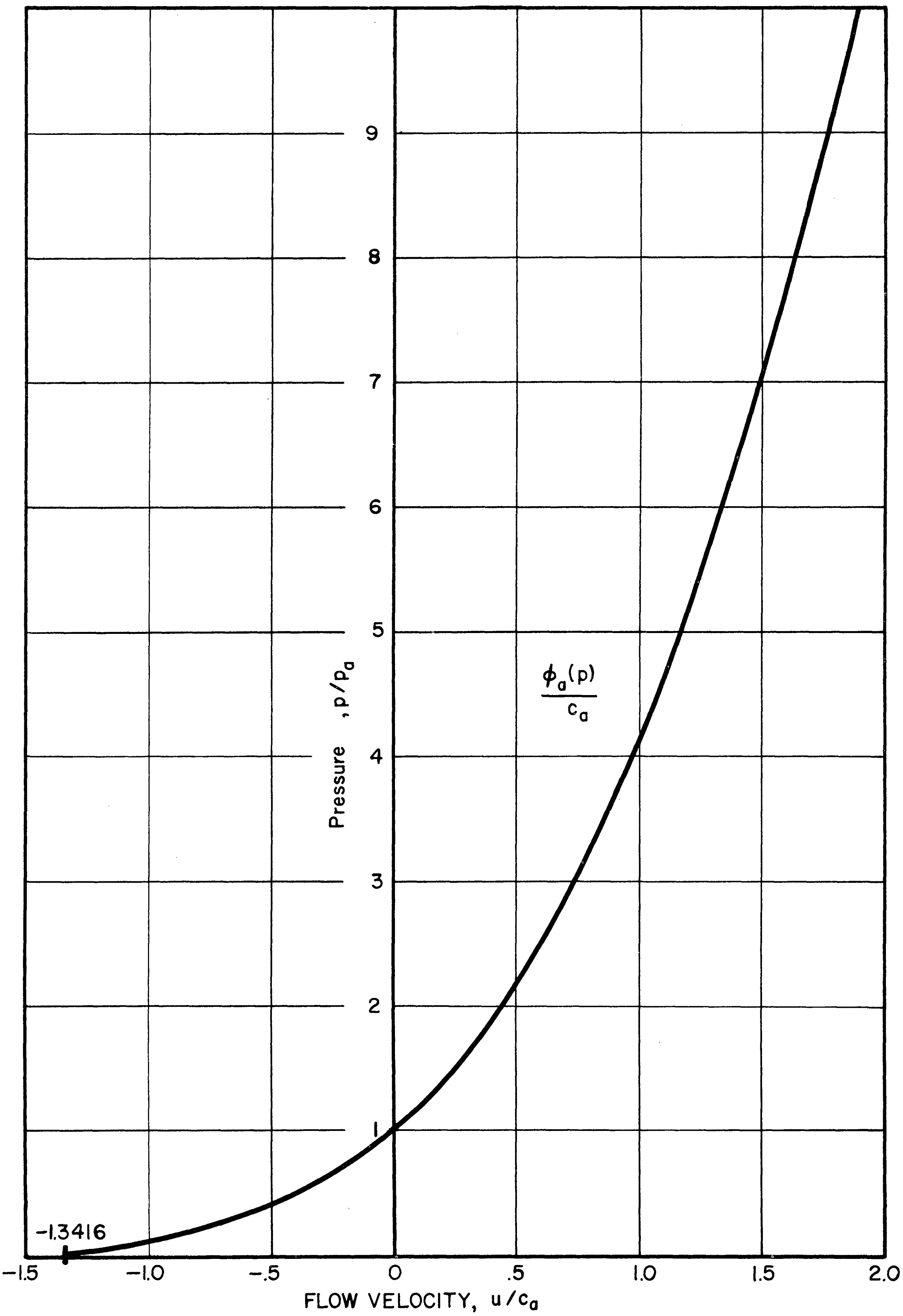

Figure 2. Plot of the flow velocity function, $\phi_a(p)$, behind a shock wave.

A function similar to $\phi(p)$ can also be derived for rarefaction waves. The preparation given in Appendix B is very brief and contains only the essentials necessary to the solution of this particular problem. Some use is made of the theory of characteristics, but their properties are not developed in general. For a more complete treatment the reader is referred to the book by Courant and Friedrichs.[22]

In Appendix B we have considered a one-dimensional rarefaction wave separating two constant states (a) and (b). From equations (B.12), (B.13), and (B.15) the flow velocity in region (b) can be expressed in the form

$$u_b = u_a \pm \psi_a(p_b) \tag{2.2}$$

where

$$\psi_a(p) = (\mu-1)c_a\left[\left(\frac{p}{p_a}\right)^{\frac{1}{\mu+1}} - 1\right].$$

According to equations (B.12) and (B.13) the plus sign should be used for a rarefaction facing to the right, and the minus sign should be used for a rarefaction facing to the left. The curve of $\psi_a(p)$ is plotted in Figure 3 for $\mu = 6$, a diatomic gas such as hydrogen. Some of the properties of this function are derived in Appendix C.

We now have sufficient preparation to proceed with the solution of the shock-tube problem, which can be stated as follows: Given that there are two gases at different pressures in a tube separated by a diaphragm, and at time $t = 0$ the diaphragm is instantaneously removed. Find the flow variables at any later time t. A graph of flow velocity vs pressure will be used for the solution of this problem. For the case of polytropic gases, the shock-tube problem can be solved analytically without the use of such

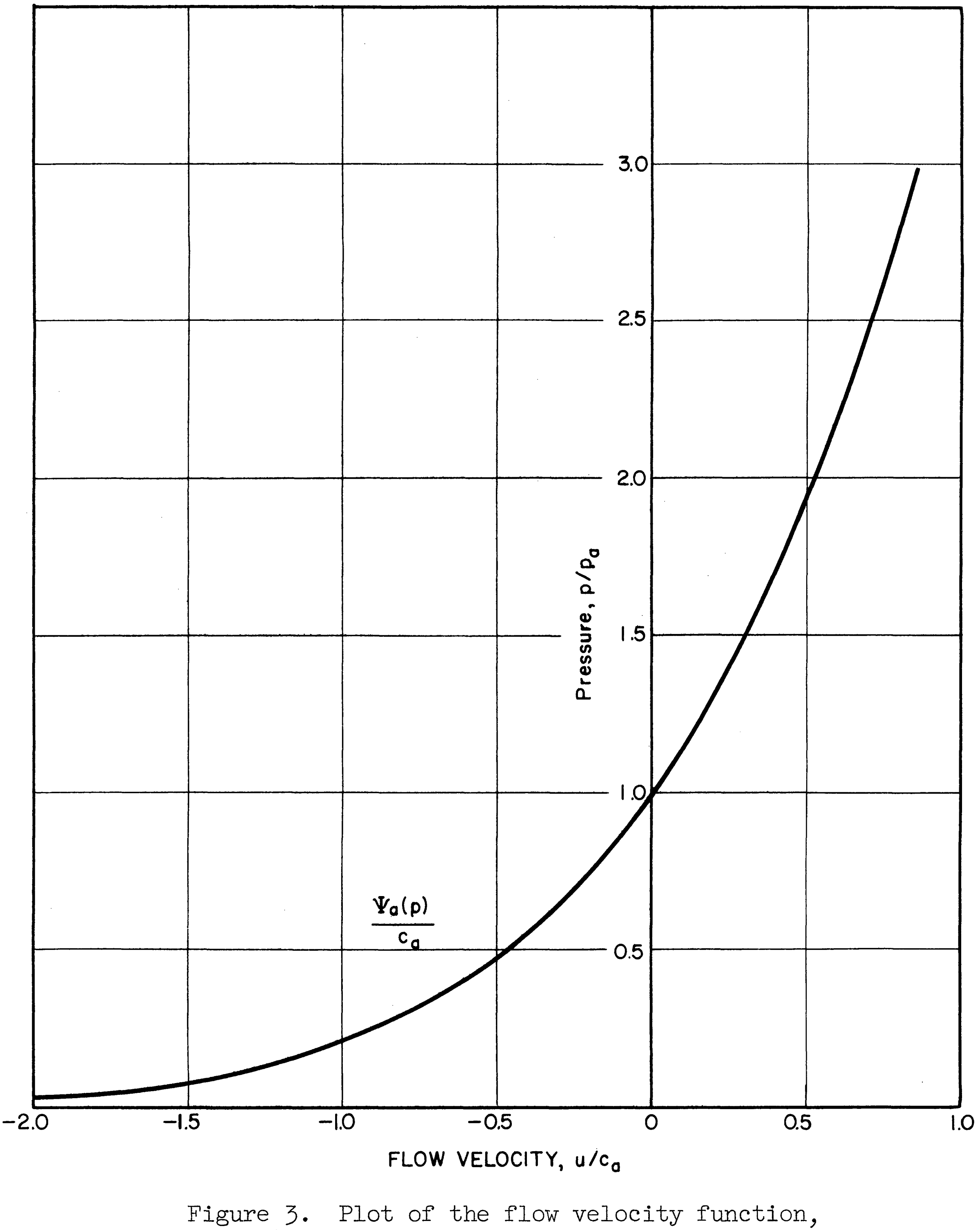

Figure 3. Plot of the flow velocity function, $\psi_a(p)$, behind a rarefaction wave.

a graph, but the graphical presentation gives more physical insight into the problem and the methods will be found very useful for the theory of the reflected shocks at the end of the tube. This graph is shown in Figure 4. Let the high-pressure chamber be at the left and the low-pressure chamber at the right. The curve $u = \phi_1(p)$ represents all states which can be reached by a shock wave moving toward the right into state (1), which is at rest. The curve $u = -\psi_4(p)$ represents all states resulting from a rarefaction moving toward the left into the high-pressure gas, which is also at rest.* Before the time $t = 0$ the pressure difference between the two gases is supported by a diaphragm. When the diaphragm is removed, however, there is a gaseous interface which must then move with the flow velocity and which can no longer support a pressure differential. If it is assumed that the diaphragm is removed instantaneously, then the gaseous interface must have an infinitesimal thickness. The character of the interface then imposes the following two boundary conditions on the flow:

$$u_2 = u_3 \quad \text{or} \quad \phi_1(p_2) = -\psi_4(p_3)$$

and

$$p_2 = p_3 \ .$$

The interface therefore is represented by the intersection of the two curves $u = \phi_1(p)$ and $u = -\psi_4(p)$. The above conditions result in the following equation:

$$\frac{(\mu_1 - 1)\left(\frac{p_2}{p_1} - 1\right)c_1}{\sqrt{(\mu_1 + 1)\left(1 + \mu_1 \frac{p_2}{p_1}\right)}} = (\mu_4 - 1)c_4\left[1 - \left(\frac{p_2}{p_4}\right)^{\frac{1}{\mu_4 + 1}}\right] . \tag{2.3}$$

---

*See Figure 1 for the numbering of the flow regions in the shock tube.

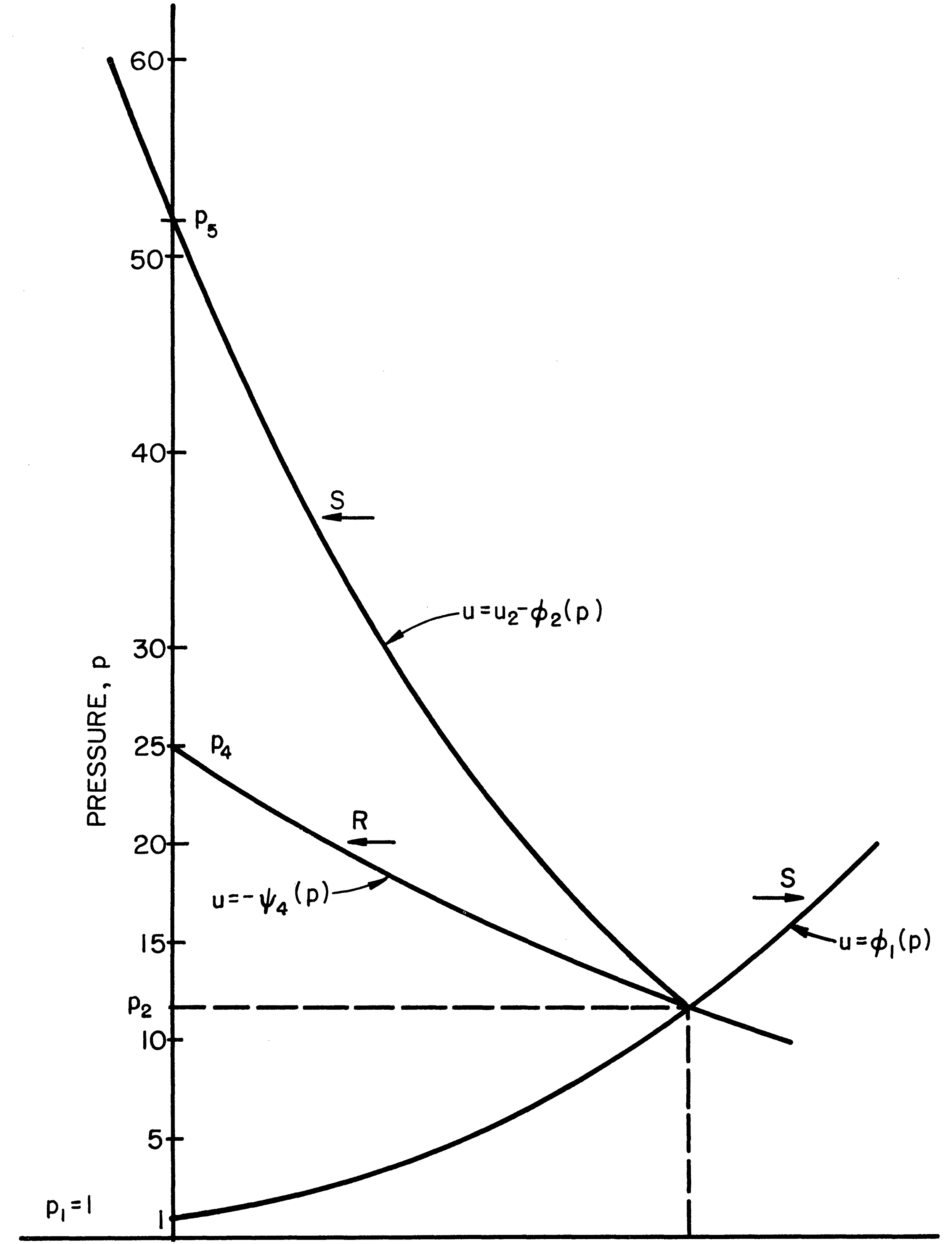

Figure 4. The pressure-velocity graph of the shock-tube problem.

Solving for p_4/p_1, one obtains

$$(2.4)\quad \frac{p_4}{p_1} = \frac{p_2}{p_1}\left[1 - \frac{(\mu_1-1)c_1}{(\mu_4-1)c_4}\cdot\frac{\left(\frac{p_2}{p_1}-1\right)}{\sqrt{(\mu_1+1)\left(1+\mu_1\frac{p_2}{p_1}\right)}}\right]^{-(\mu_4+1)},$$

This equation was derived by A. H. Taub in the report by Reynolds[5] and will hereafter be referred to as the Taub equation.

It is convenient, as a shorthand notation, to introduce the following variables:

$$Z = \frac{p_4}{p_1}, \quad y_{21} = \frac{p_2}{p_1}, \quad x_{21} = \frac{\rho_2}{\rho_1}.$$

In the case of x and y the first subscript denotes the region behind the shock and the second denotes the region ahead of the shock. Thus the Taub equation will now be written

$$(2.5)\quad Z = y_{21}\left[1 - \frac{(\mu_1-1)c_1}{(\mu_4-1)c_4}\,\frac{(y_{21}-1)}{\sqrt{(\mu_1+1)(1+\mu_1 y_{21})}}\right]^{-(\mu_4+1)}.$$

The initial pressure ratio Z required to produce a shock wave of a given strength y_{21} is very sensitive to the ratio

$$\frac{(\mu_1-1)c_1}{(\mu_4-1)c_4}.$$

As one can see from the Taub equation, the shock tube is more efficient (i.e., smaller Z required) if this ratio is small. Table I shows the sound speeds at 300°K for several gases, and in Figure 5 the initial pressure ratios required to produce given shock strengths are plotted

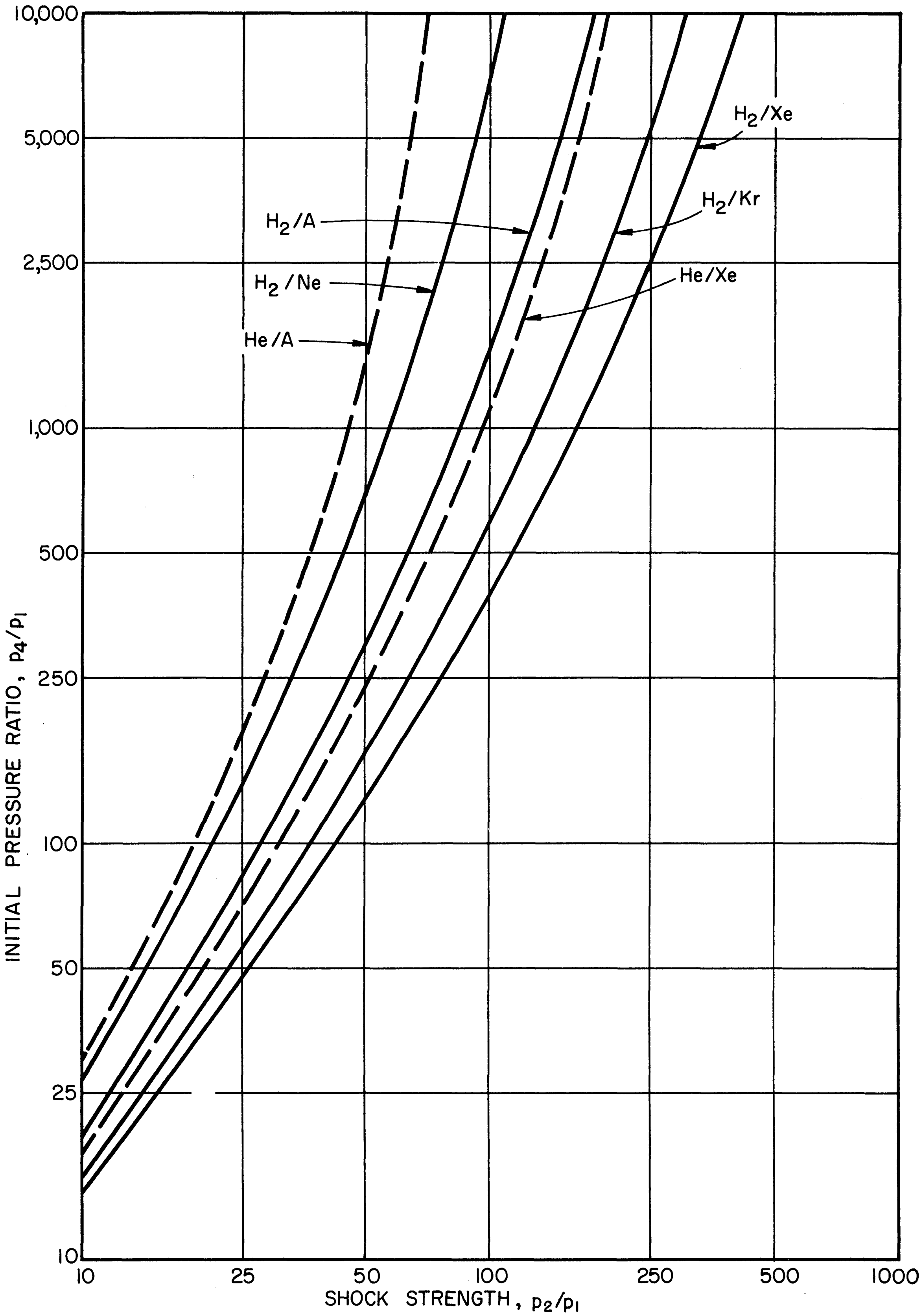

Figure 5. Theoretical shock strengths vs initial pressure ratios for several combinations of gases (neglecting ionization).

for various combinations of hydrogen and helium with the rare gases. The shock strength produced by a given initial pressure ratio (say 1000) in the rare gases goes up in the series neon, argon, krypton, and xenon. Also one sees that hydrogen is a considerably more efficient driver gas than helium.

Table I. Molecular Weights and Sound Speeds of Various Gases

Gas	Molecular Weight	Sound Speed at 300°K
H_2	2.016	131,600 cm/sec
N_2	28.016	35,300
He	4.003	102,000
Ne	20.183	45,400
A	39.944	32,250
Kr	83.7	22,300
Xe	131.3	17,800

The maximum theoretical shock strength is limited because the velocity of the expanding high-pressure gas can be no greater than $(\mu_4 - 1)c_4$ for an infinite pressure ratio [see equation (2.2)]. In the Taub equation above, if Z is set equal to infinity, the bracket must be zero. Then the maximum theoretical shock strength is the solution to the equation.

$$(2.6) \qquad \frac{(\mu_1-1)c_1}{(\mu_4-1)c_4}\,\frac{(y_{21}-1)}{\sqrt{(\mu_1+1)(1+\mu_1 y_{21})}} = 1.$$

This value is given for several combinations of gases in Table II. This table shows that the maximum shock strength increases with the series neon, argon, krypton, xenon; that a hydrogen driver gas gives higher maximum shock strengths than helium; and that like gases in the high- and low-

Table II. Maximum Theoretical Shock Strengths

High-Pressure Gas	Low-Pressure Gas	Max. Theoretical y_{21}
H_2	Ne	467
H_2	A	925
H_2	Kr	1935
H_2	Xe	3036
He	A	200
He	Xe	657
N_2	N_2	44
A	A	22.2

pressure chambers give rather low shock strengths. An explosive mixture of hydrogen and oxygen used as a driver gas (described by Resler, Lin, and Kantrowitz[14]) can have a sound speed 67 percent greater than hydrogen and therefore is somewhat more efficient.

2. The Reflected Shock Waves

As we have previously explained in Chapter I, most of the experimental observations were made near the end of the shock tube because of the higher temperatures that can be obtained behind the reflected shock. Therefore it is necessary to understand the theory of the first reflected shock wave and of subsequent reflections which occur at the end of the tube.

The problem of the reflection of a plane shock wave from a rigid wall was first treated by von Neumann.[23] In our analysis we will again make use of the p-vs-u graph as shown in Figure 4. The gas behind the primary shock wave has a velocity u_2 and must be brought to rest at the end of the tube. This can be accomplished only by a reflected shock moving toward the left since a rarefaction moving toward the left would accelerate the gas toward the right instead of bringing it to rest. The condition that the gas velocity be zero at the end of the tube can be expressed as

$$u_5 = u_2 - \phi_2(p_5) = 0,$$

The curve $u_2 - \phi_2(p)$ is shown in Figure 4 and its intersection with the p-axis gives the pressure p_5 for which the gas velocity is brought to zero behind the reflected shock wave.

Writing out the expression for $\phi_2(p_5)$ in the above condition gives

$$u_2 - \frac{(\mu-1)(y_{52}-1)c_2}{\sqrt{(\mu+1)(1+\mu y_{52})}} = 0 \tag{2.7}$$

where $y_{52} = p_5/p_2$. The flow velocity u_2 is given by

$$u_2 = \phi_1(p_2) = \frac{(\mu-1)(y_{21}-1)c_1}{\sqrt{(\mu+1)(1+\mu y_{21})}} .$$

Also, an expression must be found for the sound speed c_2. Using the fact that the sound speed is proportional to the square root of the temperature, we have

$$\frac{c_2}{c_1} = \sqrt{\frac{T_2}{T_1}} ,$$

and using equation (A.7) for the temperature ratio gives

$$\frac{c_2}{c_1} = \sqrt{y_{21}\frac{\mu+y_{21}}{1+\mu y_{21}}} .$$

Now by substituting these expressions for u_2 and c_2 into equation (2.7) above, we obtain the equation

$$\frac{(y_{21}-1)}{\sqrt{y_{21}(\mu+y_{21})}} = \frac{(y_{52}-1)}{\sqrt{1+\mu y_{52}}} \tag{2.8}$$

from which y_{52} can be determined as a function of the primary shock strength y_{21}. The above equation is quadratic in y_{52}, so there are two roots. One root is $y_{52} = 1/y_{21}$, but this would be a rarefaction wave which would not bring the gas flow to rest. The other root is

$$y_{52} = \frac{(\mu+2)y_{21}-1}{\mu+y_{21}}, \tag{2.9}$$

which is the physically correct solution.

Once y_{52} is known, the other hydrodynamic variables behind the reflected shock can be easily calculated. The density ratio $x_{52} = \rho_5/\rho_2$ is found, using the Rankine-Hugoniot equation (A.6),

$$x_{52} = \frac{1+\mu y_{52}}{\mu+y_{52}}.$$

The temperature T_5 is given by

$$\frac{T_5}{T_1} = \frac{T_5}{T_2}\cdot\frac{T_2}{T_1} = \frac{y_{21}(\mu+y_{21})}{(1+\mu y_{21})}\cdot\frac{y_{52}(\mu+y_{52})}{(1+\mu y_{52})},$$

using equation (A.7). Substituting for y_{52} from equation (2.9) and reducing, the temperature T_5 can be expressed as a function of y_{21} by the equation

$$\frac{T_5}{T_1} = \frac{[(2+\mu)y_{21}-1][\mu-1+2y_{21}]}{(1+\mu y_{21})(\mu+1)}. \tag{2.10}$$

The reflected shock velocity, which will be called U', can be found by the use of equation (A.12):

$$U' = u_2 - \sqrt{\frac{1+\mu y_{52}}{\mu+1}}\, c_2.$$

Substituting for u_2, c_2, and y_{52} and reducing the equation to its simplest form we have

$$U' = -\frac{(2y_{21}+\mu-1)c_1}{\sqrt{(\mu+1)(1+\mu y_{21})}}. \tag{2.11}$$

The reflected shock velocity is of course negative since the shock moves to the left. The solution of the variables behind the first reflected shock is now complete. As we have indicated by equation (A.12), the shock strength can be easily calculated from the measured primary shock velocity, and from this all the variables behind the primary shock can be found. Now we have shown that all the variables behind the reflected shock can also be calculated from the shock strength y_{21}. Therefore a measurement of the primary shock velocity plus a knowledge of the initial conditions ahead of the primary shock are all that is necessary for a complete solution of all the variables behind both the primary and first reflected shock waves.

The conditions at the end of the shock tube are complicated by the interaction of the reflected shock wave with the interface between the hot and cold gases (see Figure 1). In all cases a shock wave is transmitted through the interface into the cold flow, but the wave which is reflected back into the hot gas may be either a rarefaction or a shock wave, depending on the conditions. The interaction of the reflected shock with the interface can be best understood by the use of p-vs-u graphs as shown in Figure 6.

We start with the point (p_2, u_2) which defines both the hot flow and the cold flow back to the rarefaction foot. The temperatures and densities of the hot and cold flow are very different, but still the pressures and flow velocities are the same according to the ideal solution of the shock-tube problem given in Section 1. As in Figure 4, we draw the curve $u = u_2 - \phi_2(p)$ which represents all states behind a reflected shock moving toward the left into the hot flow, and the intersection with the p-axis gives the pressure p_5 when the gas is brought to rest. Next we con-

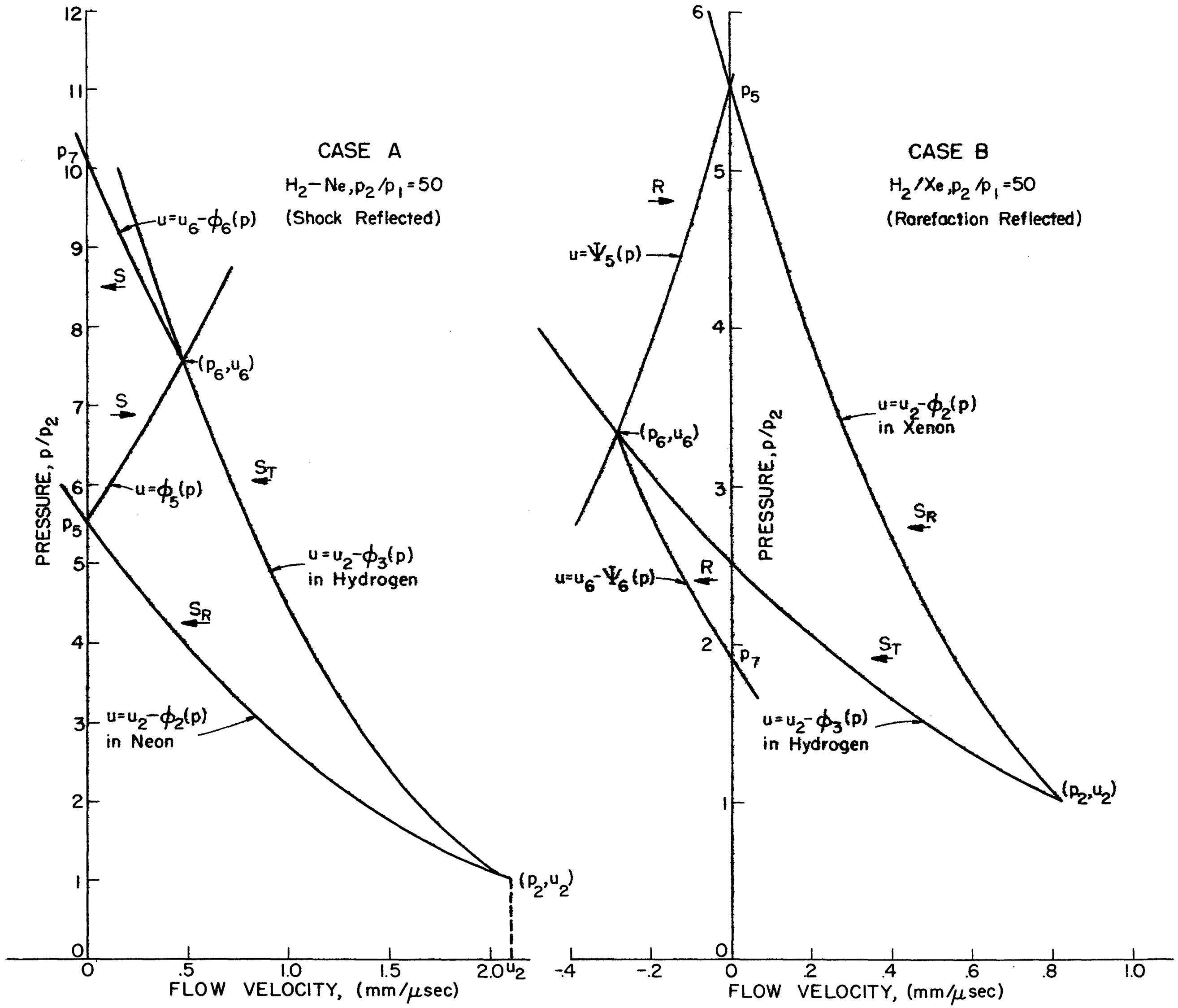

Figure 6. The pressure-velocity graphs for the interaction of the first reflected shock with the interface.

sider the shock wave which is transmitted through the interface into the cold flow. Again starting at the point (p_2, u_2), the curve $u = u_2 - \phi_3(p)$ is drawn. This curve is the locus of all states that can be reached by a shock wave moving to the left into the cold flow.

The curve $u = u_2 - \phi_2(p)$ is labeled with the symbol $\underset{\leftarrow}{S_R}$, which indicates the reflected shock wave moving toward the left into the incoming hot flow, and the curve $u = u_2 - \phi_3(p)$ is labeled with $\underset{\leftarrow}{S_T}$, which indicates the transmitted shock wave moving toward the left into the cold flow. The curve $\underset{\leftarrow}{S_T}$ may lie either above or below the curve $\underset{\leftarrow}{S_R}$, depending on the sound speeds in the hot and cold flows and the μ's of the two gases. If μ is the same for the two gases, then it is obvious from equation (2.11) that $\underset{\leftarrow}{S_T}$ will lie above the curve $\underset{\leftarrow}{S_R}$ if $c_3 < c_2$. We will divide the problem into two cases, Case A where $\underset{\leftarrow}{S_T}$ lies above $\underset{\leftarrow}{S_R}$ and Case B where $\underset{\leftarrow}{S_T}$ lies below $\underset{\leftarrow}{S_R}$.

The problem of the interaction of the reflected shock with the interfaces resolves itself into the following. What sort of wave must be propagated toward the right into the hot flow in order to fulfill the two boundary conditions across the interface, namely, that the interface can support no pressure difference and that the flow velocities are equal on both sides? Let us consider Case A first. A rarefaction wave moving toward the right cannot be a solution because the pressure p_6 would then be less than p_5. But $\underset{\leftarrow}{S_T}$ lies above $\underset{\leftarrow}{S_R}$, so only a shock wave $\underset{\rightarrow}{S}$ (i.e., a shock facing toward the right) can satisfy the boundary conditions on the interface. A pressure diagram of this interaction is shown in Figure 7a.

To find the values of p_6 and u_6 we start from the point $(p_5, 0)$ and draw the curve $u = \phi_5(p)$. Its intersection with the curve $\underset{\leftarrow}{S_T}$ then gives the pressure p_6 and the velocity u_6, both behind the transmitted shock

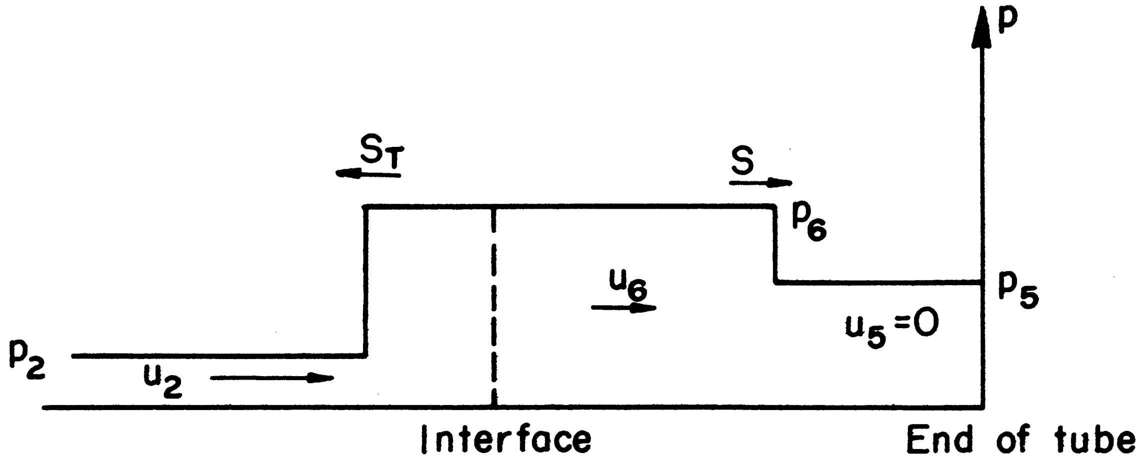

Figure 7a. Interaction of the reflected shock with the interface; Case A, shock reflected.

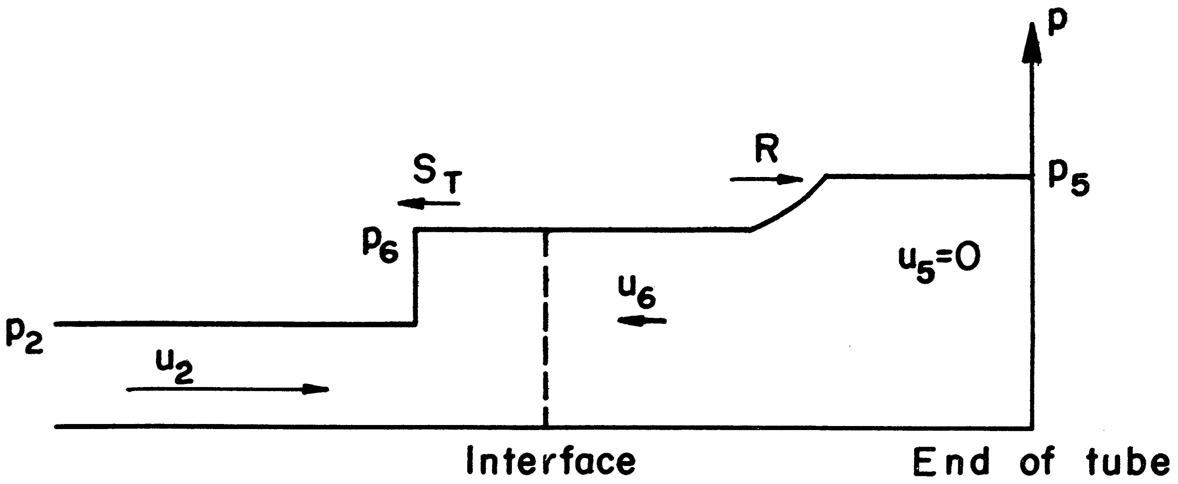

Figure 7b. Interaction of the reflected shock with the interface; Case B, rarefaction reflected.

moving into the cold flow and behind the reflected shock moving into the hot gas. The interface must of course move with the flow velocity u_6. Upon hitting the end of the tube the shock moving into the hot gas must be reflected in the same manner as the primary shock so that the flow velocity is brought to zero. To find the pressure behind the second reflection, from the end of the tube, the curve $u = u_6 - \phi_6(p)$ is drawn and its intersection with the p-axis gives the pressure p_7. This last shock wave will again interact with the interface producing another reflected shock, etc.

The other variables such as the density, temperature, and shock velocity can be calculated for each shock wave by using equations (A.6), (A.7), and (A.12). The variables in region (3), the cold flow, must be calculated to construct the function $\phi_3(p)$. This can be done by the assumption of isentropic expansion from p_4 to p_2, i.e.,

$$\frac{p_2}{\rho_2^{\gamma}} = \frac{p_4}{\rho_4^{\gamma}} .$$

Next let us consider Case B where the curve $\underleftarrow{S_T}$ lies below $\underleftarrow{S_R}$. The only type of wave moving to the right into the hot flow which can reduce the pressure p_5 to make possible an intersection with $\underleftarrow{S_T}$ is a rarefaction. The pressure profile for this type of reaction is shown in Figure 7b. A shock wave moving into the hot flow would result in an increased pressure, and therefore the curve $u = \phi_5(p)$ for a shock moving toward region (5) could not possibly intersect the curve $\underleftarrow{S_T}$. To solve the problem quantitatively we plot the curve $u = + \psi_5(p)$ for a rarefaction wave facing toward the right. Its intersection with the curve $\underleftarrow{S_T}$ then gives p_6 and u_6, which represents the flow induced by the transmitted shock in the cold gas and the flow induced by the rarefaction in the hot gas. The rarefaction wave will be reflected as another rarefaction from the end of the tube with the condition that $u_7 = 0$. Thus from the point (p_6, u_6) we draw the curve $u = u_6 - \psi_6(p)$ and its intersection with the p-axis gives the value of the pressure p_7.

The other variables behind the rarefaction waves are calculated from the isentropic formulae

$$\frac{p_b}{\rho_b^{\gamma}} = \frac{p_a}{\rho_a^{\gamma}}\,, \qquad p_a^{\frac{\gamma-1}{\gamma}} T_a = p_b^{\frac{\gamma-1}{\gamma}} T_b$$

and the sound speed from

$$\frac{c_b}{c_a} = \sqrt{\frac{T_b}{T_a}}\,.$$

The head or foot of a rarefaction always moves with the flow velocity plus or minus the sound speed of the adjacent constant state depending on whether the rarefaction wave is facing right or left.

The curves shown in Figure 6 were calculated using the ideal shock-tube theory for the cases H_2 - Ne, $y_{21} = 50$ and H_2 - Xe, $y_{21} = 50$. For the former a shock wave is reflected from the interface and for the latter the reflected wave is a rarefaction. The wavespeed diagrams for these two cases, together with the computed temperatures and pressures, are shown in Figure 8. For Case A the hot gas at the end of the tube is heated further by the shock reflected back from the interface so that in region (7) the temperature is considerably higher than in region (5), behind the first reflected shock. For Case B, on the other hand, although the temperature behind the first reflected shock is the same, the hot gas is cooled by each passage of the reflected rarefaction until in region (7) the temperature is 30% lower than in region (5).

At some critical primary shock strength a transition from a reflected

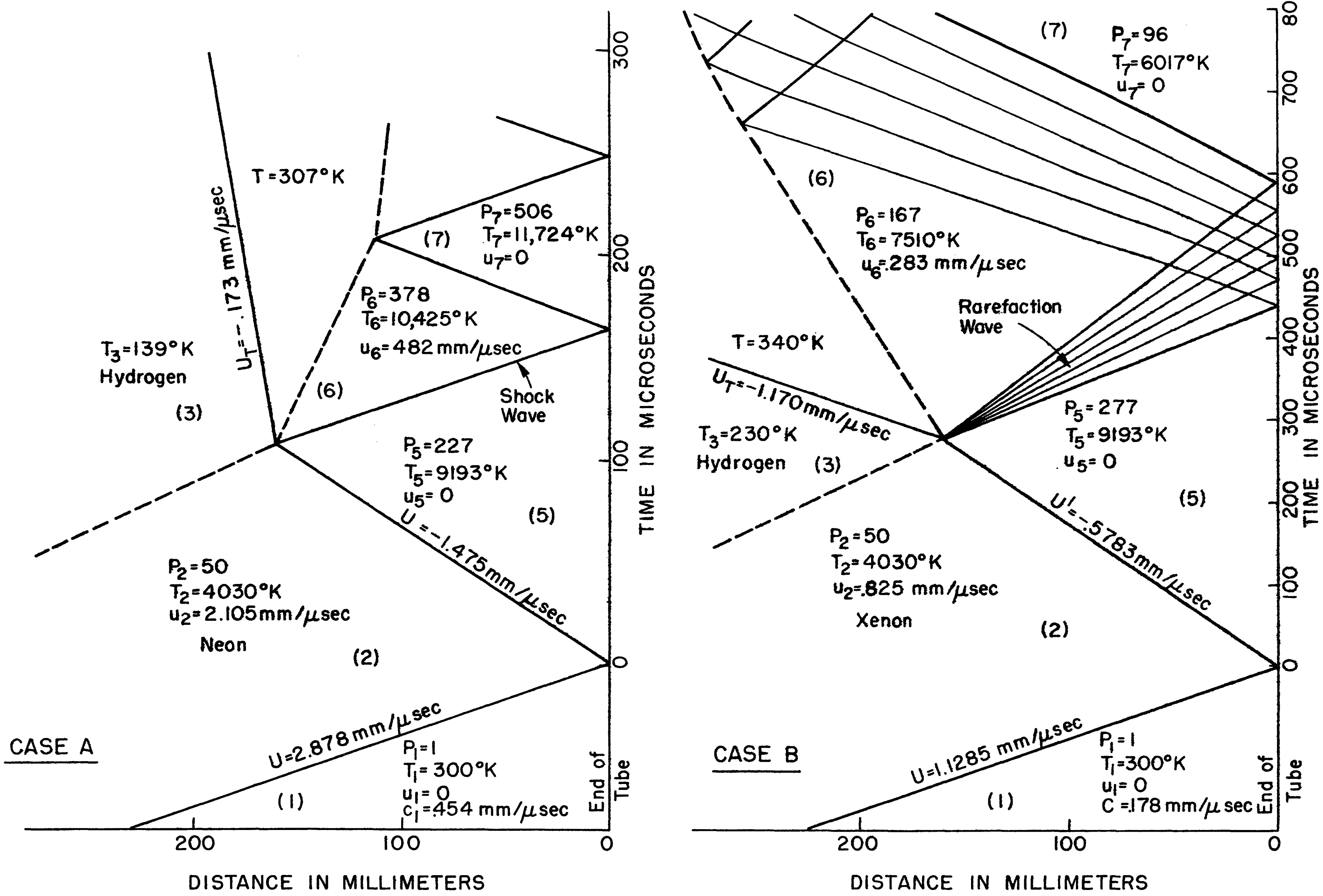

Figure 8. Distance-time diagrams of the interaction of the first reflected shock wave with the interface.

rarefaction to a reflected shock from the interface will occur. At this transition point the wave reflected from the interface will disappear and the first reflected shock will be transmitted into the cold flow with no change in strength. Also the velocity of the interface will be zero. The condition at this point is

$$\varphi_2(p_5) = \varphi_3(p_5),$$

i.e., that the curves $\underset{\leftarrow}{S_R}$ and $\underset{\leftarrow}{S_T}$ coincide at the p-axis. Written out in detail the above condition is

$$\frac{(\mu_1 - 1)(y_{52} - 1)c_2}{\sqrt{(\mu_1 + 1)(1 + \mu_1 y_{52})}} = \frac{(\mu_4 - 1)(y_{52} - 1)c_3}{\sqrt{(\mu_4 + 1)(1 + \mu_4 y_{52})}} . \tag{2.12}$$

For the case where $\mu_1 = \mu_4$ this reduces to the very simple condition that $c_2 = c_3$. When $c_2 < c_3$ a rarefaction is reflected from the interface, and when $c_2 > c_3$ a shock wave is reflected. It can be easily seen that if identical gases are used in both chambers of the shock tube, a shock wave must always be reflected from the interface since $c_2 > c_3$. The solution of y_{21} from equation (2.12) is most easily obtained graphically. The procedure is somewhat long and will therefore not be included in this thesis. The results for several combinations of gases are given in Table III below.

Table III. Critical Primary Shock Strengths

Combination of Gases	Critical Primary Shock Strength*
H_2 - Ne	24
H_2 - A	50
H_2 - Kr	102
H_2 - Xe	163
He - A	17
He - Xe	60

---

*Shock strength at which there is no reflection from the interface.

Figure 8 illustrates that even though the primary shock strengths may be the same (i.e., 50) there are different types of reflections at the interface for neon and xenon.

3. The Effect of Ionization

As the temperature of the rare gases increases, ionization becomes increasingly important and must be taken into account in the hydrodynamic equations. A degree of ionization of only 1% has a profound effect on the flow, and the ideal theory is no longer adequate. In theoretical calculations of the hydrodynamic variables in argon, Shao-Chi Lin[24,14] found that for an initial pressure of 1 cm Hg deviations from the ideal theory due to ionization became important at a temperature of about 8000°K.* For the other rare gases this critical temperature varies directly with the ionization potential. In xenon, for example, ionization would become important at about 6200°K. We will consider only the rare gases because of the greater simplicity of the problem. The specific heats for the rare gases are almost constant up to the temperature where ionization occurs. For diatomic molecules, however, one must consider the effects of vibration, excitation, and dissociation which change the specific heat at relatively low temperatures.

For the shock-wave theory of ideal gases given in Appendix A we had the three conservation equations

---

*At first glance it may seem strange that appreciable ionization could take place in argon at a temperature of less than 1 electron volt (1 volt is equivalent to 11,606°K) when the ionization potential is 15.68 volts. The answer lies in the fact that, according to the Boltzmann distribution of velocities, there are some particles with enough velocity to cause ionization. Also, according to the mass-action law, the equilibrium is driven in the direction of producing more particles by the relatively low gas pressure.

$$\rho_a v_a = \rho_b v_b \tag{A.1}$$

$$\rho_a v_a^2 - \rho_b v_b^2 = p_b - p_a \tag{A.2}$$

$$\frac{1}{2} v_a^2 + h_a = \frac{1}{2} v_b^2 + h_b \tag{A.3}$$

plus the equation of state and four unknowns, p_b, ρ_b, T_b, and v_b. Therefore the unknowns could be completely determined. For partially ionized gases the three conservation conditions above still hold under the original assumptions that heat is not added to or removed from the gas and that viscosity and heat conduction are negligible. There is another variable, however, which is the fraction of the gas ionized, so yet another equation is required for a complete solution.

The relation between the degree of ionization and the temperature and pressure was first derived by N. M. Saha from thermodynamical considerations. Later Menzel[25] gave a derivation of this equation, using statistical mechanics. The Saha equation is

$$\frac{N_1}{N_0} p_e = \frac{(2\pi m)^{3/2}(kT)^{5/2}}{h^3} \frac{2B_1(T)}{B_0(T)} e^{-\frac{\chi}{kT}} \tag{2.13}$$

The variables are defined as follows:

N_1 = number of ionized atoms per cc

N_0 = number of neutral atoms per cc

p_e = electron pressure

χ = ionization potential of the atom

m = reduced mass of ion and electron (essentially equal to the mass of the electron)

h = Planck's constant

k = Boltzmann's constant

$B_1(T)$ = partition function for the ionized atom

$B_0(T)$ = partition function for the neutral atom.

Let us designate the fraction of the gas which is ionized by α and let p be the total pressure of atoms + ions + electrons. The fraction of ionized atoms is $\alpha/(1 + \alpha)$, the fraction of neutral atoms is $(1 - \alpha)/(1 + \alpha)$, and the electron pressure is $\alpha p/(1 + \alpha)$. The Saha equation can then be written

$$\frac{\alpha^2}{(1-\alpha^2)} p = \frac{(2\pi m)^{3/2}(kT)^{5/2}}{h^3} \frac{2B_1(T)}{B_0(T)} e^{-\frac{\chi}{kT}},$$

which can be solved for α to give

$$\alpha = \left[p \frac{h^3}{(2\pi m)^{3/2}(kT)^{5/2}} \frac{B_0(T)}{2B_1(T)} e^{\frac{\chi}{kT}} + 1\right]^{-\frac{1}{2}}. \tag{2.14}$$

The partition function is defined as

$$B(T) = \sum_n g_n e^{-\frac{E_n}{kT}}$$

where g_n is the statistical weight of a level of energy E_n. The energy of the ground state is arbitrarily set equal to zero. Bond[26] has calculated the partition functions for neutral and singly ionized argon up to 26,000°K. He has found that at temperatures of up to 15,000°K there is an error of less than 1% in assuming that $B_0(T) = 1$ for neutral argon, the contribution of only the ground state. As the temperature increases, however, the higher excited states contribute more to the partition function. The energy-level diagrams of all the rare gases are quite similar so that one can safely assume that the limit above which $B_0(T) = 1$ is no longer accurate varies approximately as the ionization potential. With xenon, for example, the contributions of the upper levels of excitation would become important at temperatures of greater than 11,500°K. In this work it will be assumed that the temperature of the gas is low enough so that $B_0(T) \cong 1$.

For the rare-gas ions the lowest lying levels are $^2P_{3/2,\,1/2}$ with a small energy difference E_1 between the levels with different J values. A schematic energy-level diagram is shown in Figure 9. The $^2P_{3/2}$ level is the lower of the two, so the contribution of these levels to the partition function is

$$B_1(T) = 4 + 2e^{-\frac{E_1}{kT}}.$$

Bond's calculations show that for argon the higher excited states of the ion do not contribute appreciably at temperatures as high as 20,000°K. If the numerical values for h, k, and m are put into equation (2.14), we get

$$\alpha = \left[\frac{p}{T^{5/2}}\,\frac{10^4}{2+e^{-E_1/kT}}\,e^{\frac{\chi}{kT}}+1\right]^{-1/2} \tag{2.15}$$

where p is expressed in cm of mercury pressure and T in degrees Kelvin. The values for the ionization potential and the energy difference between the two lowest states of the ionized atoms are shown in Table IV. The values are given in equivalent temperature in degrees Kelvin.

Table IV. Ionization Energies of the Rare Gases

Gas	$\Theta = \chi/k$	E_1/k
Neon	249,000°	1120°
Argon	182,000°	2060°
Krypton	162,000°	7720°
Xenon	140,000°	15200°

The equation of state must be altered since additional particles are being produced by ionization. It will be assumed that the atoms, ions, and electrons behave separately as ideal gases and that the interactions between them can be neglected insofar as the equation of state is concerned.

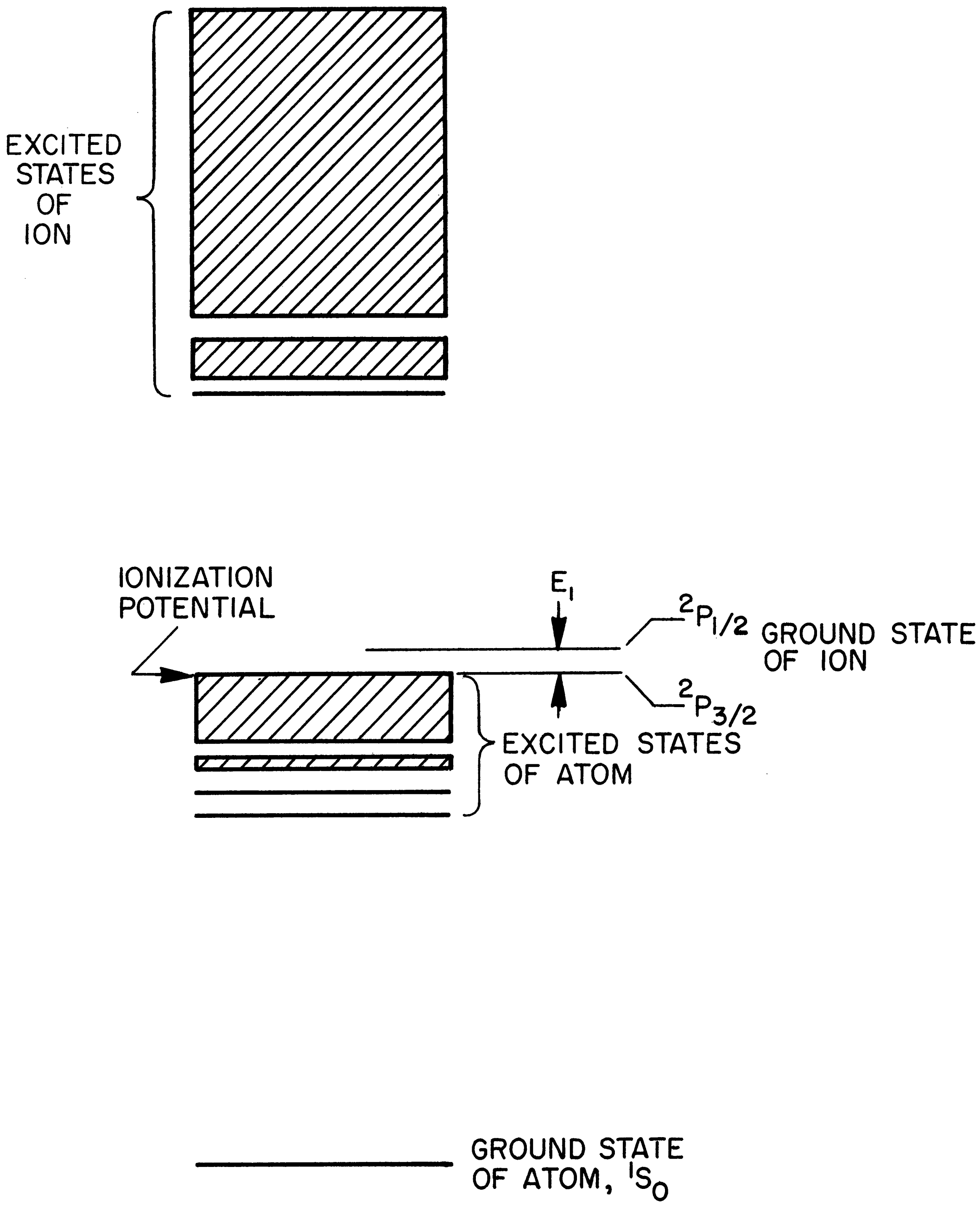

Figure 9. Simplified diagram of energy levels of a rare-gas atom and ion.

Astrophysical calculations have shown the validity of this assumption in the range of temperatures and pressures with which we are concerned.* The pressure of the atoms plus ions is

$$p_A + p_I = NkT$$

and the pressure of the electrons is

$$p_e = \alpha NkT$$

where N = number of atoms plus ions per cc. The density is

$$\rho = N m_A \,, \qquad (m_A = \text{mass of atom})$$

since the electrons contribute very little mass. The equation of state is therefore

$$\frac{p}{\rho} = (1+\alpha)\frac{kT}{m_A} = (1+\alpha)\frac{R_0 T}{M_A} \,.$$

R_0 is the universal gas constant and M_A is the molecular weight. The equation of state will usually be used in the form

$$\frac{p}{\rho} = (1+\alpha)RT \,, \quad R = \frac{R_0}{M_A} \,. \tag{2.16}$$

Finally, an expression for the enthalpy must be derived, or since $h = e + p/\rho$ we can find instead an expression for the specific energy e. The energy of a rare gas at high temperatures is made up of three parts:

e_t = translational energy of atoms, ions, and electrons;

e_e = energy of excitation of the atoms and ions;

e_i = energy of ionization.

$$e = e_t + e_e + e_i$$

The translational energy per cc is

$$\frac{3}{2}(1+\alpha)NkT$$

---

*See Chapter III of Ref. 27.

where N is the number of atoms plus ions per cc. The specific energy e_t is therefore

$$e_t = \frac{3}{2}(1+\alpha)RT.$$

The probability that an atom or ion will have the electronic energy E_n is

$$\frac{g_n e^{-E_n/kT}}{B(T)}$$

so the average excitation energy for an atom or ion is

$$\frac{\sum_n E_n g_n e^{-E_n/kT}}{B(T)}.$$

The specific energy due to excitation of the atoms and ions is therefore

$$e_e = (1+\alpha)RT\frac{\left(\sum_n \frac{E_n}{kT} g_n e^{-E_n/kT}\right)_{ATOMS}}{B_0(T)} + \alpha RT\frac{\left(\sum_n \frac{E_n}{kT} g_n e^{-\frac{E_n}{kT}}\right)_{IONS}}{B_1(T)}.$$

Shao-Chi Lin[24] has calculated, however, that at a temperature of 16,000°K the energy of excitation is only 1.7% of the total enthalpy of argon. At higher temperatures the energy of excitation becomes appreciable. To simplify the theory we will neglect the excitation energy, but the resulting formulae will be valid only for temperatures of less than 16,000°K for argon.[*] The maximum useable temperatures for the other rare gases will be

---

[*] The population of the $^2P_{1/2}$ state of the ion will be appreciable even at low temperatures. The specific excitation energy for ions is then $[2R/B_1(T)]\ [E_1/kT]\ [e^{-E_1/kT}]$ at temperatures below which the upper states contribute. This is to be compared with the ionization energy of $R\Theta$. For neon and argon $\Theta \gg E_1/kT$ (see Table IV), so the excitation energy of this level can be neglected. For krypton and xenon the energy of this level is larger, but even for xenon at 10,000°K, it is only 1-1/2% of the ionization energy. At a degree of ionization of 5%, the error introduced by neglecting the energy of the $^2P_{1/2}$ level is only about 1/2% of the total enthalpy for xenon.

approximately in proportion to their ionization potentials.

The ionization energy per cc is

$$\alpha N \chi$$

so the specific energy due to ionization is

$$e_i = \alpha R \frac{\chi}{k} = \alpha R \theta$$

where $\theta = \chi/k$. The total specific energy is now

$$e \cong \frac{3}{2}(1+\alpha)RT + \alpha R\theta \tag{2.17}$$

and the enthalpy is therefore

$$h = \frac{5}{2}(1+\alpha)RT + \alpha R\theta. \tag{2.18}$$

We now have sufficient preparation to derive some equations for the hydrodynamic variables behind a shock wave when ionization occurs. Because of the form of the Saha equation many of the equations will be transcendental, requiring numerical methods of solution. A number of useful equations may be derived, however, by assuming the degree of ionization behind the shock wave to be known.

The three conservation equations (A.1), (A.2), and (A.3) are still valid for ionization, so the Hugoniot relation (A.4) which was derived derectly from them is also valid. Putting in the expression for the enthalpy derived above, we obtain a new Rankine-Hugoniot equation which is similar to equation (A.6),

$$\frac{\rho_b}{\rho_a} = \frac{\mu \frac{p_b}{p_a} + 1}{\frac{p_b}{p_a} + \mu - 2\frac{(\alpha_b - \alpha_a)}{(1+\alpha_a)}\frac{\theta}{T_a}} \tag{2.19}$$

Döring[28] obtained a similar sort of Rankine-Hugoniot equation for very strong shock waves in nitrogen. For a shock wave moving into a gas which is not ionized, such as the primary shock wave in the shock tube,

$$\frac{\rho_b}{\rho_a} = \frac{\mu \frac{p_b}{p_a} + 1}{\frac{p_b}{p_a} + \mu - 2\alpha_b \frac{\theta}{T_a}} . \tag{2.20}$$

Here one observes the first important effect of ionization on the hydrodynamics of a shock wave. In the ideal case of no ionization the density ratio approaches the limit μ asymptotically for large shock strengths. In the above equation, however, the ratio θ/T_a may be almost 200 for the rare gases. Therefore, if the degree of ionization were say 5%, the negative term would subtract about 20 from the denominator. Thus the density ratio might rise considerably above the ideal limit μ. The increased density ratio leads to a decrease in the temperature, as one can see in using the equation of state (2.16).

$$\frac{T_b}{T_a} = \frac{(1+\alpha_a)}{(1+\alpha_b)} \frac{p_b}{p_a} \frac{\rho_a}{\rho_b} . \tag{2.21}$$

The flow velocity and shock velocity are also changed by ionization but not as much as the density and temperature ratios. In order to derive an expression for the flow velocity, we use equation (A.9), which is still valid for the case of ionization.

$$\frac{\left(\frac{p_b}{p_a} - 1\right)}{\left(1 - \frac{\rho_a}{\rho_b}\right)} p_a \rho_a = \left(\frac{p_b - p_a}{u_b - u_a}\right)^2 = \frac{\left(\frac{p_b}{p_a} - 1\right)^2}{(u_b - u_a)^2} p_a^2 .$$

Solving for $(u_b - u_a)^2$ gives

$$(u_b - u_a)^2 = \frac{p_a}{\rho_a} \frac{\left(\frac{\rho_b}{\rho_a} - 1\right)}{\frac{\rho_b}{\rho_a}} \left(\frac{p_b}{p_a} - 1\right) . \tag{2.22}$$

Substituting for ρ_b/ρ_a from the Rankine-Hugoniot equation (2.19), we have

$$(2.23)\qquad (u_b-u_a)^2=(1+\alpha_a)RT_a\left[\frac{(\mu-1)\left(\frac{p_b}{p_a}-1\right)+2\left(\frac{\alpha_b-\alpha_a}{1+\alpha_a}\right)\frac{\theta}{T_a}}{\mu\frac{p_b}{p_a}+1}\right]\left(\frac{p_b}{p_a}-1\right),$$

or for a shock wave moving into a gas which is not ionized this simplifies to

$$(2.24)\qquad (u_b-u_a)^2=RT_a\left[\frac{(\mu-1)\left(\frac{p_b}{p_a}-1\right)+2\alpha_b\frac{\theta}{T_a}}{\mu\frac{p_b}{p_a}+1}\right]\left(\frac{p_b}{p_a}-1\right).$$

It can be seen from the above equation that the effect of ionization is to cause an increase in the flow velocity behind a very strong shock wave.

To obtain the shock velocity, U, one uses the conservation-of-mass equation (A.1)

$$\frac{\rho_b}{\rho_a}=\frac{v_a}{v_b}=\frac{u_a-U}{u_b-U}=\frac{(U-u_a)}{(u_b-u_a)-(U-u_a)}.$$

Solving for $(U - u_a)$ and squaring gives

$$(U-u_a)^2=\left(\frac{\frac{\rho_b}{\rho_a}}{\frac{\rho_b}{\rho_a}-1}\right)^2(u_b-u_a)^2,$$

and substituting for $(u_b - u_a)^2$ from equation (2.22) gives

$$(2.25)\qquad (U-u_a)^2=\frac{p_a}{\rho_a}\,\frac{\frac{\rho_b}{\rho_a}}{\left(\frac{\rho_b}{\rho_a}-1\right)}\left(\frac{p_b}{p_a}-1\right).$$

Putting in the expression for ρ_b/ρ_a from equation (2.19), we have

$$(2.26)\qquad (U-u_a)^2=(1+\alpha_a)RT_a\left[\frac{\mu\frac{p_b}{p_a}+1}{(\mu-1)\left(\frac{p_b}{p_a}-1\right)+2\left(\frac{\alpha_b-\alpha_a}{1+\alpha_a}\right)\frac{\theta}{T_a}}\right]\left(\frac{p_b}{p_a}-1\right).$$

Again, for a shock wave moving into a gas that is not ionized,

$$(2.27)\qquad (U-u_a)^2 = RT_a\left[\frac{\mu\frac{p_b}{p_a}+1}{(\mu-1)\left(\frac{p_b}{p_a}-1\right)+2\alpha_b\frac{\theta}{T_a}}\right]\left(\frac{p_b}{p_a}-1\right).$$

For a given shock strength the effect of ionization is to decrease the shock velocity. The net result of ionization therefore is to decrease the difference between the shock and flow velocities, which is also self-evident from the conservation-of-mass equation.

It is theoretically possible to obtain equation (2.27) in the form $(U - u_a) = F\,(p_b/p_a,\ p_a,\ T_a)$, which would then be inverted to find the shock strength p_b/p_a as a function of the measured shock velocity U. To do this, one would have to eliminate ρ_b and T_b from the Saha equation, the equation of state, and the Rankine-Hugoniot equation to get α as a function of p_b/p_a and the initial state variables and then substitute for α in equation (2.27). Besides being transcendental, the resulting equation would be very complicated and could be solved only by laborious numerical methods. A more practical method of solution is to use a fast-converging iteration procedure such as the one described below.

Consider the primary shock wave in the tube. For this case, equation (2.27) can be written

$$(2.28)\qquad \left(\frac{U}{c_1}\right)^2 = \left[\frac{4y_{21}+1}{3(y_{21}-1)+2\alpha_2\frac{\theta}{T_1}}\right]\frac{3}{5}\,(y_{21}-1)$$

where $\mu = 4$ for a monatomic gas and $c_1 = \sqrt{5/3\ RT_1}$. Equation (2.28) is quadratic in y_{21} and can be solved immediately.

$$(2.29)\qquad y_{21} = \frac{1}{8}\left\{3+5\left(\frac{U}{c_1}\right)^2+5\sqrt{\left[\left(\frac{U}{c_1}\right)^2-1\right]^2+\frac{32}{15}\alpha_2\frac{\theta}{T_1}\left(\frac{U}{c_1}\right)^2}\right\}.$$

In addition to this equation we also use the relation for the temperature,

$$T_2 = \frac{T_1}{(1+\alpha_2)} \frac{y_{21}}{x_{21}} ,$$

the Rankine-Hugoniot equation,

$$x_{21} = \frac{4y_{21}+1}{y_{21}+4-2\alpha_2 \frac{\theta}{T_1}} ,$$

and the Saha equation,

$$\alpha_2 = \left[1 + \frac{10^4 y_{21} p_1}{T_2^{5/2}} \frac{e^{\theta/T_2}}{(2+e^{-E_1/kT_2})}\right]^{-1/2} .$$

The iteration procedure now goes as follows: Assuming a value for α_2, calculate the shock strength y_{21} from the measured shock velocity U. Calculate x_{21} from the Rankine-Hugoniot equation and then T_2. From y_{21} and T_2 use the Saha equation to calculate a new α_2. Recalculate y_{21}, x_{21}, and T_2, using this second α_2, and from the second y_{21} and T_2 obtain a third α_2, etc. The number of iterations depends on the accuracy desired. This method converges fairly fast.

It is of course, far more convenient if curves of the hydrodynamic variables in the shock tube are prepared in advance. Shao-Chi Lin[24] in his thesis gives curves of temperature, pressure, density, degree of ionization, and flow velocity behind the primary shock wave in argon for initial pressures of 1, 5, and 15 cm Hg plotted vs the shock Mach number. He also included curves of temperature, density, degree of ionization, and shock velocity for the region behind the reflected shock wave.

The variables behind the reflected shock wave can be found by plotting a p - u curve for the gas behind the shock, as discussed in Section 2* (see also Figure 4). The relation between the pressure and flow ve-

---

*The variables behind the primary shock must all be known.

locity is given in this case by equation (2.22) or (2.23). Because α_5 depends on T_5 and p_5, an equation for the curve cannot be expressed in closed form, so several points on the curve must be calculated numerically, one at a time. The boundary condition for the first reflected shock is that the flow velocity be brought to zero. Therefore the pressure, p_5, behind the reflected shock is the point of intersection of the p - u curve with the p-axis. Usually only a few points on the curve close to the p-axis are necessary for an accurate determination of p_5.

The equations that are necessary to calculate points on the p - u curve are the Rankine-Hugoniot equation,

$$X_{52} = \frac{4y_{52}+1}{y_{52}+4-2\left(\frac{\alpha_5-\alpha_2}{1+\alpha_2}\right)\frac{\theta}{T_2}} ;$$

the relation for the temperature,

$$\frac{T_5}{T_2} = \left(\frac{1+\alpha_2}{1+\alpha_5}\right)\frac{y_{52}}{X_{52}} ;$$

the Saha equation,

$$\alpha = \left[1 + \frac{10^4 p_2 y_{52}}{T_5^{5/2}} \frac{e^{\frac{\theta}{T_5}}}{\left(2+e^{-E_1/kT_5}\right)}\right]^{-\frac{1}{2}} ;$$

and the equation for the flow velocity, equation (2.48),

$$(u_5-u_2)^2 = (1+\alpha_2)RT_2 \frac{X_{52}-1}{X_{52}} (y_{52}-1) .$$

The procedure is as follows: One assumes a value of y'_{52} that is probably close to the true value (usually $y_{52} \cong 5.8$). Then a value of α'_5 is also assumed and one calculates x'_{52} and T'_{52}. From the Saha equation a new value of α''_5 may then be found. If this new value of α''_5 is close (within ± 10%) to the originally assumed value, the next step may be taken. If not, a better estimate of α'_5 can be made, x'_{52} and

T'_{52} can be recalculated, and a new α''_5 found from the Saha equation. The accuracy of the next step depends on the fact that α varies slowly with p. Substituting x_{52} from the Rankine-Hugoniot equation into the temperature relation, we obtain a quadratic equation in y_{52}.

$$(2.30) \quad y_{52}^2 - \left[4\frac{T_5}{T_2}\left(\frac{1+\alpha_5}{1+\alpha_2}\right) + 2\left(\frac{\alpha_5-\alpha_2}{1+\alpha_2}\right)\frac{\theta}{T_2} - 4\right] y_{52} - \frac{T_5}{T_2}\left(\frac{1+\alpha_5}{1+\alpha_2}\right) = 0 .$$

Using T'_5 and α''_5 in the above, y''_{52} can be determined and it should be extremely close to the true value. Now using the above equation for the flow velocity, we can calculate u_5. The x''_{52} used in this equation should be calculated from α''_5 and the new y''_{52}. This now gives a point (p_5, u_5) on the curve. Several points on either side of the p-axis will allow one to interpolate to find accurate values of p_5, α_5, and T_5. The reflected shock velocity can be found, using equation (2.25).

If one wishes to calculate the hydrodynamic variables behind successive shock waves resulting from the interaction with the interface, the principles of Section 2 can be followed, using the above-outlined method for calculating points on the p - u curves for the shock waves.

4. Mixtures of Gases

It has sometimes been found very convenient to add to the carrier gas a small amount of a test gas which is to be studied. For example, in the study of hydrogen line broadening we have added about 1% hydrogen to neon. This technique will be discussed further in Chapter V, but here we will develop the necessary mathematical formulae.

The test gas in most cases is diatomic. It is assumed that the test gas is completely dissociated behind the primary shock wave but that no ionization takes place. Then for the first reflected shock and subsequent shock waves the gas may be considered as a mixture of monatomic gases. This latter case will be considered first and later we will return to the problem of the primary shock wave.

Let N^i be the number of atoms plus ions per cc of the i^{th} gas and let α^i be the fraction ionized. Then the total pressure is

$$p = \sum_i N^i(1+\alpha^i)kT.$$

The density of the gas is $\rho = \sum_i N^i m^i$ where m^i is the mass of one atom of the i^{th} gas. If ϵ^i is the fraction of the i^{th} gas before ionization, the equation of state then becomes

$$\frac{p}{\rho} = \frac{\sum_i \varepsilon^i(1+\alpha^i)kT}{\sum_i \varepsilon^i m^i}.$$

The gas constant per gram is

$$R = \frac{R_0}{\sum_i \varepsilon^i M^i}$$

where R_0 is the universal gas constant and M^i is the molecular weight of the i^{th} gas. So the equation of state is written

$$\frac{p}{\rho} = \sum_i \varepsilon^i(1+\alpha^i)RT. \tag{2.31}$$

The specific internal energy of the gas, neglecting excitation, is

$$e = \frac{3}{2}\sum_i \varepsilon^i(1+\alpha^i)RT + R\sum_i \alpha^i\varepsilon^i\theta^i.$$

The first term is the translation energy and the second term is the energy of ionization. Θ^i is the ionization energy χ^i divided by Boltzmann's constant. The enthalpy is therefore

$$h = \frac{5}{2}\frac{p}{\rho} + R\sum_i \alpha^i\varepsilon^i\theta^i. \tag{2.32}$$

Putting this expression for h into the Hugoniot equation (A.4), we arrive at the modified Rankine-Hugoniot equation

$$(2.33) \qquad \frac{\rho_b}{\rho_a} = \frac{4\frac{p_b}{p_a}+1}{\frac{p_b}{p_a}+4-2\frac{\sum \varepsilon^i\theta^i(\alpha_b^i-\alpha_a^i)}{\sum \varepsilon^i(1+\alpha_a^i)T_a}} .$$

The flow velocity is similar to equation (2.22).

$$(2.34) \qquad (u_b-u_a)^2 = \sum_i \varepsilon^i(1+\alpha_a^i)RT_a\left(\frac{\frac{\rho_b}{\rho_a}-1}{\frac{\rho_b}{\rho_a}}\right)\left(\frac{p_b}{p_a}-1\right)$$

$$= \sum_i \varepsilon^i(1+\alpha_a^i)RT_a\left[\frac{3\left(\frac{p_b}{p_a}-1\right)+2\frac{\sum \varepsilon^i\theta^i(\alpha_b^i-\alpha_a^i)}{\sum \varepsilon^i(1+\alpha_a^i)T_a}}{4\frac{p_b}{p_a}+1}\right]\left(\frac{p_b}{p_a}-1\right)$$

and the shock velocity is given by equation (2.25), using equation (2.31) for p/ρ or by

$$(2.35) \qquad (U-u_a)^2 =$$

$$\sum_i \varepsilon^i(1+\alpha_a^i)RT_a\left[\frac{4\frac{p_b}{p_a}+1}{3\left(\frac{p_b}{p_a}-1\right)+2\frac{\sum \varepsilon^i\theta^i(\alpha_b^i-\alpha_a^i)}{\sum \varepsilon^i(1+\alpha_a^i)T_a}}\right]\left(\frac{p_b}{p_a}-1\right) .$$

The temperature ratio is

$$(2.36) \qquad \frac{T_b}{T_a} = \frac{\sum \varepsilon^i(1+\alpha_a^i)}{\sum \varepsilon^i(1+\alpha_b^i)}\,\frac{p_b}{p_a}\,\frac{\rho_a}{\rho_b} .$$

The hydrodynamic variables behind the reflected shock may be solved by the same method described in Section 3, except that one must now solve several simultaneous Saha equations of the form [see equation (2.13)].

$$\log\left[\frac{\alpha^i}{(1-\alpha^i)}\sum_j \alpha^j p_0^j\right] = -\frac{\chi^i}{kT}\log e + \frac{5}{2}\log T + \log\frac{(2\pi m)^{3/2}k^{5/2}}{h^3}\,\frac{2B_1^i(T)}{B_0^i(T)}, \tag{2.37}$$

The expression p_o^j is pressure of atoms + ions of the j^{th} gas, so $\sum \alpha^j p_o^j$ is the total electron pressure. Logarithms are to the base 10. Putting in the values of the physical constants, the above equation may be written as

$$\log\left[\frac{\alpha^i}{(1-\alpha^i)}p_e\right] = -\chi^i\,\frac{5040.4}{T} + \frac{5}{2}\log T - 0.477 + \log\frac{2B_1^i(T)}{B_0^i(T)} \tag{2.38}$$

where χ^i is now given in electron volts.

For the primary shock wave we assume that all molecules are completely dissociated but that no ionization takes place. Let δ^1 be the fraction of the monatomic carrier gas and $\delta^2, \delta^3, \ldots$.* be the fractions of the diatomic test gases which are much less than δ^1. It is assumed that $\gamma = 7/5$ for the diatomic test gases and, of course, $\gamma = 5/3$ for the monatomic carrier gas. The equation of state and the enthalpy in region (1) ahead of the primary shock are

$$\frac{p_1}{\rho_1} = RT_1 \qquad \text{where} \qquad R = \frac{R_0}{\sum_i \delta^i M^i} \qquad \text{and}$$

$$h_1 = \frac{5}{2}\delta^1 RT_1 + \frac{7}{2}\sum_{i=2}\delta^i RT_1 = \frac{5}{2}\frac{p_1}{\rho_1}\left(1 + \frac{2}{5}\sum_{i=2}\delta^i\right) ; \tag{2.39}$$

---

*These δ's are not the same as the ε's used earlier, but they are, of course, related.

$$\varepsilon^i = 2\,\frac{\delta^i}{\delta^1 + 2\sum_{i=2}\delta^i} .$$

while in region (2) behind the shock the equation of state is

$$\frac{p_2}{\rho_2} = \left(\delta^1 + 2\sum_{i=2}\delta^i\right)RT_2 \tag{2.40}$$

and the enthalpy is

$$h_2 = \frac{5}{2}\frac{p_2}{\rho_2} + R\sum_{i=2}\delta^i\Phi^i \ . \tag{2.41}$$

$\Phi^i = E_D/k$ where E_D is the energy of dissociation.

Putting these expressions for the enthalpy into the Hugoniot equation gives

$$x_{21} = \frac{4y_{21}+1}{y_{21}+4-2\sum_{i=2}\delta^i\left(\frac{\Phi^i}{T_1}-1\right)} \ . \tag{2.42}$$

The flow velocity u_2 may be found by putting this value of x_{21} into equation (2.22) and an expression for the shock velocity can be written down by substituting for x_{21} in equation (2.25). This gives

$$U = R_1T_1\left[\frac{4y_{21}+1}{3(y_{21}-1)+2\sum_{i=2}\delta^i\left(\frac{\Phi^i}{T_1}-1\right)}\right](y_{21}-1) \ . \tag{2.43}$$

Then in the same manner as equation (2.29) was obtained we can write

$$y_{21} = \frac{1}{8}\left\{3+5\frac{U^2}{\frac{5}{3}R_1T_1}+5\sqrt{\left(\frac{U^2}{\frac{5}{3}R_1T_1}-1\right)^2+\frac{32}{15}\frac{U^2}{\frac{5}{3}R_1T_1}\sum_{i=2}\delta^i\left(\frac{\Phi^i}{T_1}-1\right)}\right\} \ . \tag{2.44}$$

From this equation one can solve for the shock strength from the measured shock velocity. From this primary shock strength one can solve for all the remaining variables behind the primary shock and also behind the reflected shock by using the equations developed previously.

CHAPTER III

DESCRIPTION OF APPARATUS

1. The Shock Tube

The first experiments on luminosity behind shock waves done in this laboratory[12,13] were carried out using the 2 x 7-inch cross-section shock tube. Almost all the experimental work reported in this dissertation, however, was done with a smaller tube designed expressly for the production of very strong shock waves.

This shock tube has an overall length of about 12 feet and a rectangular internal cross section of 1-5/8 x 2-5/8 inches. The tube was made from commercial cold-drawn steel tubing of 3/16-inch wall thickness, the corners of which were round with a 1/8- to 3/16-inch radius. The inside surface is about as smooth as cold-rolled steel, and no additional finishing was done to improve it. One section of the tube was tested at 700 psia* pressure and showed no leaks or distortion. The high-pressure chamber was built to withstand a pressure of 2000 psia by putting the rectangular tubing inside a standard 5-inch round steel pipe and pouring concrete in between.

The sections of the shock tube were fabricated by welding round steel flanges to the ends of the rectangular tubing and machining the flanges for "O" rings. The sections are fastened together with eight 3/8-inch bolts. The high-pressure chamber is 47 inches long and is made in one

---

*Psia is an abbreviation for pounds per square inch absolute, and psi is an abbreviation for pounds per square inch above atmospheric pressure.

section. The low-pressure chamber consists of four sections, exclusive of the test section, two of 31-1/2-inch length and two of 15-1/2-inch length, making a length of 94 inches. The relative lengths of the high- and low-pressure chambers were determined so that the rarefaction wave reflected from the end of the high-pressure chamber would not reach the luminous region before the reflected shock met the interface. These calculations followed the method described by Mautz.[8]

The reason that the tube was constructed with a rectangular cross section rather than circular was that it was desired to make optical observations in the region behind the reflected shock. A round glass tube would not have been strong enough to withstand the high pressure in this region. A rectangular section permits the use of thick, plane side windows which make possible the observation of the flow from the top to the bottom of the tube and also to the very end. The size of the tube was determined mainly by the limitations of space and the funds available. Since it was planned to use some rather expensive gases such as xenon, the tube volume of only seven liters made the cost per shot rather reasonable.

The requirements on the gas tightness of the shock tube are quite severe. In order to insure the purity of the gas in the low-pressure chamber, it is necessary to obtain an ultimate vacuum of less than 1μ but, after firing, the pressure in the tube might be as much as 500 psia. A high vacuum of better than 1μ is obtained with a VMF-10 oil-diffusion pump[*] backed by a 1405-B Welch Duo-Seal mechanical pump. A vacuum valve was especially designed to provide a one-inch-diameter opening in the tube for fast pumping but to close flush with the inside wall of the tube and withstand up to

---

[*] Manufactured by Distillation Products, Inc., Rochester, N. Y.

600-psia pressure without leaking after the tube is fired.

A schematic diagram of the shock-tube plumbing is shown in Figure 10. The oil-diffusion pump is by-passed so that it can be kept hot while the tube is being pumped down to 100μ—the pressure at which the diffusion pump can be opened to the system and can start pumping. A thermocouple vacuum gauge is connected to the vacuum manifold for continuous readings while the McLeod gauge is used as a check. A thermocouple gauge is more sensitive to organic vapors than air, so a comparison between readings of the thermocouple and McLeod gauges indicates whether or not organic vapors are present in the tube. Both gauges can be read down to about 1-μ pressure. A di-butyl phthalate manometer* is used to measure the pressure of gas put into the low-pressure chamber. The rare gas is added from a 2-liter glass flask which is filled from a cylinder of "Linde" mass-spectrometer-checked gas.

The pressure in the high-pressure section is measured with a precision Bourdon gauge** accurate to 1/4% of full scale. This section is evacuated to less than 0.5-mm-Hg pressure before filling with hydrogen. The procedure is to pump out both chambers to 0.5 mm Hg and then fill the high-pressure chamber with hydrogen to a few pounds over atmospheric pressure so that any leaks will be outward. Meanwhile the low-pressure chamber is pumped down to 100μ, at which point the valves to the diffusion pump are opened. The time required to reach this point from the closing of the tube is about 4 minutes. It usually takes about one hour to pump out the tube

---

*13 mm of di-butyl phthalate is equivalent to 1-mm-Hg pressure.

**Actually two gauges were used interchangeably. One registered 600 psi full scale and the other 2000 psi. They were Ashcroft laboratory gauges manufactured by Manning, Maxwell, and Moore, Inc., Stratford, Conn.

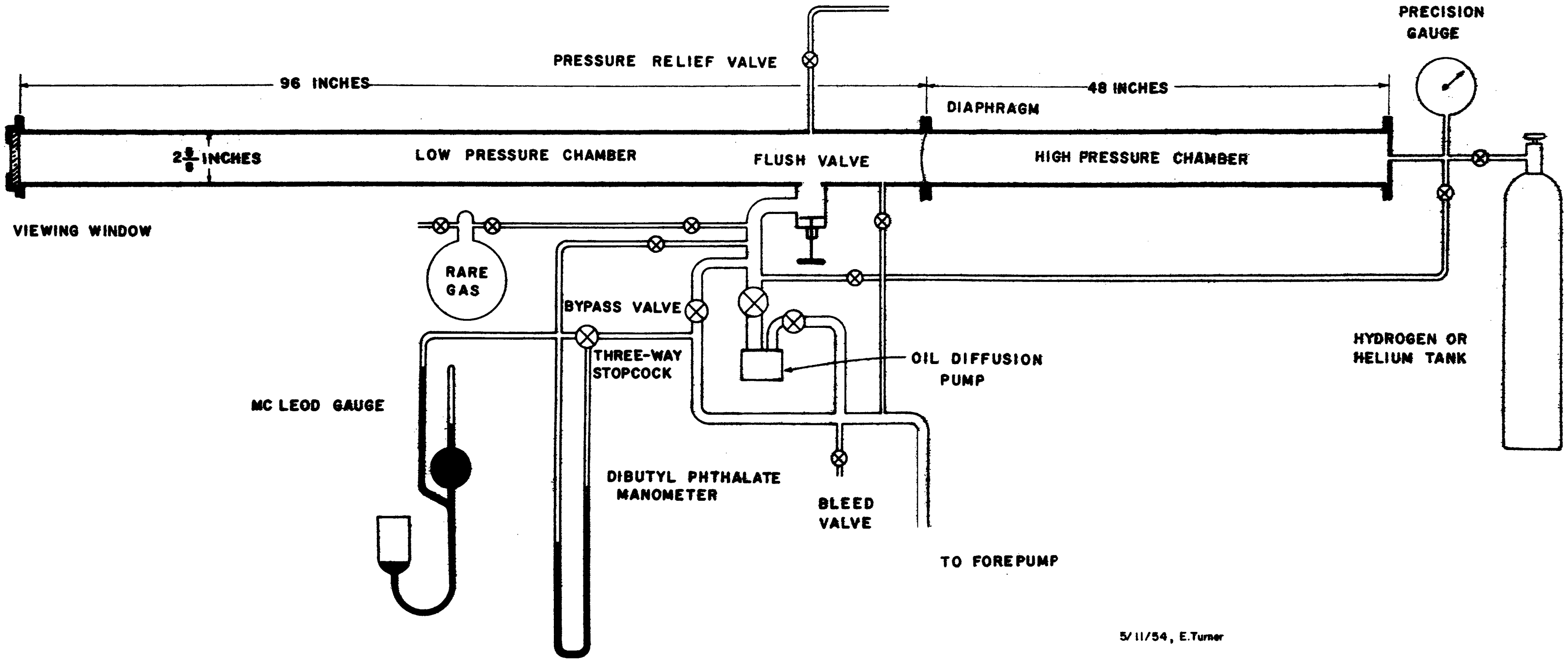

Figure 10. Schematic diagram of shock tube.

sufficiently to bring the apparent "leak rate" down to 5μ per minute, which we consider satisfactory for shooting the tube. For an elapsed time of two minutes between filling the low-pressure chamber and firing the tube, the impurity level is 10μ or 0.1% for 1-cm-Hg initial pressure. If the tube has been pumping for several hours, however, the leak rate is sometimes as low as 1μ per minute.

The diaphragm material which is used most often is cellulose acetate sheet in thicknesses of from 0.005 to 0.060 inch. It was found necessary, however, to outgas the acetate sheets for a couple of days in a vacuum chamber before they are suitable for use in the shock tube. The diaphragms are held with flat neoprene gaskets cemented to the diaphragm plates. For low pressures of up to 200 psia a single diaphragm is used, but for higher pressures two diaphragms are used in series separated by a thin chamber of intermediate pressure. A photograph of this arrangement is shown in Figure 11. The center plate has a vertical support bar to give added bursting strength to the diaphragm on the high-pressure side. A support bar was also tried on the diaphragm plate on the low-pressure side, but it had to be removed because of the adverse effect on the flow. The difficulty was that the front diaphragm would burst in two halves, one on each side of the vertical support bar, a short time apart. When the first half burst the primary shock was formed in the tube and when the second half burst a second shock was formed which caught up with the first about halfway down the tube. The amalgamation of the two shocks gave rise to a strong contact surface[29] (i.e., temperature discontinuity) in the flow behind the primary shock. A solenoid-operated prod is used to break the thinner diaphragms up to 20 mils thick, but the device was not powerful enough to break the heavier acetate sheet. Therefore one method used to fire the tube at a

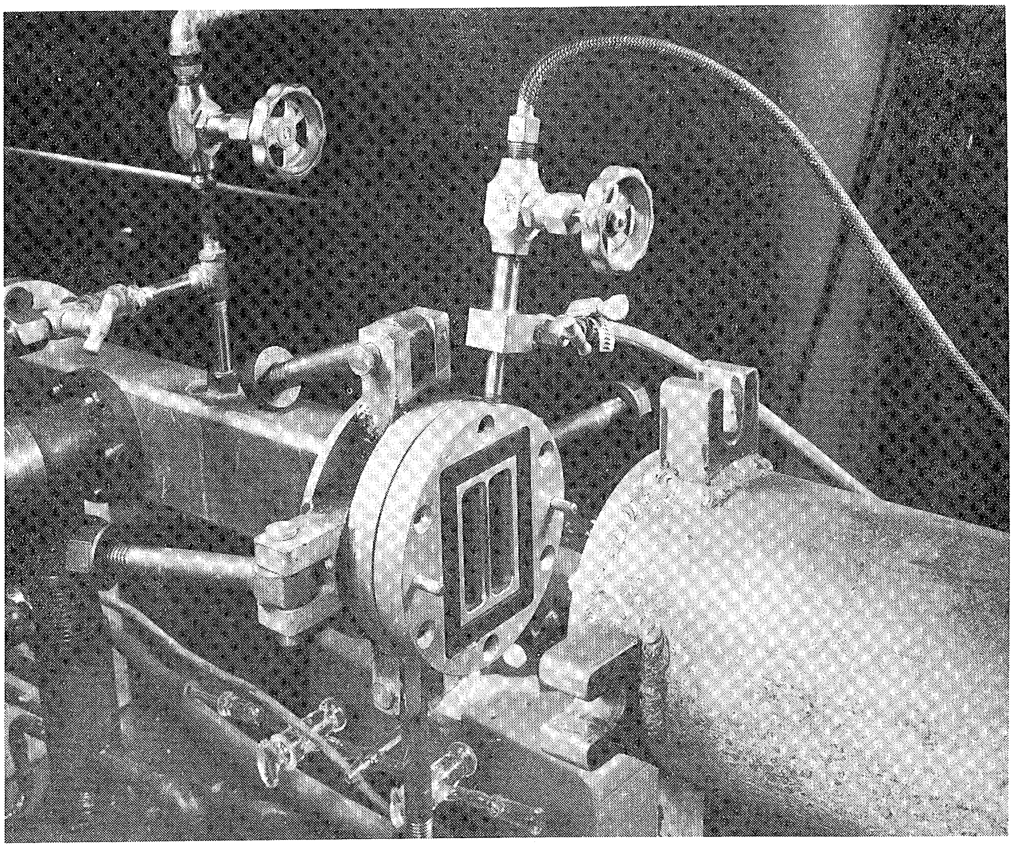

Figure 11. Photograph of diaphragm section of shock tube showing center diaphragm plate.

predetermined pressure is to release the pressure in the intermediate chamber so that the pressure difference across the rear diaphragm reaches the bursting point. The front diaphragm breaks immediately after the rear one because of the sudden excess pressure. A 10-mil-thick acetate diaphragm will hold from 120-150 psia, while a 60-mil sheet will hold about 400-psia pressure. The vertical support bar almost doubles this bursting strength.

The plumbing of the high-pressure chamber was also arranged so that an explosive mixture of hydrogen and oxygen can be used as the pusher gas. This mixture gives a large increase in shock strength. According to the graphs published by Shao-Chi Lin,[24] a ratio of O_2 to H_2 of 0.15, gives, due to the high temperatures attained, a 67% increase in sound speed over hydrogen for a constant-volume combustion.

A mixture of 18 psia of oxygen and 120 psia of hydrogen is usually used with a 0.010-inch-thick, soft copper diaphragm. Attempts to prevent the copper pieces from flying down the tube were unsuccessful and the end of the aluminum test section sustained considerable damage. Therefore a block of tool steel was bolted into the back of the test section and this stopped further damage.

The mixture at first was ignited with the spark from an automobile ignition coil at the rear end of the high-pressure chamber, but then a peaked detonation wave travels down the tube until it reaches the diaphragm, which quickly breaks. This gives rise to an uneven flow behind the primary shock. The second method was to ignite the mixture near the diaphragm so that the detonation wave travels to the rear of the chamber, leaving behind the hot burned gas at rest. This method, however, did not work as intended. The sound speed of the burned gas behind the detonation is not much greater than pure hydrogen at room temperature. If a 0.005-inch-thick copper diaphragm is used, which breaks soon after the ignition, the shock speed is not much greater than when using a hydrogen driver gas at 1000-lb pressure. If a heavier 0.010-inch-thick copper diaphragm is used, however, the diaphragm does not break until the arrival of the reflected detonation from the rear of the tube. The pressure profile of the driver gas is still slightly peaked at the front, but the flow behind the primary shock wave, as judged by the evenness of the luminosity behind the reflected shock, is fairly constant. The resultant shocks are much stronger than when using the 0.005-inch-thick copper diaphragm.

A better method is to approach a constant-volume burning by igniting the mixture at a number of points evenly spaced along the length of the chamber and thus avoid a detonation wave. After firing, the tube is pumped out with a second mechanical pump through a liquid air trap for at least one-half hour to remove all the water from the tube.

Figure 12 is a photograph of the shock tube, showing a two-prism glass spectrograph looking into the end of the low-pressure chamber through a one-inch-thick plexiglas window. Before the test section, described below, was fabricated all the spectral observations were made in this manner. The hydrogen cylinder and high-pressure chamber are at the far end.

2. The Test Section

In order to observe the flow at the end of the tube, a special test section was constructed. One-inch-thick glass or plexiglas windows fit into the sides of the chamber to give an unobstructed view of the last eight inches of the shock tube. A vacuum seal is obtained by an "O" ring in a groove on the main chamber and a flat rubber gasket was cemented to the retaining frame which presses against the outside surface of the window. A photograph of the test section disassembled and also a photograph of the section with the slit plate are shown in the Figure 13. The slit cover plate is used to obtain wavespeed photographs according to the scheme of Figure 14. Plexiglas does not transmit very well below 3300 Å, so a 1-1/2-inch-diameter fused-quartz window was mounted in a one-inch-thick aluminum plate which can be placed in the side of the test section in the same manner as a glass window.

Ordinary one-inch-thick commercial plate glass is not strong enough for the high pressures obtained at the end of the tube. A tempered plate glass such as Libby-Owens-Ford Tuf-flex or plexiglas is suitable. The tempered plate glass is not scarred by the acetate diaphragm particles, but when a hydrogen-oxygen explosive driver was used one shot left the

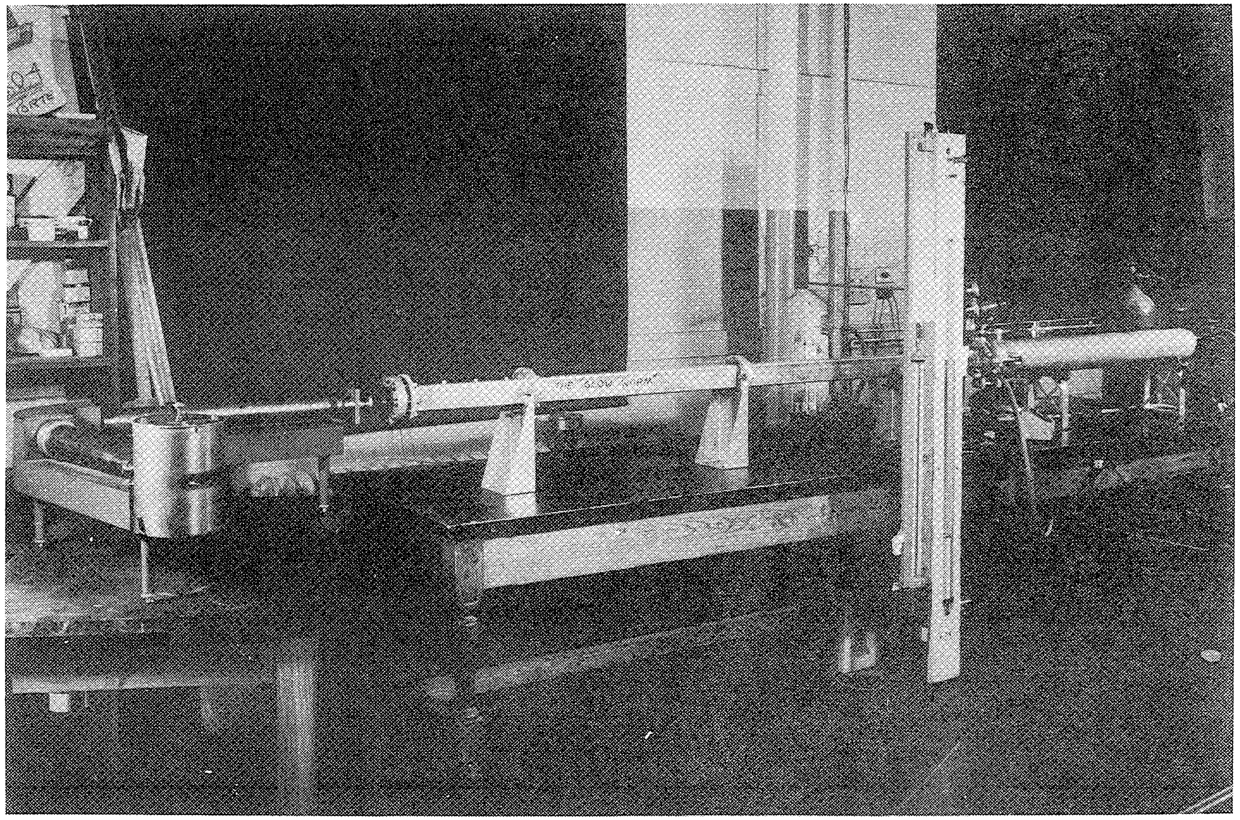

Figure 12. Photograph of shock tube.

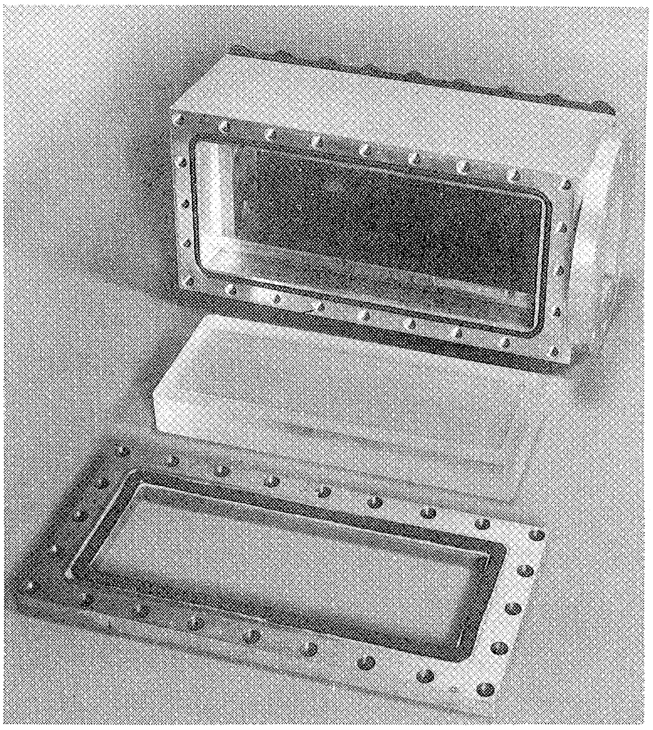

Figure 13a. Test section, disassembled to show window mounting.

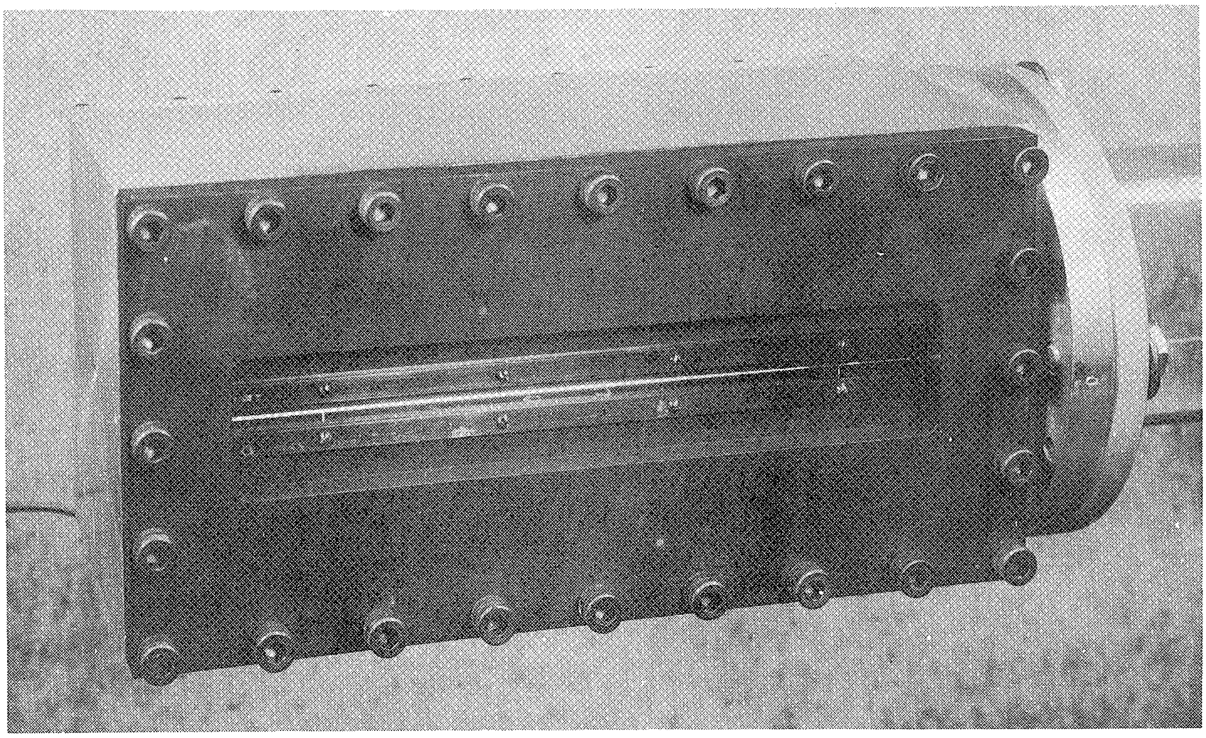

Figure 13b. Test section with slit cover plate.

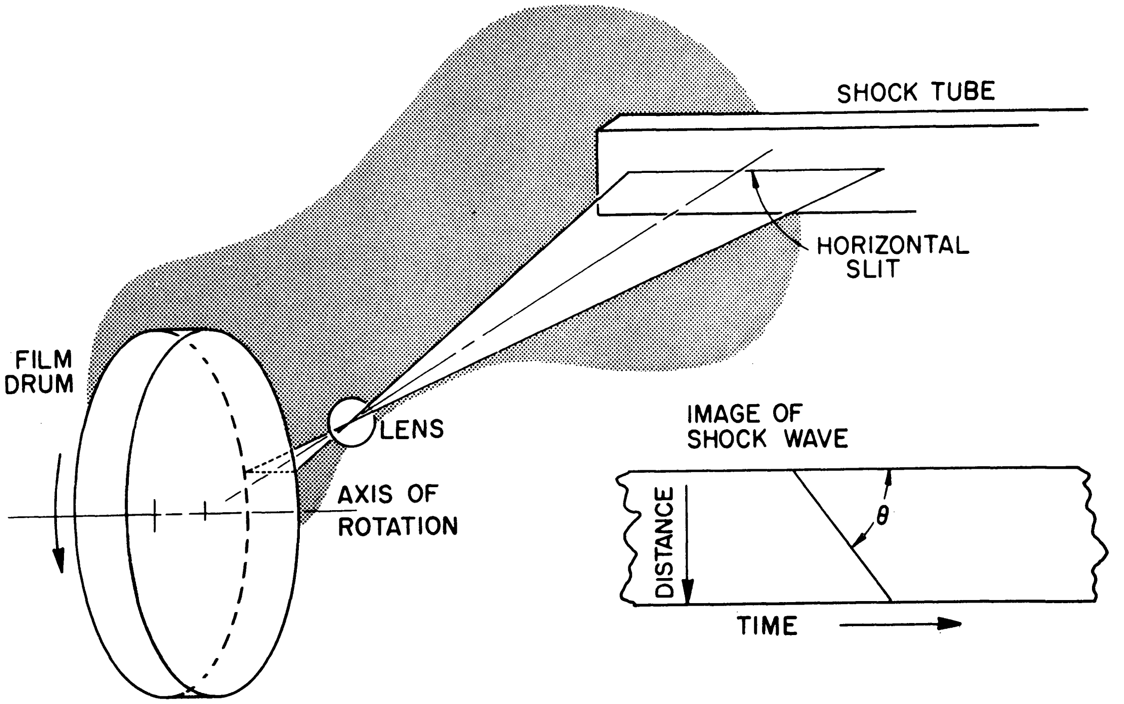

Figure 14. Schematic diagram of setup for wave-speed photographs.

glass surface with a ground appearance. Plexiglas was found to be the safest type of window to use.

3. Revolving Drum Camera

The revolving drum camera was designed to be used with a series 7 Dumore tool-post grinder. This grinder consists of a 3/4-hp, high-speed electric motor which turns the quill, on which the grinding wheel is mounted, through a belt and pulley. With a 7X-250 quill, which is used for external grinding wheels, a speed of up to 15,000 rpm may be obtained. An 8-3/8-inch-ID aluminum drum made to hold 35-mm film is mounted on the quill in place of a grinding wheel. This drum was dynamically balanced* at 10,000 rpm so that the vibration is very small. The drum is enclosed in a light-tight housing with a removable front cover on which is mounted an f/4.5, 8-1/2-inch focal length camera lens and a first surface mirror

---

*The writer is indebted to the General Motors Technical Center in Detroit for balancing the film drum.

at a 45° angle to reflect the image onto the film wrapped on the inside of the drum. A photograph of the camera on a tripod base is shown in Figure 15.

In order to focus the camera, an arm, which holds a small ground-glass screen at the same radius as the film on the drum, is put onto the shaft in place of the film drum. The image on the ground-glass screen is then viewed through the magnifier mounted on the side of the housing as the camera lens is adjusted for best focus. The film can be easily loaded into the camera in daylight by enclosing the camera in a commercial photographic loading bag which has sleeves that fit tightly over the arms. The camera cover is removed and the film, which has been cut to the correct length and put in a small light-tight can,* is placed on the inside of the drum and the cover is replaced. The speed of the drum can be varied from a few thousand rpm up to 13,000 rpm by using various pulley combinations. The camera housing begins to heat up due to air friction at 13,000 rpm, so this is the highest speed used. The speed is measured by a Hasler** revolution counter which, according to the manufacturer, is accurate to ± 1/4%. For wavespeed pictures Eastman 103-D unperforated 35-mm film has been found to be very satisfactory. It has a low fog level and can take excessive overexposures without halation. Also it does not have much curl in contrast to films like Linagraph Pan. This curl makes shock-velocity measurements more difficult because the film cannot easily be made to lie flat.

---

*A standard Kodak 35-mm-film can in which cartridges are placed has been found to work very well.

**Sold by the Hasler-Tel Co., 32 Vesey St., New York 7, N. Y.

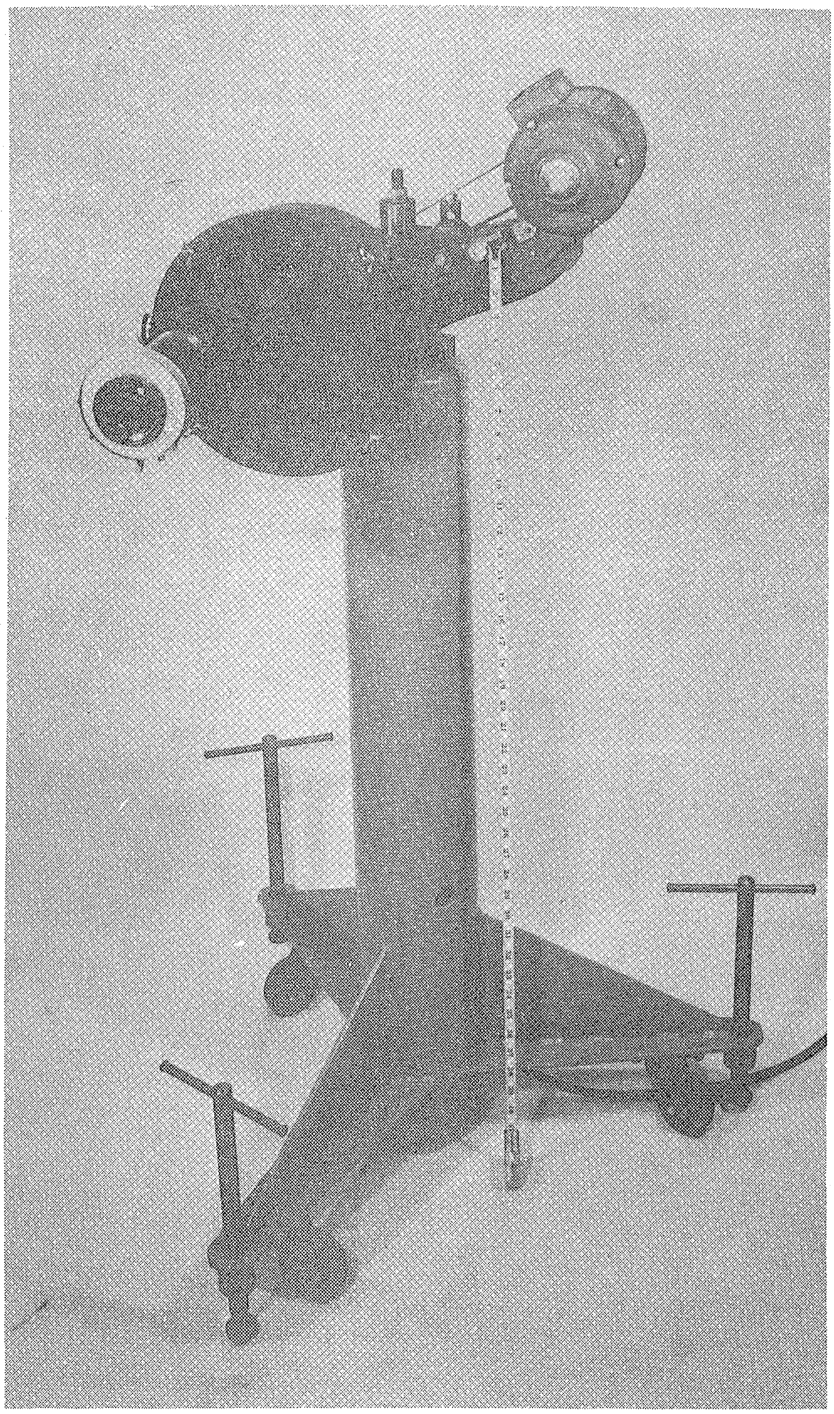

Figure 15. Revolving drum camera.

4. Spectrographs

A most important instrument for the investigation of luminosity behind strong shock waves is the spectrograph. As in astronomy, a considerable amount can be learned about the state of a luminous gas from an analysis of its spectra, or conversely, if the state of a gas is known from other measurements, information can be obtained about the physics of radiative processes.

The research profited from the availability of a good spectrograph* at the start. The instrument uses two glass prisms to give a dispersion of approximately 10 Å per mm at 4000 Å and 50 Å per mm at 5500 Å. The entire visible spectrum from 4000 Å to 6500 Å can be photographed on a 3-1/4 x 4-1/4-inch plate. The spectrograph can also be adjusted to include the infrared region up to 9000 Å, but the dispersion is very poor, only 100 Å per mm at 8000 Å. The aperture of the spectrograph is f/14, which was sufficiently fast for most of our work. This instrument was designed by Dr. Ralph A. Sawyer and built in The University of Michigan Physics Shop in 1924 by Mr. Herman Roemer, the present shop foreman.

The spectrograph at first was set up to observe the luminosity from the end of the tube (as in Figure 12), which gave both a time and space average. After the test section was built, the instrument was set up to observe into the side of the tube. A narrow cross section was focused on the spectrograph slit so that space resolution was achieved, but the spectra still represented a time average of the luminous phenomena. Because of the temperature jumps caused by shock waves which cross and recross the luminous region, quantitative data cannot be obtained from the spectra without time resolution.

---

*For the loan of this instrument the writer is indebted to Dr. C. W. Peters.

The revolving drum camera was used to provide the time resolution. A new cover plate, which had a sliding shutter but no lens, was made for the camera, and a first surface mirror mounted at 45° to reflect the spectral image onto the film. A schematic diagram of this setup is shown in Figure 16. Using a slit length of 1 mm and a drum speed of about 9000 rpm, a time resolution of 10 microseconds was obtained, which proved to be more than sufficient. This arrangement yielded very satisfactory time-resolved profiles of H_β, but it was difficult to set up and adjust. The tripod base of the revolving drum camera, for example, had to be positioned within a fraction of an inch to get sharp spectra and also the correct spectral region. Because of the temporary nature of the setup it was not very light-tight and the shock-tube shooting had to be done in almost total darkness.

The principal disadvantage of a prism spectrograph is the poor dispersion at the longer wavelengths. For the spectrograph used, the dispersion is great enough for line-broadening studies only in the limited spectral region of 3800 Å to 5000 Å. But many of the lines of interest, including the strongest rare-gas lines, are in the red and near infrared. Also, the near ultraviolet spectrum is not transmitted by the glass. For these reasons it was decided to have a grating spectrograph built with mirror optics which could transmit the near ultraviolet. For maximum flexibility the spectrograph should be able to photograph a large spectral range for survey work and also should be adaptable for time-resolved spectra by the addition of a revolving drum camera.

A spectrograph meeting these requirements was made for us by the Jarrell-Ash Co. It was a smaller 1-1/2-meter version of the Ebert type spectrograph which had been recently developed by this company.[30] The

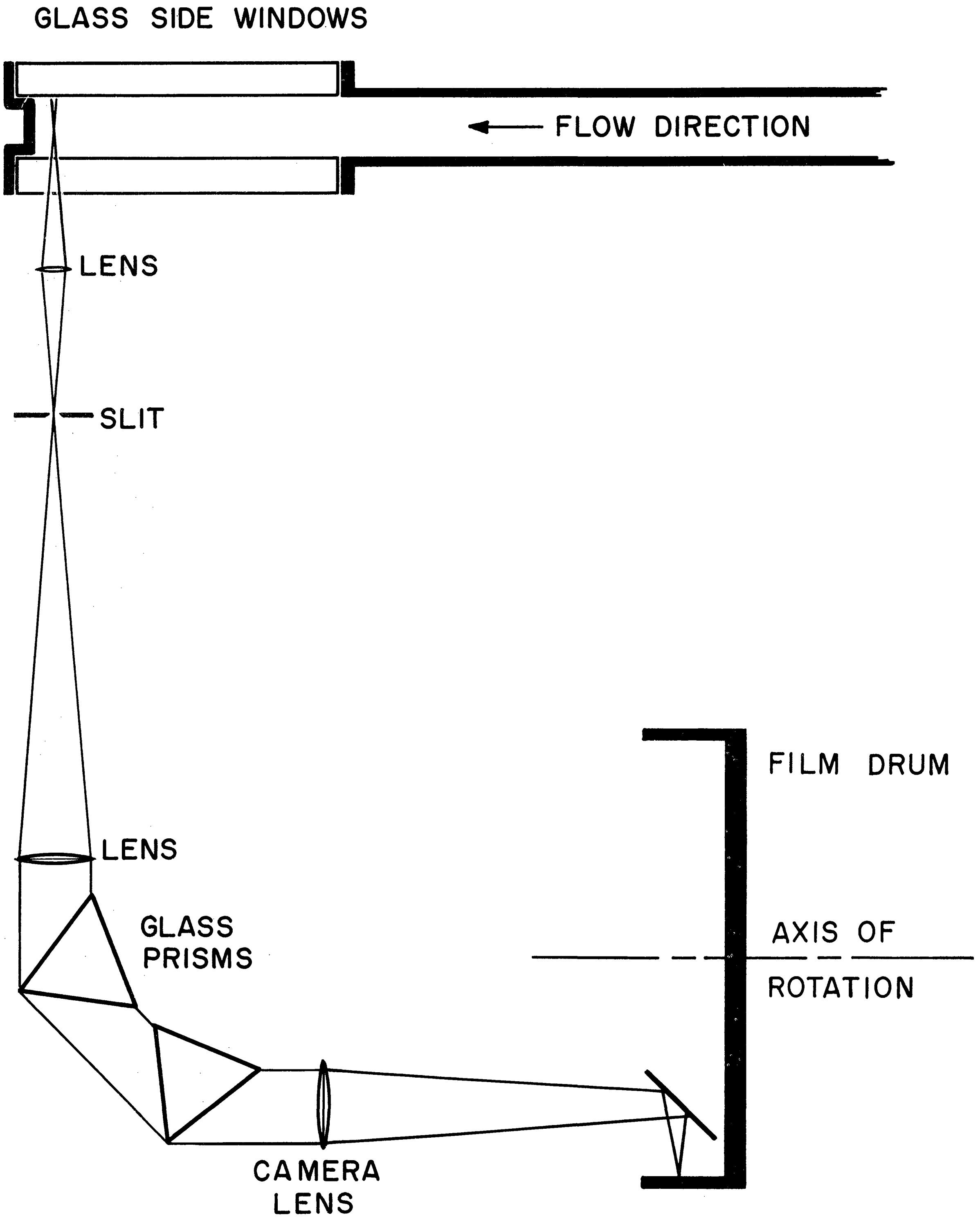

Figure 16. Schematic diagram of apparatus for time-resolved spectra.

instrument uses a ten-inch-diameter spherical mirror of 1-1/2-meter focal length and a plane grating with a ruled area of 65 x 76 mm. Two gratings are used interchangeably, one with 300 rulings per mm blazed at 7500 Å and the second with 1200 rulings per mm blazed at 5600 Å. The first is an original grating ruled by the Jarrell-Ash Co. and the second is a replica grating purchased from the Bausch and Lomb Optical Co. The average dispersions using these two gratings are 22 Å per mm and 5.3 Å per mm, respectively, in the first order. The grating table can be rotated so that any wavelength may be centered on the plate. A holder for a 4 x 10-inch plate is provided for photographing a large spectral range at one time.

A mount was made, which bolts onto the spectrograph table, for holding a revolving drum camera so that the spectrum can be focused on the film drum. The camera can be swung away from the spectrograph for loading the film. Figure 17 is a photograph of the drum camera mounted on the spectrograph. The spectrograph proper is set on foam-rubber pads to give vibration isolation from the revolving drum camera.

It is necessary to measure the primary shock velocity simultaneously with the exposure of a time-resolved spectrum since the initial pressure ratio is not a sufficiently accurate measure of the shock velocity. According to experimental results, which will be discussed in Chapters IV and V, an accurate measure of the initial pressures predicts the shock velocity only to within ± 1% at best. Since the revolving drum camera was to be used for time-resolved spectra, another method of shock-velocity measurements had to be devised. Electronic timing circuits with probes were considered, but it was finally decided to use a second revolving drum camera since it is just as accurate, more reliable, and gives more

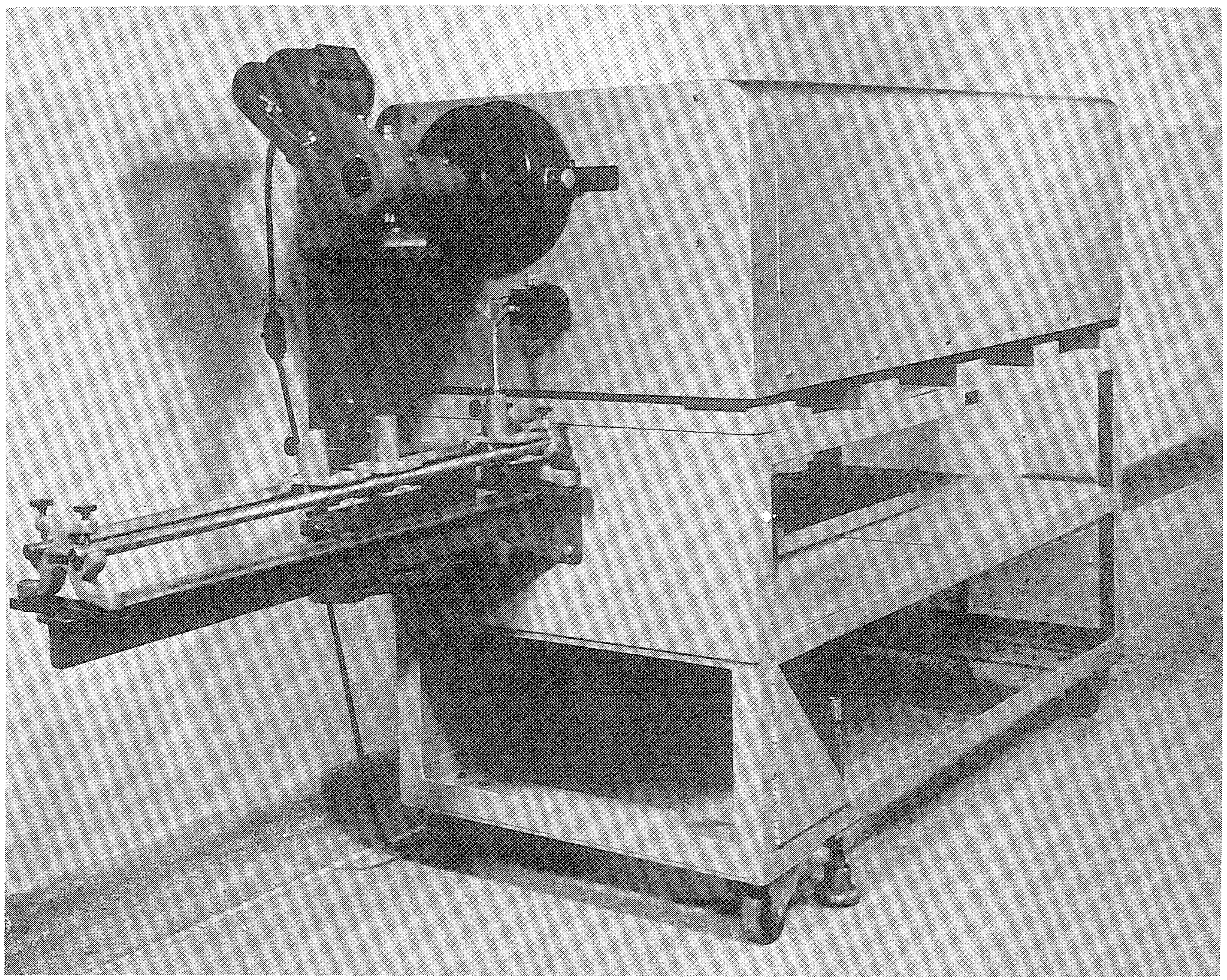

Figure 17. Grating spectrograph with revolving drum camera mounted in place.

information, especially about the reflected shocks, than electronic circuits. As one can see from Figure 12, the shock tube is close to the wall of the room. The spectrograph is placed on the left side of the test section (looking downstream), and the horizontal slit cover plate is put on the wall side of the test section. A first surface mirror is then used to reflect the light into the wavespeed camera, which is set off at an angle from the end of the tube.

It was found necessary to use fast photographic plates to obtain good spectra with one shot of the shock tube. Eastman Kodak 103-D and 103-F plates are used in the visible spectral region, 103-0 plates are used for the blue and ultraviolet, and I-N plates with a Wratten No. 16 filter are used in the infrared. The usual development time is 5 minutes in Eastman Kodak formula D-19 developer at 20°C.

Using the values for the grating area and the focal length of the spectrograph mirror given above, one finds that the geometrical aperture of the instrument is approximately f/19. This is somewhat faster than the usual spectrochemical instruments, which are about f/30, and a very good iron arc spectrum can be put on an Eastman SA-1 plate with an exposure of only 2-4 seconds (using the following method of slit illumination). For spectrochemical work the usual method of slit illumination is to focus an arc or spark on the slit with a cylindrical lens. The image of a point source is then a line along the slit. This method gives very even illumination over the entire length of the slit and therefore is well adapted to calibration methods such as a rotating sector disc. At the most only about one-fifth of the speed of the spectrograph is utilized, resulting in an exposure of perhaps 5-10 seconds instead of 1 or 2 seconds. This exposure time, however, is still relatively short for spectrochemical work. Using this method of illumination, our grating spectrograph forms exceedingly sharp spectra over the entire length of the 10-inch plate.

If, however, the luminous source is focused on the slit with a spherical lens so that the grating is filled with light, or if the luminous source is large enough to fill the grating without the use of a lens, the spectral image deteriorates badly toward the edges of the plate. Actually only the central region of 2 or 3 inches of the plate is sufficiently sharp. To get sharp spectra across the entire plate, the luminous source must be masked from the top and bottom and a cylindrical lens used to image the source on the slit. The height of the unmasked area should be determined so that, for a very short slit, a horizontal band across the center of the grating only about one-fifth the total height is illuminated. For time-resolved spectra only the central 35-mm length of the spectrum is photographed, so the lines are always imaged sharply. The writer does not understand the reason for the poor imaging under this type of slit illumination, and this information is being included in the hope it may be of help to others who may wish to use this type of spectrograph.

Recent calculations by the writer have shown that an aperture of f/19 is not sufficient to obtain good time-resolved spectra in the red and near infrared at the temperatures that can be obtained in our shock tube. There are two principal reasons for this. First of all, the maximum of the Planck black-body distribution curve is at shorter wavelengths ($\lambda_{max} \cong 2900$ Å at 10,000°K), so the near infrared is on the tail of the distribution curve where the intensity is only a fraction of the intensity in the blue. Also, the intensity on the tail of the Planck distribution curve increases only slowly with temperature. At 15,000°K the black-body radiation intensity at 8000 Å is only twice that at 10,000°K. Secondly, the I-N photographic plates, which are sensitive to the near infrared, are somewhat slower than 103-0 plates, for example, which are sensitive in the blue.

Therefore at the time of this writing another spectrograph is being built which will use the 1200-line-per-inch grating mentioned above and an f/5.6, 20-inch focal length, aerial camera lens. The dispersion will be approximately 16 Å per mm and the geometric aperture will be f/6.7. The speed will be about eight times that of the previous grating spectrograph and the dispersion will still be adequate for line-broadening studies.

With a few exceptions, the experimental apparatus has proven to be very satisfactory. The shock tube with the test section and vacuum plumbing was relatively inexpensive, but yet it has been quite versatile and has fulfilled all the requirements necessary for the production of very strong shock waves. Possibly the attenuation of strong shock waves can be reduced by polishing the inside walls very smooth, but this has not been investigated. The revolving drum cameras were very easy to build, costing less than 1000 dollars each, including the mounts, and they have been most valuable in this research. The problem of the appropriate spectrograph has been more difficult to solve, and at present it seems to the writer that no single spectrograph can meet all the requirements. In spite of this, however, many valuable data have been obtained from spectroscopy.

CHAPTER IV

EXPERIMENTAL OBSERVATIONS OF FLOW

1. Qualitative Description of Wave-Speed Pictures

Most of the observations of the flow in the shock tube were made by photographing a horizontal slit on the side of the test section with a revolving drum camera, as shown schematically in Figure 14. Photographs obtained in this manner are called wave-speed pictures, and they are essentially x-t plots of the shock waves and luminous phenomena in the shock tube.

Figure 18 is a wave-speed photograph of shock waves produced by firing hydrogen at 600-psia pressure into 1-cm-Hg pressure of argon. The shock velocity is approximately eight times the speed of sound of the gas ahead of the shock front. The primary shock wave appears at the left as a thin luminous line. An explanation for this phenomenon will be given in Section 5 of this chapter. The end of the tube is at the right-hand side of the wave-speed picture. The primary shock wave upon meeting the end of the tube is reflected, and the sudden increase in temperature is evidenced by the intense luminosity behind the reflected shock wave. The original film was so black that to make a usable enlargement this region had to be exposed for a much longer time than the primary shock to bring out the detail. The luminosity ceases when the reflected shock meets the cold hydrogen interface, and one can dimly see a shock wave, which results from this interaction, moving back into the luminous gas and reflecting off the end of the tube. The gas is heated by each passage of a shock wave. When a shock is reflected from the interface, the flow velocity, and hence the velocity of the

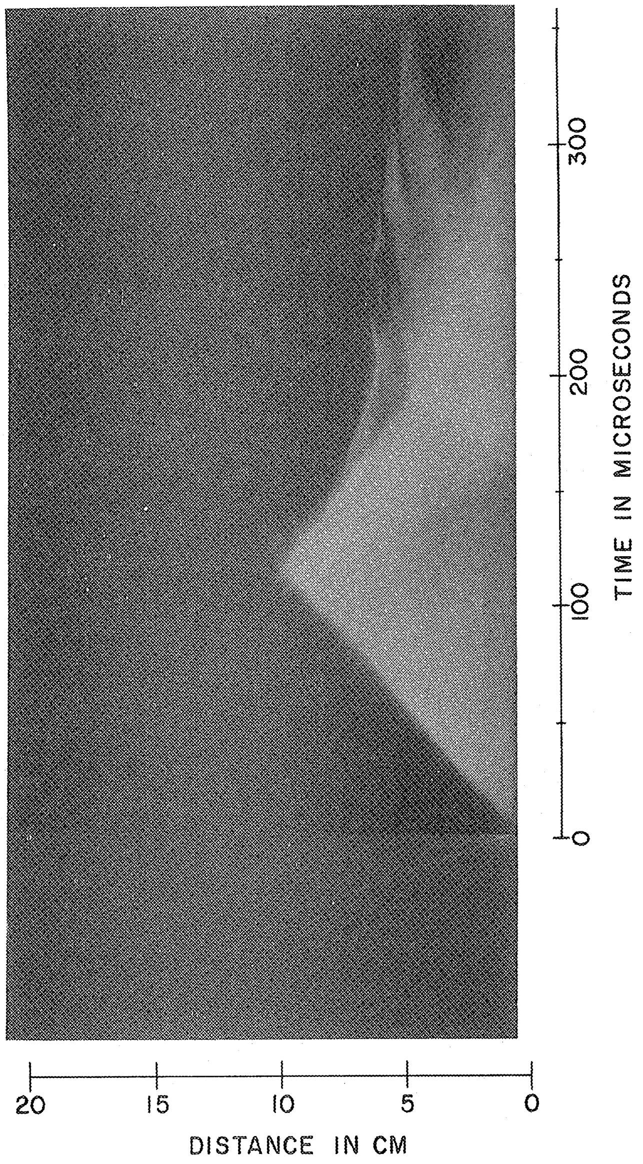

Figure 18. Wave-speed picture of shock waves in argon.

interface, is still in the positive direction (toward the end of the tube). Because of this and the spreading of the interface, which will be discussed later in this chapter, the luminous region decreases rapidly in size with time. Figure 18 therefore constitutes experimental evidence of the prediction made in Chapter II, Section 2, and of the schematic diagram shown in Figure 8, Case A. In the range of shock strengths studied, a shock wave usually resulted from the interaction of the reflected shock with the interface. The case of the reflected rarefaction was not often observed, even for xenon, for reasons discussed in the next section.

2. Shock-Velocity Measurements

If the speed of the revolving drum camera and the object-image ratio are known, the shock velocity can be computed from a measurement of the angle of the shock-wave image on the film. For each shot the drum speed is measured with a revolution counter accurate to ± 1/4%. The object-image ratio is found by making two white marks six inches apart on the horizontal slit jaws, which are then photographed with the film drum stationary. In order to provide a reference from which the shock-wave angles can be measured, this calibration picture is made with the slit illuminated from behind. A correction must be made in the object-image ratio because the horizontal slit is a finite distance from the center of the test section. If one observes the calibration marks on the horizontal slit from the position of the revolving drum camera, he actually sees a slightly greater distance at the central axis of the tube because of parallax. For our test section the slit was effectively 2.5 inches (including the effect of the index of refraction of the window) from the center of the tube and the camera was about 72 inches from the horizontal slit. The correction was therefore

$$\frac{72 + 2.5}{72} = 1.035 \quad .$$

The film was placed in a photographic enlarger* and the shock waves were traced on a sheet of paper from which the measurements were made. It is estimated that these measurements were accurate to ± 1/2%, resulting in an accuracy of shock-velocity determination of approximately ± 0.56%. One must be very careful in using an enlarger since many enlarger lenses have a large amount of distortion. Recently this project has purchased a comparator with a protractor eyepiece so that the angles can be measured directly from the film. This promises to be a more accurate method of shock-velocity determination.

Shock-velocity measurements were made in argon and xenon over a wide range of initial pressure ratios and in krypton and neon for only narrow ranges of initial pressure ratios. In Figure 19 are plotted the observed shock velocities vs initial pressure ratios. Also are shown curves of shock velocity vs initial pressure ratio computed from ideal theory. The experimental shock velocities are not shown for neon, but these will be discussed in the next chapter. The shock velocities are given in terms of the dimensionless variable M_s which is defined as the ratio of the shock velocity to the sound speed of the gas ahead of the shock.** It is often called the shock Mach number, but it should not be confused with the flow Mach number, which is the flow velocity in the laboratory coordinate system divided by the local sound speed of the gas. The initial pressure ratio,

---

*Leitz Focomat enlarger with f/2.0 Summar lens.

**M_s is related to the primary shock strength y_{21} by the equation $M_s = \sqrt{\mu y_{21}+1}/\sqrt{\mu+1}$ if ionization is neglected. This relation is also approximately correct for degrees of ionization up to a few percent.

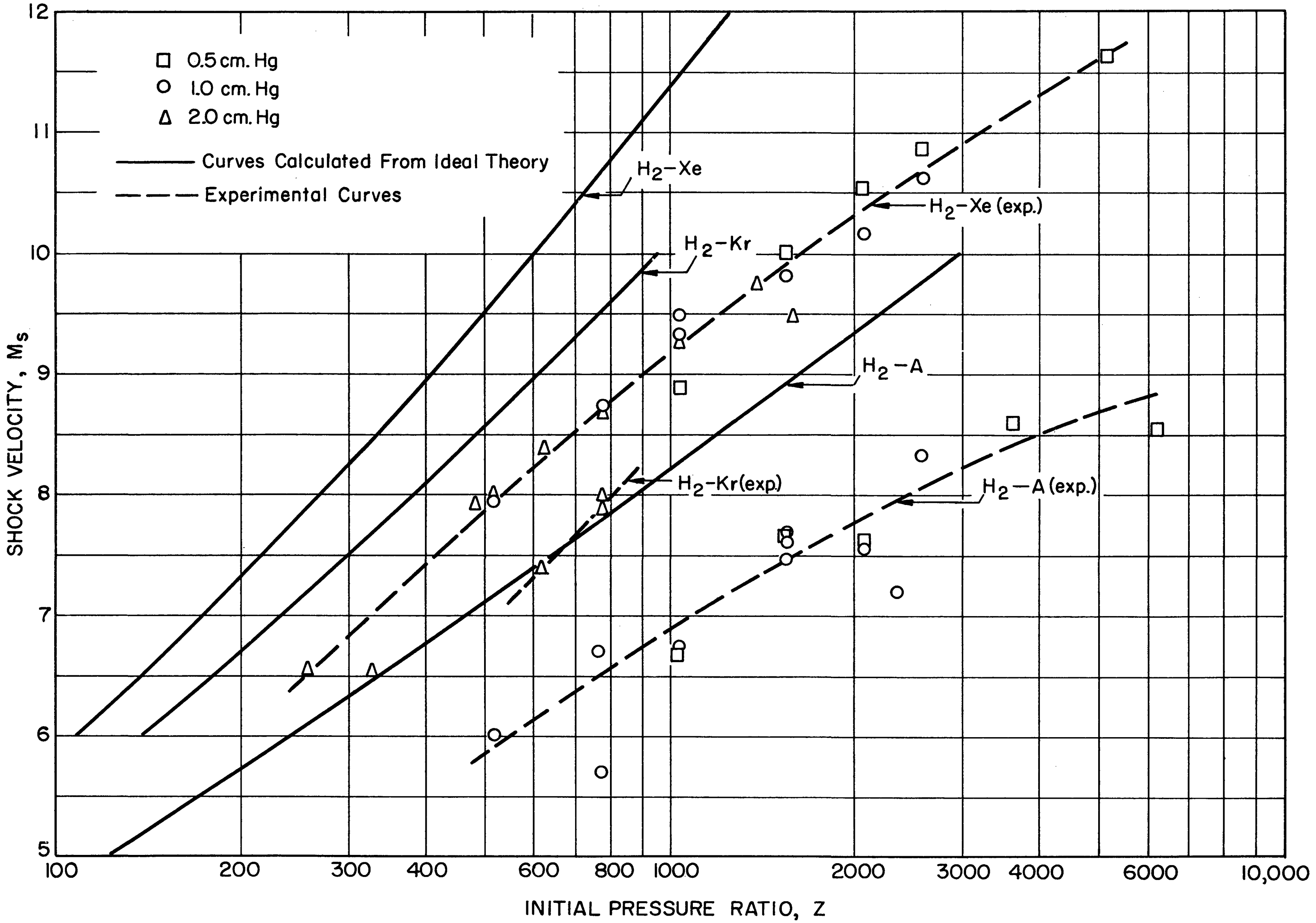

Figure 19. Shock velocities vs initial pressure ratios.

p_4/p_1, is denoted by Z.

The experimental points for xenon can be fitted with a smooth curve rather well, but the shock velocities are considerably below the ideal theory. (The experimental points for argon are, for some unexplained reason, somewhat more scattered than for xenon, but the trend is the same.) Although ionization usually occurred behind the primary shock in xenon, the decrease in shock velocity cannot result from a change in the hydrodynamic variables due to ionization since neither the flow velocity nor the shock strength depart much from the ideal theory as the shock velocity, and hence ionization, increases (see the graphs in Reference 14). For the stronger shocks in xenon the radiation behind the primary shock becomes very intense, so a part of the decrease in shock velocity may be due to energy loss by radiation. In argon, however, there was no luminosity behind the primary shock for even the strongest shocks obtained. It appears therefore that there is a rather large attenuation of shock velocities in the tube for these very strong shocks due to friction at the walls, heat losses to the walls, or both.* The practical effect of this attenuation is that initial pressure ratios of from two to four times larger than predicted theoretically are necessary to obtain a given shock strength.

No satisfactory wave-speed pictures were obtained showing a rarefaction wave reflected from the interface, even in xenon where the critical shock strength was calculated to be $y_{21} = 163$, according to the ideal theory (see Table III, Chapter II). At shock strengths below the critical value a rarefaction wave should be reflected from the interface when it is hit by the first reflected shock, but at shock strengths as low as $y_{21} = 80$

---

*Hollyer[11] has made a theoretical and experimental study of shock wave attenuation due to these factors at somewhat lower shock strengths (y_{21}=5-20).

in xenon the interface still appeared to be moving toward the end of the tube after the interaction with the first reflected shock. This would seem to indicate a shock reflected from the interface rather than a rarefaction. A shock, even if it were present, could not be distinguished in the wave-speed pictures, however, because of the extreme blackening of the film in the region behind the first reflected shock.

There are two effects which would lower the critical shock strength. First of all the high pressure, p_4, required to produce a given shock strength is at least twice as much as predicted theoretically. The cold gas is therefore expanded more, resulting in a colder gas than predicted theoretically. The second effect is that ionization behind the reflected shock lowers the reflected shock strength somewhat. From Figure 6 one can see that both of these effects are in the proper direction to lower the critical shock strength. Calculations, however, have shown that these two effects combined do not account for the apparently large reduction in the critical shock strength. One possibility is that the spreading of the interface gives the appearance of motion toward the end of the tube, after the interaction with the reflected shock, by quenching of the luminosity, although the center of the interface is actually moving in the other direction.

The velocities of the reflected shock waves were also measured from the wave-speed films. This was possible only in argon and neon, however, because in xenon the intense luminosity behind the reflected shock gave rise to considerable scattering and halation on the film so that velocity measurements were very inaccurate. The experimental points for argon are shown on the graph of U'/c_1 vs M_s in Figure 20, together with a curve of reflected shock velocities predicted by ideal theory, i.e., not consider-

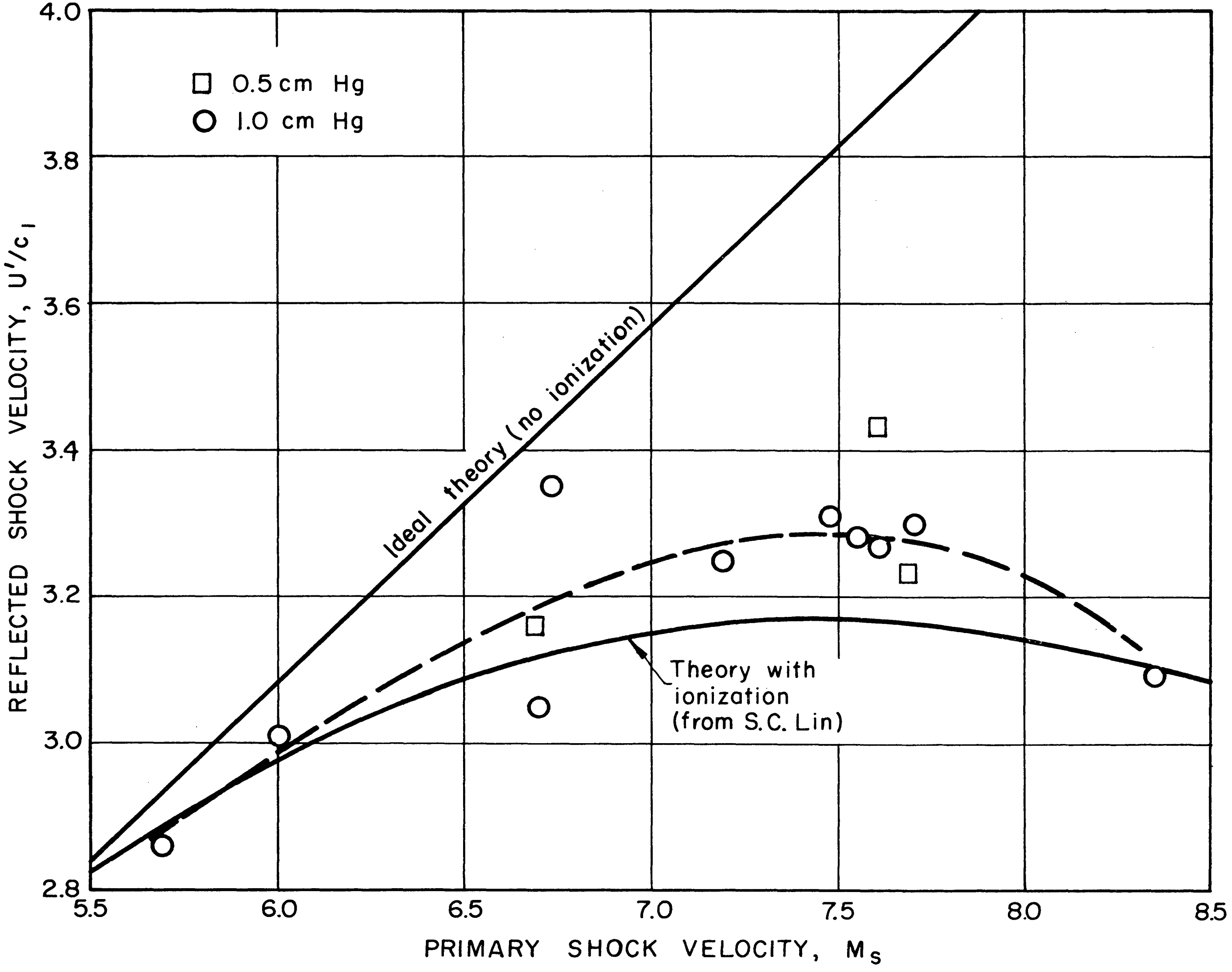

Figure 20. Reflected shock velocities vs primary shock velocities in argon.

ing the effects of ionization. Also shown is the theoretical curve for reflected shock velocities, taking into account the effect of ionization. This curve was obtained from the paper by Resler, Lin, and Kantrowitz.[14] The reason that the reflected shock velocity with ionization falls below the ideal theory can be seen from equations (2.20) and (2.25) which are rewritten below for the reflected shock.

$$X_{52} = \frac{4y_{52}+1}{y_{52}+4-2\alpha_5\frac{\theta}{T_2}}$$

$$(U'-u_2)^2 = RT_2 \frac{X_{52}}{X_{52}-1}(y_{52}-1)$$

The pressure ratio y_{52} across the reflected shock is affected only slightly by ionization, but the density ratio x_{52} is increased. This in turn reduces the reflected shock velocity. In fact, the reflected shock velocity would seem to be a good indication of the amount of ionization.

The experimental points fall mostly a little above the theoretical curve, indicating slightly less than equilibrium ionization. One possible explanation might be that energy losses due to radiation and heat conductivity to the walls reduce the temperature and, hence, the ionization. This effect, however, has not been computed.

3. Delay Time for Ionization Equilibrium

A very interesting phenomenon observed in xenon shots is the finite delay time for ionization equilibrium to be attained behind the primary shock wave.* This is shown by the series of wave-speed pictures of shots into xenon in Figure 21. The shock velocities increase from $M_s = 8.9$ to

---

*This phenomenon was observed previously by Kantrowitz and co-workers in argon.

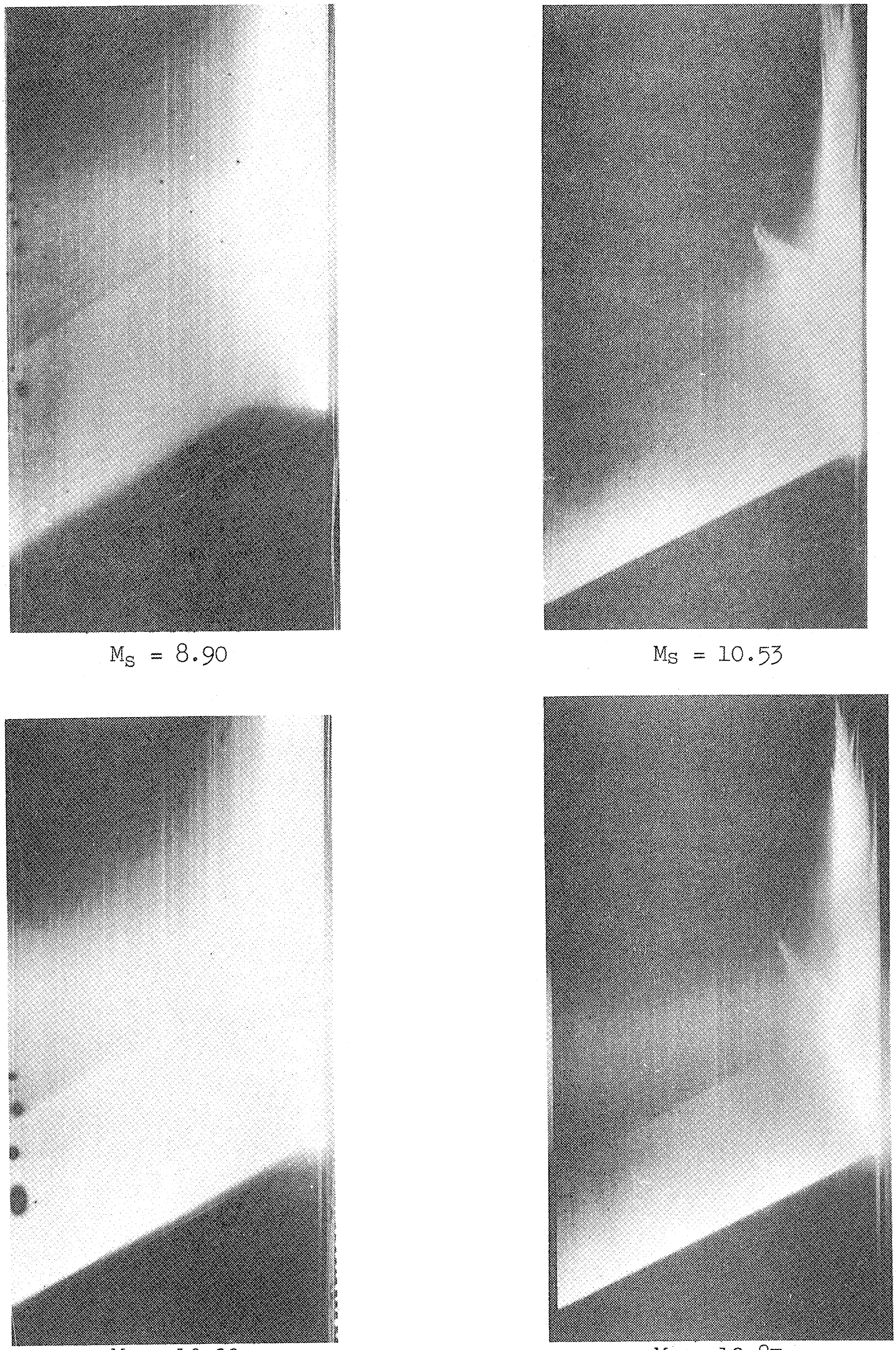

M_s = 8.90

M_s = 10.53

M_s = 10.00

M_s = 10.87

Figure 21. Series of wave-speed photographs of shock waves in xenon (p_1 = 0.5 cm Hg).

10.9 in the series. As in Figure 18, the time axis is vertical and increasing upward while the distance axis is horizontal and the end of the tube is at the right-hand side of the picture. The primary shock wave appears as a sharp luminous line at the left. After reflection the luminosity becomes so intense that the outline of the reflected shock is not sharply defined due to the scattered light and halation in the film.

There is a dark space behind the primary shock, followed by luminosity which extends back to the interface.* This onset of luminosity is well defined and is interpreted as the point at which ionization equilibrium is reached. One can see from this series of pictures how the delay time decreases with increasing shock strength. Also, for the two strongest shots the luminosity can be seen to decrease with distance behind the front before it is finally quenched at the cold hydrogen interface. This decrease is due to the energy lost by radiation and has been investigated quantitatively in argon by Kantrowitz _et al_.[17]

Measurements of the delay time were made at a range of shock strengths for initial xenon pressures of 0.5 cm, 1.0 cm, and 2.0 cm Hg, and the experimental points are plotted on the graph of Figure 22. The delay time plotted on this curve is the actual time for a small volume of gas to become ionized after passing through the shock front. If this time be designated by Δt and the delay time measured along the time axis of the wave-speed photograph by $\Delta\tau$, then the two are related by the equation

$$\Delta t = \frac{U}{U - u_2} \Delta\tau$$

---

*In the first two pictures the interface, which is the end of the luminosity, is masked somewhat by the strong scattered light from the intense luminosity behind the reflected shock.

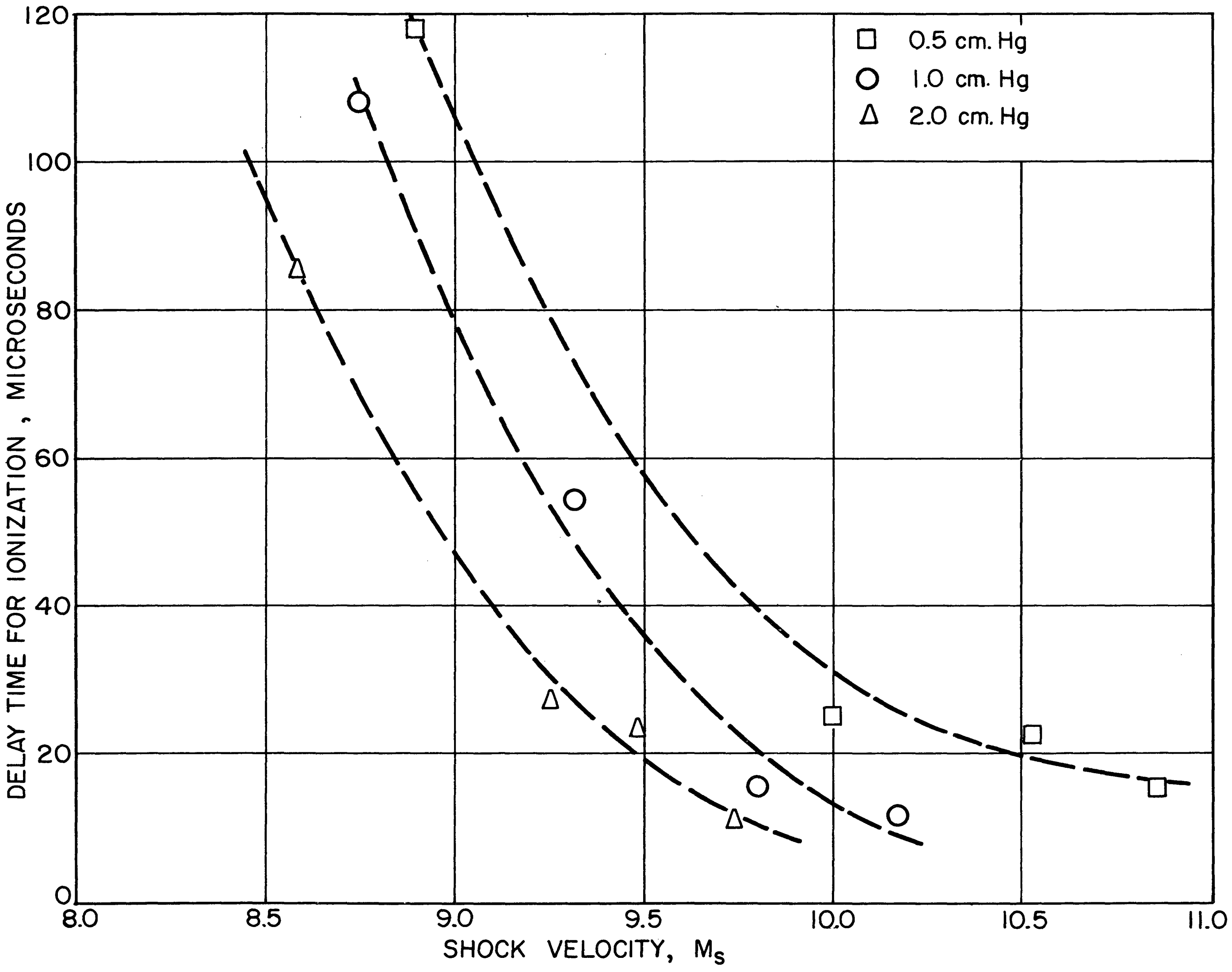

Figure 22. Delay time for ionization in xenon vs primary shock velocity.

which is derived by the following considerations. If the luminous front is a distance Δx behind the shock, it will appear at a particular point at a time $\Delta \tau$ after the passage of the shock given by $\Delta \tau = \Delta x/U$. But now the actual time for a small mass of gas to traverse this distance Δx is $\Delta t = \Delta x/(U-u_2)$ since $(U-u_2)$ is the flow velocity relative to the shock front.

The decrease in delay time is at first very rapid and then starts leveling off with increasing shock velocity. The error in the measurement of $\Delta \tau$ was approximately ± 15%. The reasons for this were that the onset of luminosity was not absolutely sharp and the measured $\Delta \tau$ varied from one point to another. Also there were often dark streaks exhibiting the angle corresponding to the flow velocity in the luminous region. These are apparently regions of un-ionized gas moving with the flow. Such a dark streak is apparent in the wave-speed photograph for $M_s = 10.0$.

A theory to explain the delay time for ionization behind a strong shock front in argon was developed by John W. Bond, Jr.[26] He assumed that immediately behind the shock front there is no ionization and that the initial process for the production of electrons is the very inefficient reaction

$$A + A \rightarrow A^+ + A + e$$

The small number of electrons produced in this manner then enter into the far more efficient reaction

$$e + A \rightarrow A^+ + 2e$$

with, of course, the inverse reaction also taking place,

$$e + A^+ \rightarrow A + \text{radiation},$$

Bond concludes that there is a distance behind the shock front, which he calls the onset width, where the amount of ionization is very small. At this point, however, the transfer of energy from the translational degrees of freedom to ionization proceeds very rapidly by the second process above until equilibrium is reached. The onset width is the major portion of the total width required for ionization to reach its equilibrium value.

Because Bond's calculations were for argon, while our experiments were done with xenon, his theory cannot be confirmed in detail with our results although certain features seem to fit his predictions. He states, for example, that the delay time should be inversely proportional to the density of the gas ahead of the shock. The curves shown in Figure 22 do confirm this prediction. For a given shock velocity the delay time is approximately twice as long for $p_1 = 0.5$ cm Hg than for $p_1 = 1$ cm Hg and about four times as long as for $p_1 = 2$ cm Hg. Bond's theory therefore seems to explain qualitatively our results on the delay time for ionization.

In the range of shock strengths up to $M_s = 8.6$ in argon, no luminosity was observed behind the primary shock wave. The temperature behind the primary shock wave was too low to produce appreciable ionization, and also, according to the foregoing discussion, the delay distance for ionization was probably far greater than the entire hot flow. However, behind the reflected shock waves the phenomenon of the delay time for ionization was observed both in argon and neon.

Very recently more wave-speed photographs were made in order to check a few points on the curves of delay time vs shock velocity in xenon. The new pictures show delay times approximately five times as great for the same shock velocities. This result was very disturbing, so a series of four wave-speed pictures, with $p_1 = 1$ cm Hg, was made over a range of shock velocities from $M_s = 9.0$ to 10.2. These points defined a fairly smooth curve showing that the discrepancy in delay times was not due to only one or two isolated shots. The principal difference between the previous and the new experiments was that xenon from a steel cylinder of mass-spectrometer-checked gas (a gift from Linde Air Products) was used for the old experiments while xenon from a flask of spectroscopically pure xenon (also from Linde Air Products) was used for the new experiments. The flask of xenon was checked with a mass spectrometer after the shock-tube experiments were completed and was found to contain less than 0.1% of air. This is about the same amount of air that leaks into the shock tube in the time it takes to fire.

These results do not give sufficient information to discover the exact cause of the difference in delay time, but it appears that it is very sensitive to the amount of impurities present and that a small amount of impurity decreases the delay time. This could be expected from Bond's theory. The initial rate of production of electrons would not depend so much on collisions between the rare-gas atoms as on collisions with atoms and molecules of impurities.

4. The Shock Front

As one can see from the wave-speed photographs in Figures 18 and 21, the primary shock front appears as a thin luminous line even though there may be no luminosity behind the front. This phenomenon was first reported by Petschek,[31] working under Prof. Arthur Kantrowitz at Cornell University. He determined that for a shock wave in argon with a velocity of $M_s = 7$, the thickness of the luminous front was less than 0.6 mm. The writer has found that the primary shock fronts are not visible on the wave-speed photographs at shock velocities below $M_s = 5$. From $M_s = 6$ to 7 the shock front appears somewhat diffuse, but above $M_s = 8$ it is extremely thin and sharp. The appearance of this front was considered to be a very strange phenomenon inasmuch as it was not predicted by theories of the shock front. There were several speculations about the character of the shock front that would be necessary to produce such a thin luminous front, but these could not be verified or disproved because of the lack of experimental data. In particular, a spectrum of the luminosity from the front had not been obtained because the front moved too fast and was too thin to give a sufficient amount of light.

The first experiment that was made in an attempt to explain this thin luminous front was to take a wave-speed photograph in krypton with the revolving drum camera at an angle of 8-1/2° to the perpendicular from the test section. If the luminosity were a wall effect, one would expect to see two luminous lines, one from each wall of the tube. The front, however, was spread out evenly, indicating that the luminosity extended across the tube.

A second experiment was to place a Bausch and Lomb wedge interference filter in front of the horizontal slit on the test section and take a wave-speed photograph of a shot in krypton in the usual manner. The filter was three inches long and the transmission varied from 7000 Å at one end to 4000 Å at the other. The idea was that the positions along the filter at which luminosity of the shock front was transmitted would indicate the wavelengths present in the spectrum. A calibration picture was made by photographing a krypton Geissler tube through the filter. The resulting wave-speed picture showed that the luminosity consisted of a line spectrum rather than a continuum, but the pattern did not match the calibration picture of the krypton discharge tube. The only alternative was that the luminosity must be due to impurities, but the resolution of the wedge interference filter was too poor to make any identification.

At this point Prof. C. W. Peters suggested the experimental setup shown in Figure 23. The horizontal slit on the side of the test section is imaged on the vertical spectrograph slit by a lens and a Dove prism turned at 45°, and the spectrum is imaged on the film drum. As the shock front moves down the tube, its image, spread out in a spectrum, moves upward on the film. If the film drum is rotated at the correct speed, the spectrum of the shock front can be made to appear stationary with respect to the film. Thus, the shock front can be followed for a distance down the tube, resulting in a large increase in exposure time.

Figure 24 shows a spectrum obtained in this manner, but the synchronization was not close enough to define the front clearly. The luminosity was found to consist of the C_2 "Swan" bands, the violet CN bands, and the lines of sodium and calcium. The molecular bands probably result from the breaking up of organic vapors at the shock front, while the metallic lines come from dirt stripped off the walls. We believe that the sharpness of the front is caused by the dissociation of C_2 and CN into carbon and nitrogen atoms, which do not radiate so easily. The temperature behind the shock front for $M_s = 8$ is more than 6000°K and the dissociation energy of C_2 is only 3.6 volts, causing the C_2 to be quickly dissociated.

Richard J. Rosa, at Cornell University, independently developed a technique somewhat similar to the above for photographing the spectrum of the shock front and also found the luminosity to be caused by C_2, CN, Na, and Ca. These results were reported simultaneously by Rosa[32] and the writer[33,34] at the 1955 Washington meeting of the American Physical Society.

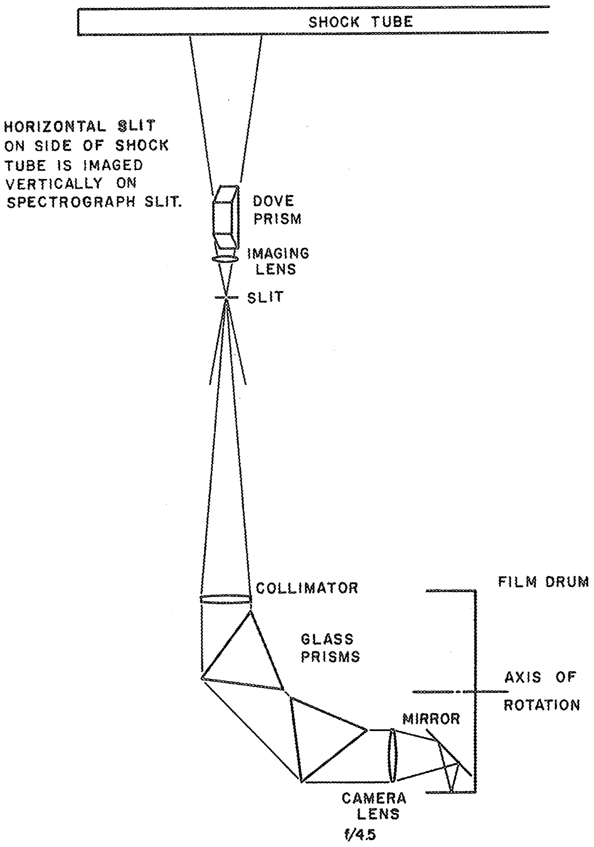

Figure 23. Experimental setup for obtaining synchronized spectra.

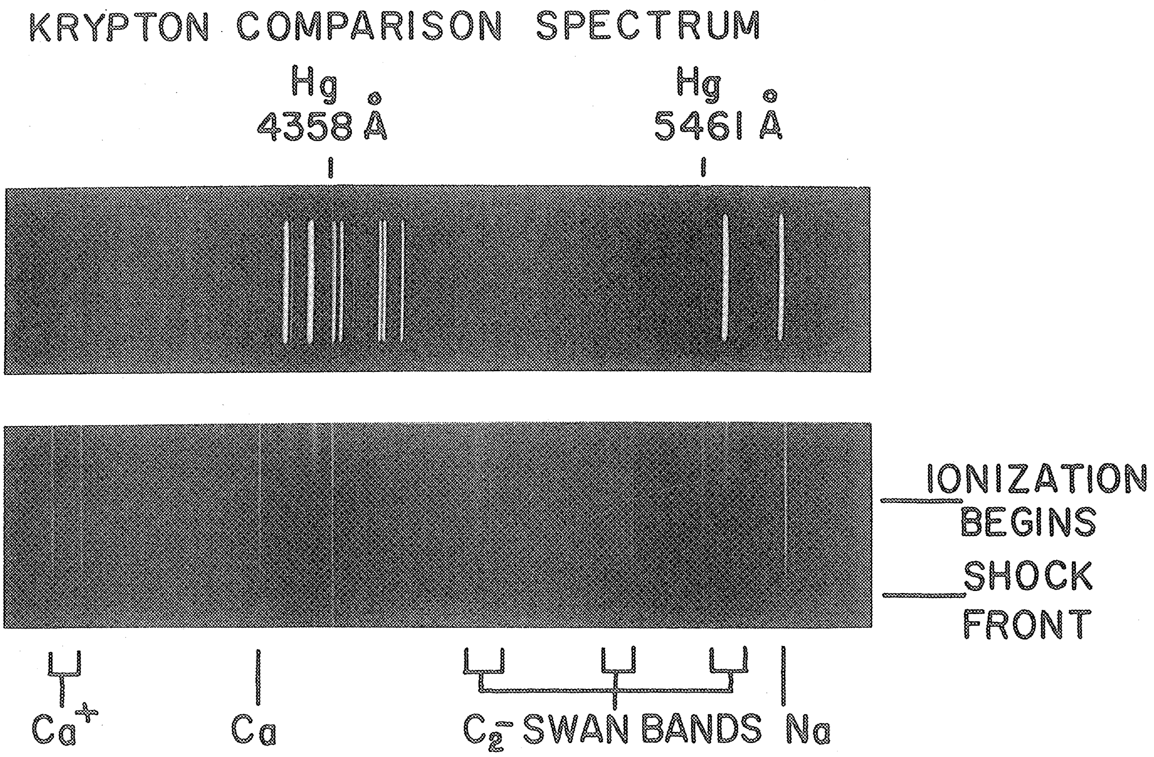

Figure 24. Synchronized spectrum of shock front in krypton.

5. The Interface

Ideally one would like the diaphragm between the high- and low-pressure gases in the shock tube to be removed instantaneously so that the interface between the two gases would be thin and plane. Practically, however, this condition cannot be realized. Mautz[8] and Geiger[9] have taken excellent photographs of the bursting of a thin diaphragm and the subsequent formation of a plane shock wave in the shock tube. They found that it took about 100 microseconds for the diaphragm to rupture completely, and that, as a result, the interface was very turbulent and contained much vorticity. It should be expected that with the use of heavy diaphragms, necessary to hold several hundred psia without bursting, the rupture process would be even slower, resulting in a considerable amount of turbulence and vorticity at the interface.

In order to observe the interface in our shock tube, a photograph was taken of the luminosity behind a strong shock wave in xenon and the border of the interface showed up by the quenching of the luminosity. The photograph, which is shown in Figure 25, was made in the following manner. The window of the test section was covered except for a narrow vertical slit which was then imaged crosswise of the film of the revolving drum camera as shown in Figure 26. The luminosity moving by the vertical slit gave the same result as if a focal-plane shutter had been used with an effective exposure time of about one microsecond. This method was used previously by Prof. Arthur Kantrowitz and his co-workers. For the shot in Figure 25 the initial xenon pressure was 1 cm Hg and the shock velocity was estimated to be $M_s = 10.2$. One can clearly see the thin luminous shock front, the onset of ionization, the decrease in luminosity due to radiation, and, finally, the quenching of luminosity by the cold hydrogen interface. This

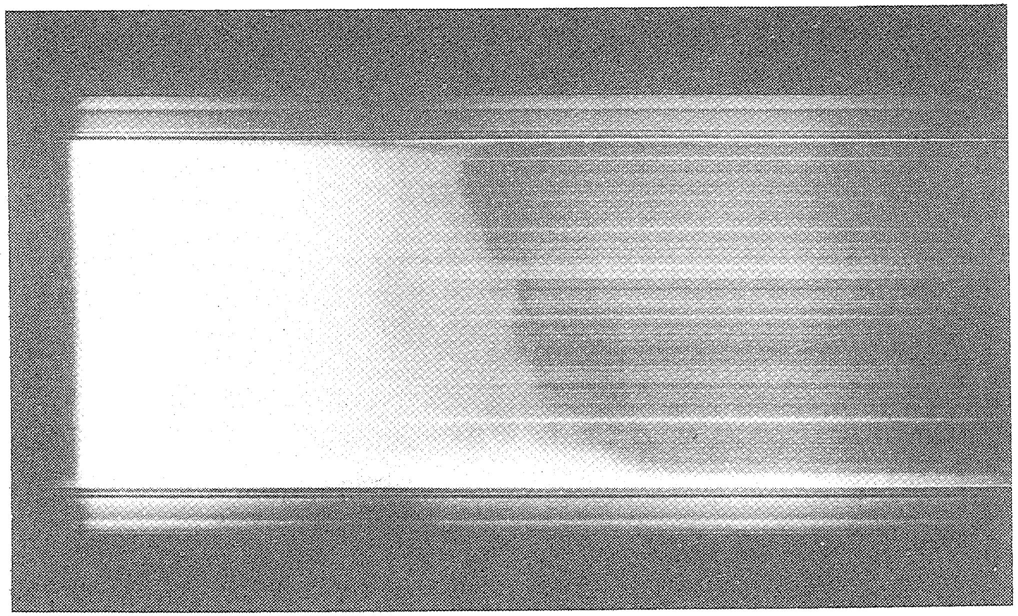

Figure 25. Vertical-slit photograph of shock wave in xenon.

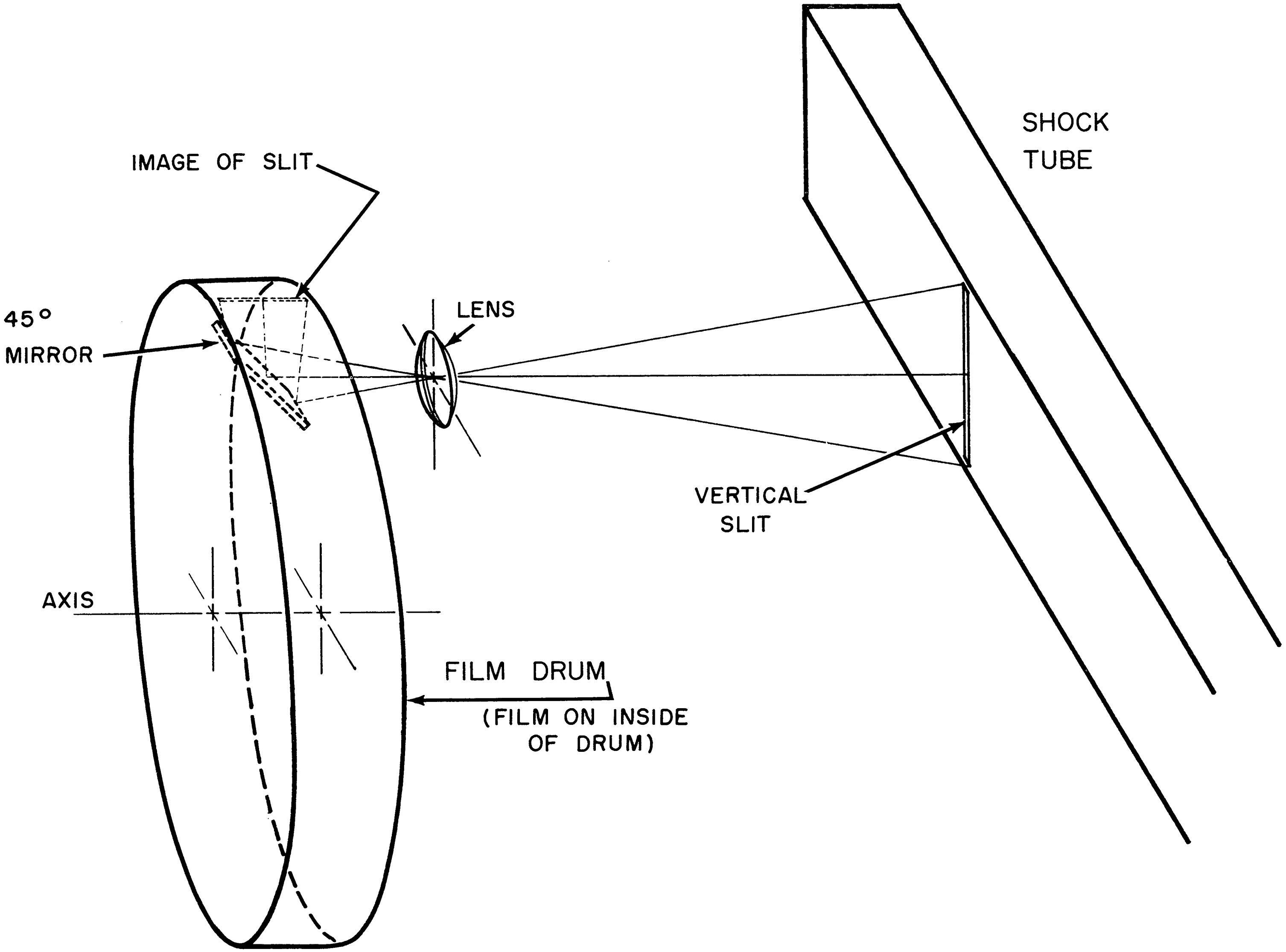

Figure 26. Schematic diagram of apparatus for vertical-slit photographs.

boundary is very uneven, showing that the interface is not the plane, thin boundary assumed ideally. This particular shot was made using two diaphragms in series with the heavier diaphragm downstream. It was found that the interface was less irregular when the thinner diaphragm was placed on the downstream side.

Another method of photographing the interface was to fire hydrogen into neon and make a wave-speed photograph in the light of H_β by using an interference filter in front of the lens of the wave-speed camera. It was found that the Balmer lines of hydrogen are strongly emitted at the border of the interface with the hot neon gas. According to the analysis which will be given in the next chapter, the maximum amount of luminosity occurs when the concentration of hydrogen in the neon is about 1-1/4%.

The wave-speed photograph made in this manner is shown in Figure 27. In order to help explain the photograph, the positions of the first and subsequent reflected shock waves have been drawn in with white ink. As in previous wave-speed pictures, the time axis is vertical and increases upward, and the end of the tube is at the right-hand side of the picture. The temperature is not sufficient to excite the emission of the hydrogen lines until after the first reflected shock. The maximum luminosity comes from that region of the interface where the concentration of hydrogen in neon is from 1/2 to 2%. It is of considerable importance in the work on hydrogen line broadening, which will be discussed in the next chapter, that the hydrogen does not diffuse through the interface into the region behind the first reflected shock. The luminosity is confined to filaments the shape of which indicates vorticity in the interface. There is also some diffuse luminosity from the highest temperature region at the right, but this is thought to be due to continuum radiation from neon ionized to 1 or

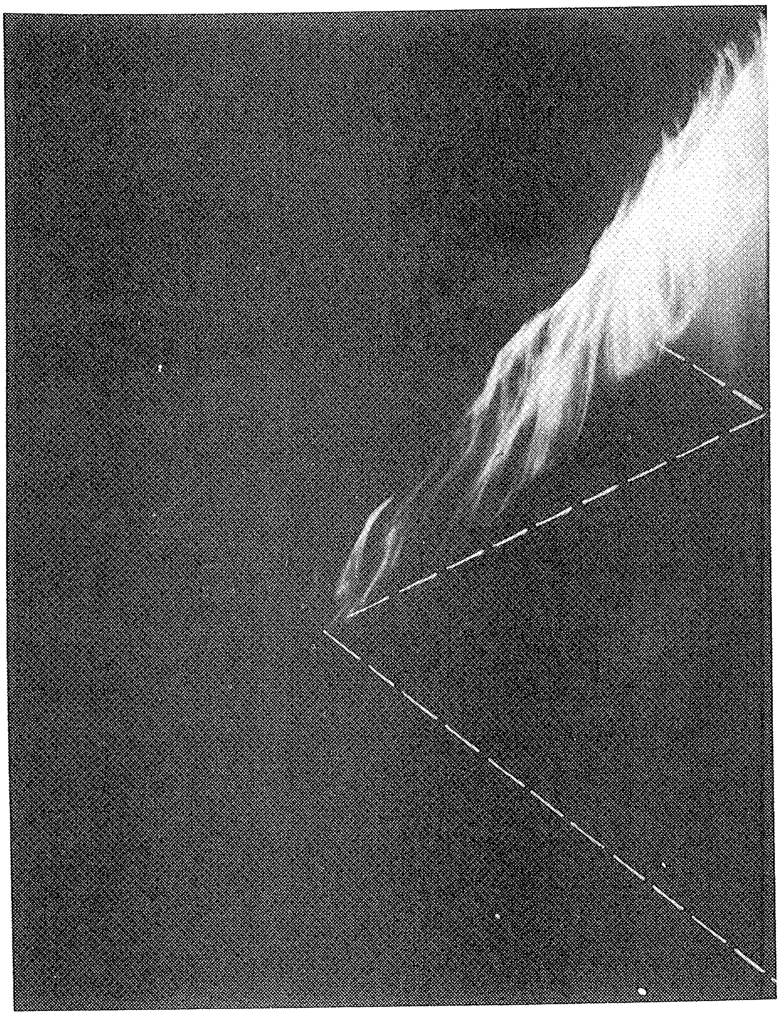

Figure 27. Hydrogen interface photographed in the light of the H_β line.

2%. The interference filter has a band-width of about 150 Å, so some of this continuum radiation will get through. The mixing of the hydrogen and neon in the interface therefore seems to be primarily due to turbulence and vorticity rather than diffusion.

CHAPTER V

SPECTRA AND LINE BROADENING

1. Qualitative Description of Visible Spectra

The luminous shock tube is a spectrographic light source especially suited to the study of phenomena involving interactions of atoms and ions. Except for a thin boundary layer, the temperature is homogeneous across a section of the tube, resulting in pure emission spectra without any self-reversal of the lines. Quantitative studies of the spectra are therefore greatly simplified in contrast to arcs and flames where cooler layers surround the hot core. By varying the initial pressures and the kind of gas used, almost any conditions of temperature, pressure, and ion density may be obtained within rather wide limits. Furthermore, these conditions may be calculated from the measured velocity of the primary shock wave.

A series of shock-tube spectra in argon at increasing shock strengths is shown in Figure 28. These spectra were obtained by observing the end of the shock tube through a Plexiglas window. Therefore, they are both a time and a space average of the luminosity. Because of this the spectra could not be used for quantitative measurements, but they do show qualitatively the effects of increasing shock strength. The estimated temperature and degree of ionization behind the first reflected shock wave is given for each spectrum. Subsequent shock waves moving through the luminous gas (see Figure 8, case A) will, of course, heat it somewhat, while energy losses by radiation will cool the gas.

First of all one sees the increase of the continuous radiation with

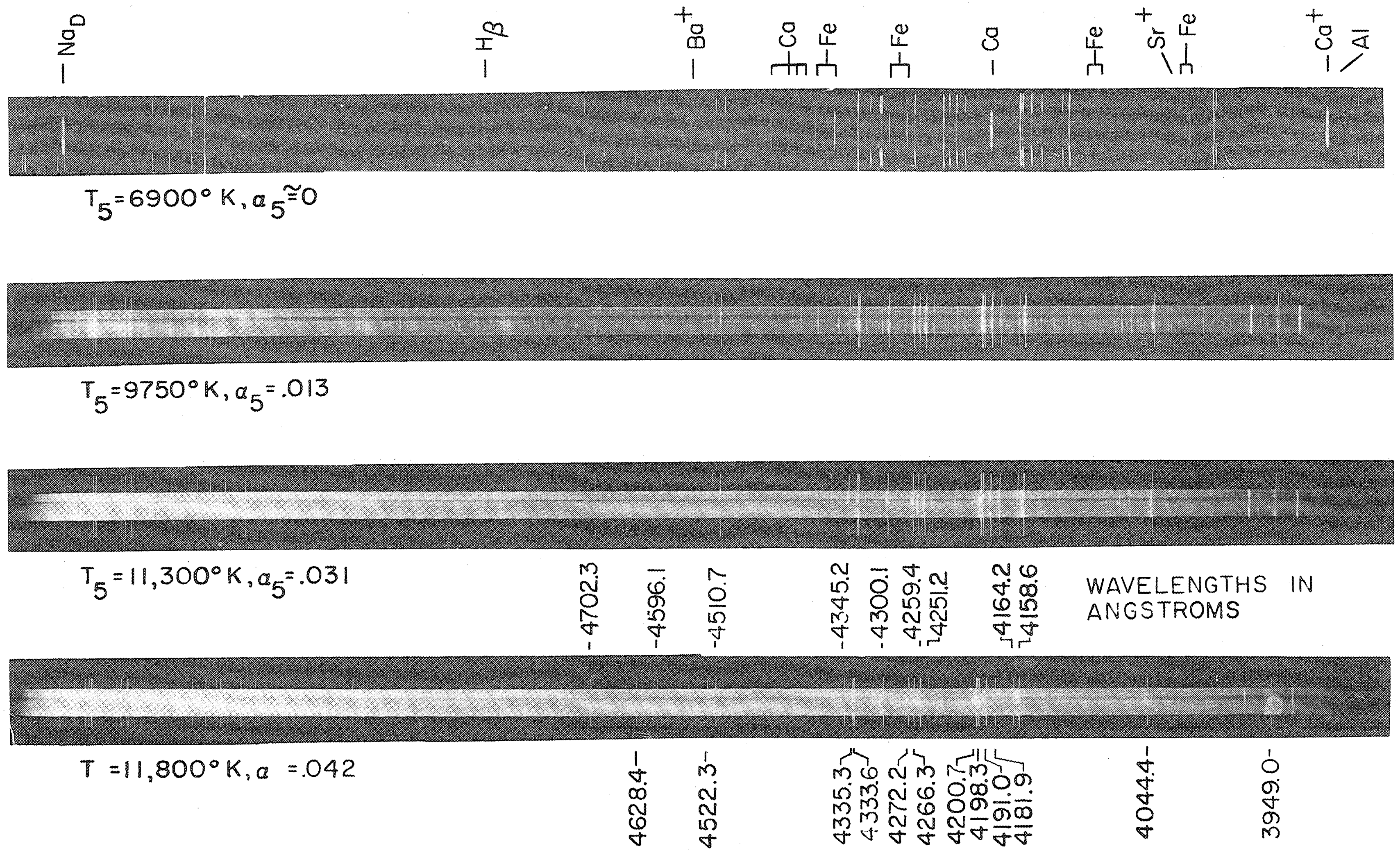

Figure 28. Series of spectra of shock-tube luminosity in argon.

increasing shock strength. This radiation arises primarily from the recombination of ions and electrons, although there is a small effect from Bremsstrahlen or free-free transitions. A free electron can have any energy within a continuous range, and the momentum distribution is given by the Maxwell-Boltzmann formula,

$$N_e(p)dp = A N_e p^2 e^{-\frac{E}{kT}} dp .$$

A is a constant, N_e is the number of electrons per cc, p is the momentum, and $E = p^2/2m$ is the energy of the electron. Transitions from this continuum to the discrete energy levels of the bound electron give rise to the continuous radiation whose frequency, ν, is given by

$$h\nu = E_{free} + (\chi - E_n) .$$

E_{free} is the energy of the free electron, χ is the ionization potential of the atom, and E_n is the energy of the n^{th} discrete level referred to the ground state of the atom. For the free-free transitions, $h\nu = E_{free} - E'_{free}$. A classical description of the free-free transitions is that the electron approaches the ion in one hyperbolic orbit, emits radiation, and leaves in another hyperbolic orbit of lower energy. For both of these sources of continuous radiation the intensity is proportional to $N_e \cdot N_{ions}$, or in our case where $N_e = N_{ions}$ the intensity is proportional to the square of the ion density.

The series of spectra in argon illustrates this very well. For the first one the ionization is negligible and the continuum is very weak. The intensity of the continuum increases with each spectrum until for the last one, where the degree of ionization is 4%, the continuum is so intense that the spectral lines can barely be seen. The continuum radiation is primarily responsible for the radiative energy loss. The line spectrum, although intense, contributes only a small fraction of the total radiated energy when summed over all wavelengths.

Metallic impurities which have rather low excitation energies show up very well in the spectra observed in the shock tube. Many lines of Na, Ca, Ba, Sr, Rb, Mg, Al, Ti, and Fe have been identified. The strongest of these are indicated on the spectra of Figure 28. At lower temperatures, i.e., 7000°K, both the neutral and ionized lines of Ca, Ba, Rb, and Sr are fairly strong, but as the temperature is increased to 10,000°K the neutral lines become weak and the ionized lines predominate, indicating that the metals have been mostly ionized. The strongest of all the metallic lines are the H and K lines of Ca II.* The alkaline earth metals, such as calcium, upon single ionization, have a spectrum similar to the alkali metals, and the H and K lines are the resonance radiation resulting from the transition $^2P_{1/2,3/2}$ to $^2S_{1/2}$. These metallic lines originate from minute amounts of dust and impurities on the surface of the tube. We have found, however, that the lines of some elements not ordinarily seen in the spectrum of the shock tube can be produced by the introduction of a small amount of a slightly volatile metallic compound. The lines of copper have been produced by putting a small amount of copper acetyl acetonate in the tube. Hydrogen lines are also seen in shots into the rare gases; they come from the mixing of hydrogen with the hot gas at the interface. It should be possible to observe the lines of almost any element that can be introduced as a gas, such as O, N, C, and S from N_2, O_2, CO, SO_2, etc. Indeed, we have already observed lines of oxygen introduced as an impurity into neon.

One of the most interesting features of the spectra shown in Figure 28

---

*The Ca II lines are the most prominent metallic absorption lines seen in the spectra of most stars.

is the broadening and red shift of the rare-gas lines. In the first spectrum, where the ionization was negligible, the argon lines, identified by the Geissler tube spectrum above and below the shock-tube spectrum, are fairly sharp. As the degree of ionization increases, the red shift, which is about equal to the half-width, increases until for the final spectrum of the series it is about 3 Å. Figure 29 shows a microdensitometer trace of several argon lines in the third shock-tube spectrum together with a trace of the Geissler tube lines. The argon lines appear to be symmetric with the maximum shifted toward the red.

The qualitative features of these broadened argon lines seem to be in accordance with the theories of Foley[35] and Lindholm,[36] which predict a shift in the line maximum as well as a broadening. These theories consider the effect of encounters with moving perturbers which cause changes in the phase of the radiation being emitted. They find that the ratio of the shift to the half-width does not change with the number of perturbers per cc. For an inverse power law interaction of the form $1/r^p$, Foley and Lindholm find that

$$\frac{\text{shift}}{\text{half-width}} = \frac{1}{2} \cot \left\{ \frac{p-3}{2(p-1)} \pi \right\} .$$

For the interaction of charged particles on the argon atoms, $p = 4$, so the ratio is $\sqrt{3}/2$. Since the electrons move much faster than the ions, they produce many more collisions with the radiating atoms and, hence, in the collision theory, contribute far more to the broadening of the lines. Lindholm and Foley obtain a line shape given by*

$$I(\nu) = I_0 \left(\frac{\gamma}{4\pi}\right)^2 \frac{1}{\left(\nu-\nu_0+\frac{\beta}{2\pi}\right)^2+\left(\frac{\gamma}{4\pi}\right)^2} .$$

---

*See page 248, Reference no. 27.

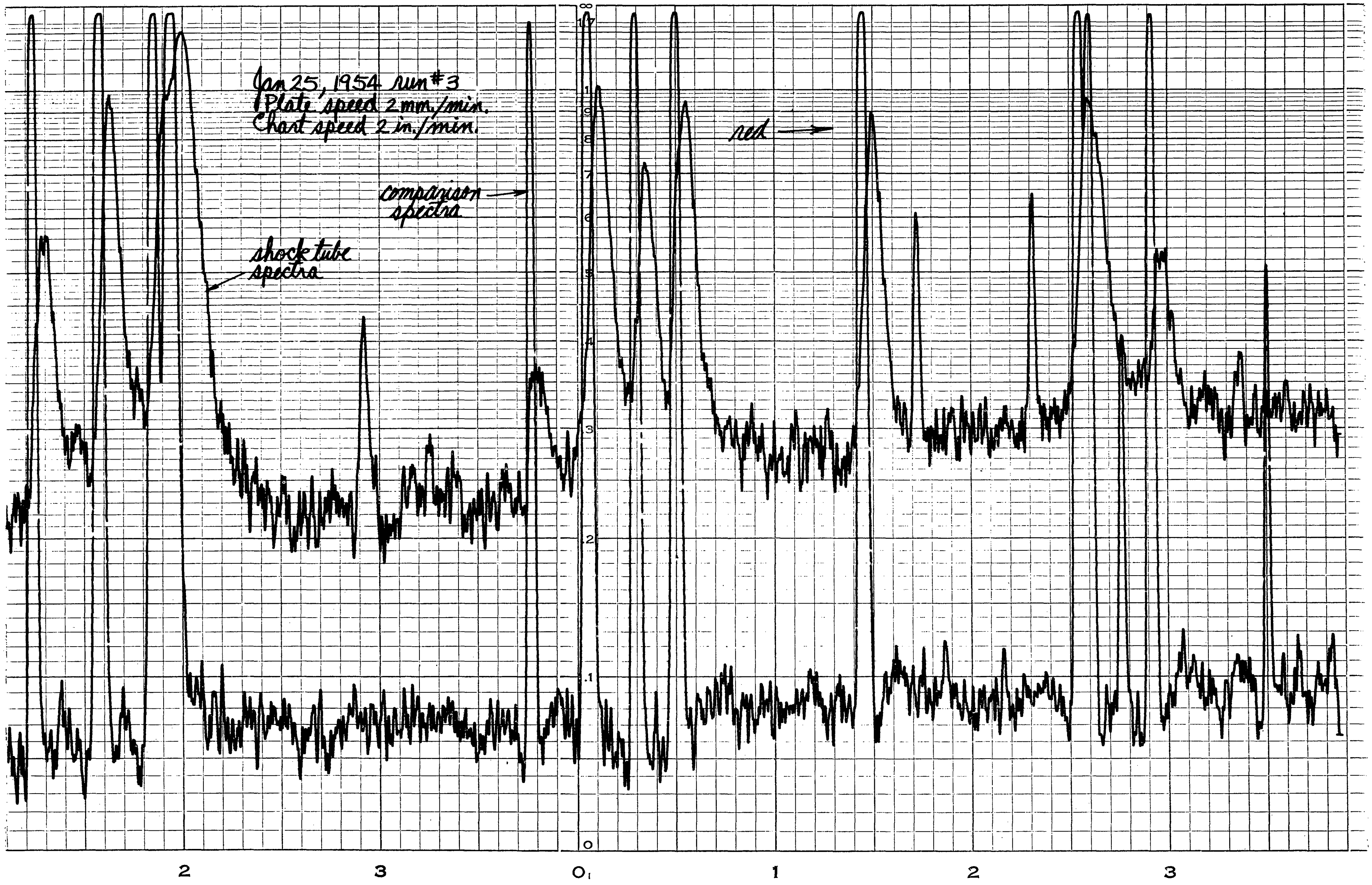

Figure 29. Microdensitometer trace of broadened argon lines.

The expression $\beta/2\pi$ is the shift of the line center and $\gamma/2\pi$ is the half-width; β and γ are proportional to the two-thirds power of the second-order Stark coefficient,* to the cube root of the mean relative speed between a radiating atom and a perturbing particle, and to the first power of the density of perturbing particles. Minnhagen[37] has measured the second-order Stark coefficients for argon, and, for the lines designated by wavelengths in Figure 28, the coefficients are all positive, i.e., the lines are shifted to the red. Earlier theories by Lorentz[38] and Weisskopf[39] for collision broadening gave a dispersion line shape but no shift.

The broadening of argon lines in shock-tube spectra was studied by Kantrowitz _et al._,[17] who compared their results to a theory developed by M. Baranger and H. A. Bethe.[40] They considered also the static field of the ions in addition to collisions with the fast-moving electrons and obtained line shifts about 20% less than Foley and Lindholm. Their experimental values for the line shifts were not quite accurate enough to differentiate between the two theories.

Spectra were also obtained of shots into xenon and krypton, and a couple of representative spectra are shown in Figure 30. Stronger shocks can be produced in the shock tube with these heavier rare gases (see Figure 5). This, combined with the lower ionization potentials, produces greater ion densities than for the argon shots, resulting in a strong continuum. The krypton lines are broadened and shifted to the red in the same manner as the argon lines, but it can be seen that some of the xenon lines are broadened asymmetrically to the red.

---

*Most radiating atoms in a homogeneous electric field produce spectral lines which are shifted by an amount proportional to the square of the electric-field strength. This factor of proportionality is called the second-order Stark coefficient.

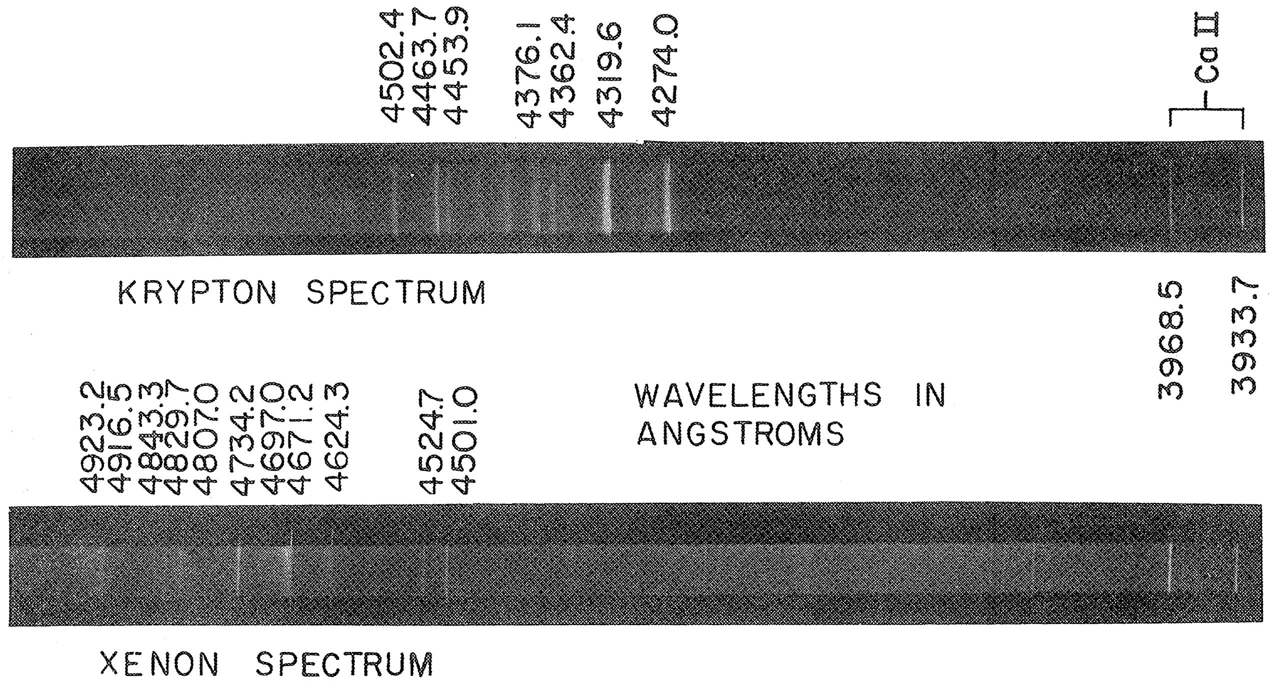

Figure 30. Spectra of shock-tube luminosity in krypton and xenon.

2. Near-Infrared Spectra

Many of the near-infrared lines of the rare gases are considerably more intense than the strongest visible lines. The reason is that they are successive series members. Simplified energy-level diagrams of argon and xenon are shown in Figure 31. The ground state of the ion is a $^2P_{3/2,1/2}$ configuration with an energy difference between the levels with different J values, which is small for argon but is considerable for xenon (see Figure 9 and Table II). The energy levels designated with primes approach the $^2P_{1/2}$ state of the ion as a limit while the unprimed levels approach the lower-lying $^2P_{3/2}$ state of the ion. Thus for argon the corresponding primed and unprimed levels are fairly close together, while for xenon they are far apart. The designations of the energy levels are consistent with those introduced by Charlotte Moore[41] for the jl-coupling scheme of the rare gases.

From these diagrams in Figure 31, it can be seen that the strong infra-

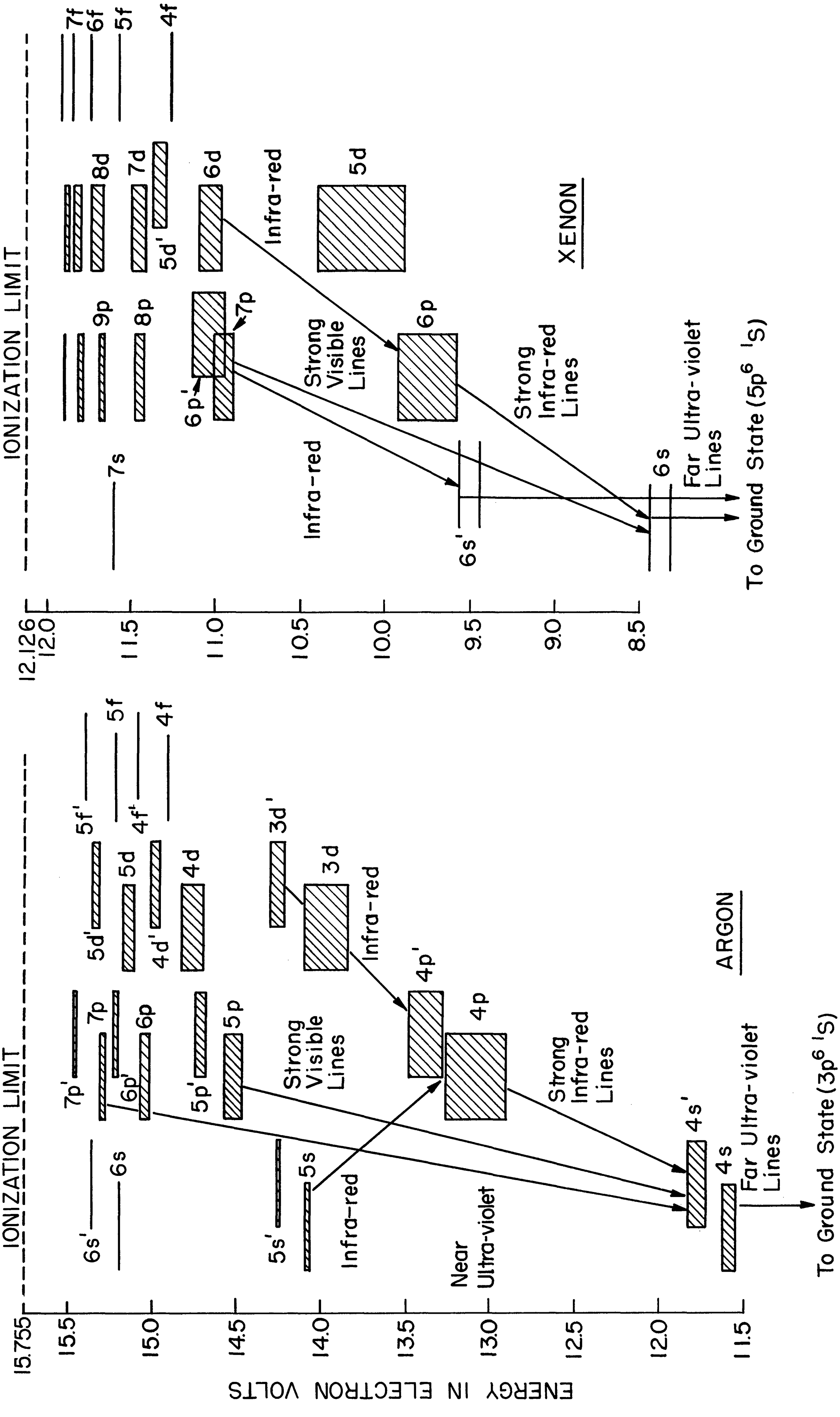

Figure 31. Simplified energy-level diagrams of argon and xenon.

red lines come from lower-lying p levels than do the visible lines. Even though the I-N photographic plates used for the near infrared are less sensitive than those used for the visible, the additional intensity of the infrared lines makes them appear stronger. With the new grating spectrograph it has been possible to photograph the near-infrared spectrum with a dispersion of 22.5 Å per mm—large enough to study the line broadening of the rare-gas lines in the shock tube. This was not possible with the two-prism instrument used previously.

Figure 32 shows three of the near-infrared spectra of argon and xenon. For both rare gases it appears that the red shift of the strongest lines is small compared to the half-widths. At first it was thought that the Lindholm-Foley theory did not apply to these lines because of this small ratio of shift to half-width, but rough calculations indicated that the strongest lines have a large self-absorption. This distorts the line shape by decreasing the intensity of the center by a large amount so that a line appears somewhat wider than it actually is. The only thing we can say, therefore, is that the second-order Stark coefficients for the strong infrared lines are less than for the visible lines as evidenced by the smaller red shift.

The weaker infrared lines in argon which arise from transitions from the 5s, 5s', 3d, and 3d' levels to the 4p and 4p' levels show a broadening and red shift comparable to the strong visible lines. Some of the weaker infrared lines of xenon resulting from transitions originating from the 6p' and 7p levels show a moderate broadening and are asymmetrically shifted to the red. This broadening is very similar to that observed for the visible lines of xenon (see Figure 30) which arise from transitions from the same upper levels. This asymmetry is not in agreement with the Lindholm-Foley

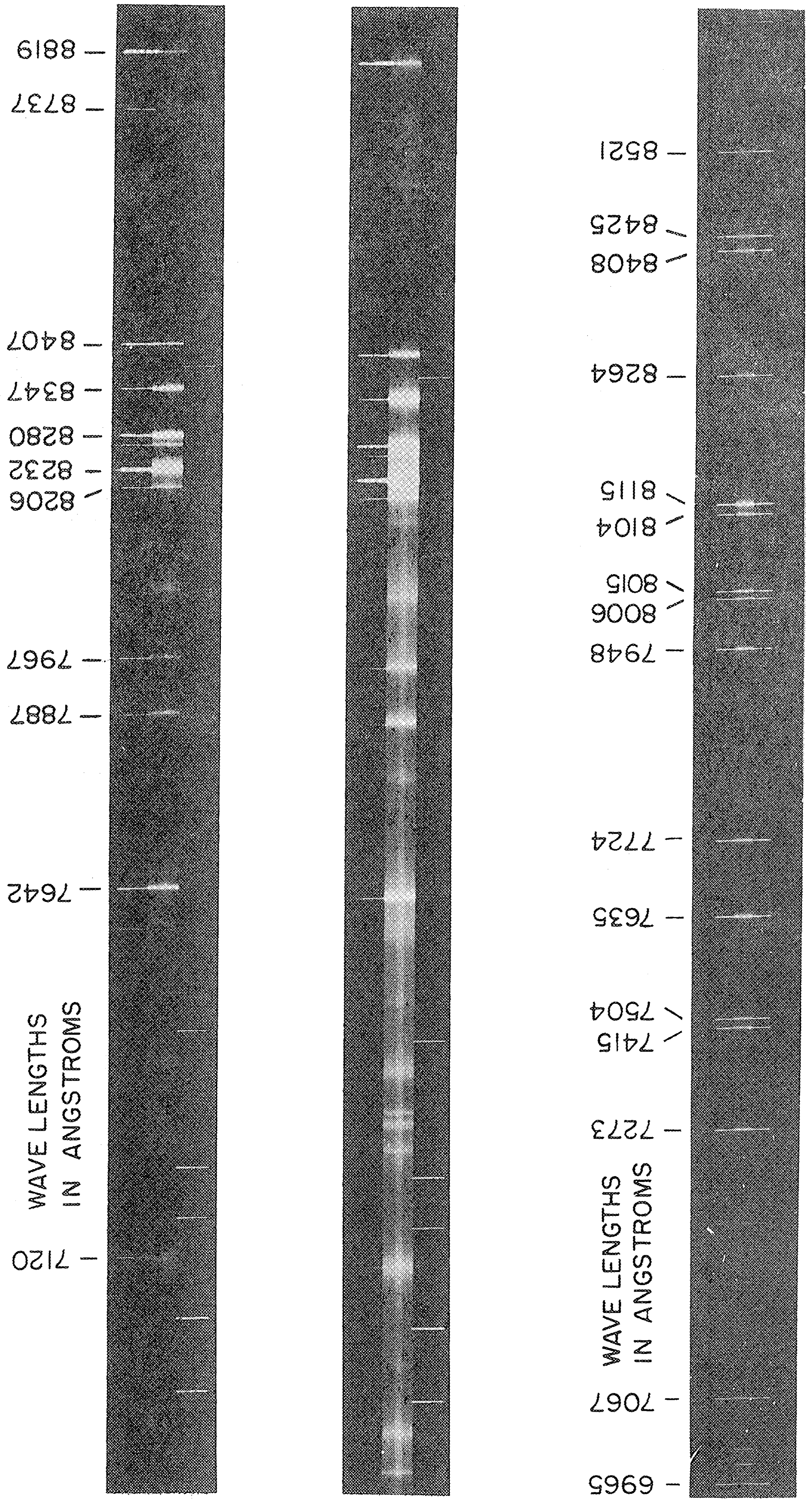

Figure 32. Near-infrared spectra of shock-tube luminosity in argon and xenon.

theory which predicts a dispersion line shape. Therefore, in addition to the broadening by collisions there must be another broadening mechanism which gives the asymmetry. One possibility might be the effect of the static-field distribution of the ions, which is asymmetric (see Section 4).

Also in the xenon spectrum one can see that some of the weakest lines, resulting from transitions originating from the higher levels, are extremely broad, comparable to the hydrogen line broadening (see Section 3). This suggests a first-order Stark effect which can occur where two or more levels, between which long wavelength transitions can occur, lie close together. Most of the shifts of the weaker lines are toward the red as expected, but a few like the 7120 Å line are symmetric in spite of the fact that the second-order Stark effect shifts most of the components towards the red.*
These phenomena have not been investigated further.

3. Spectrum of Hydrogen in Neon

It was discovered that the Balmer lines of hydrogen show up extremely well when hydrogen is fired into pure neon. This is due to the fact that the excitation energies of hydrogen are much lower than those of neon. The $n = 4$ level of hydrogen, for example, lies at 12.74 volts above the ground state, while the $3p[1/2]_1$ level of neon is at 18.37 volts. Therefore, if there is a mixture of the two gases at a high temperature, the hydrogen lines will be far stronger than the neon lines. Figure 33 shows a spectrum made with the two-prism spectrograph observing end-on. The spectrograph therefore sees both a time and a space average of the luminosity. In Figure 27 it was shown that the hydrogen luminosity comes from the hydrogen-neon interface. Also shown in Figure 33 is a microdensitometer trace of

---

*The Stark coefficients for many xenon lines have been measured by Harkness and Heard.[42]

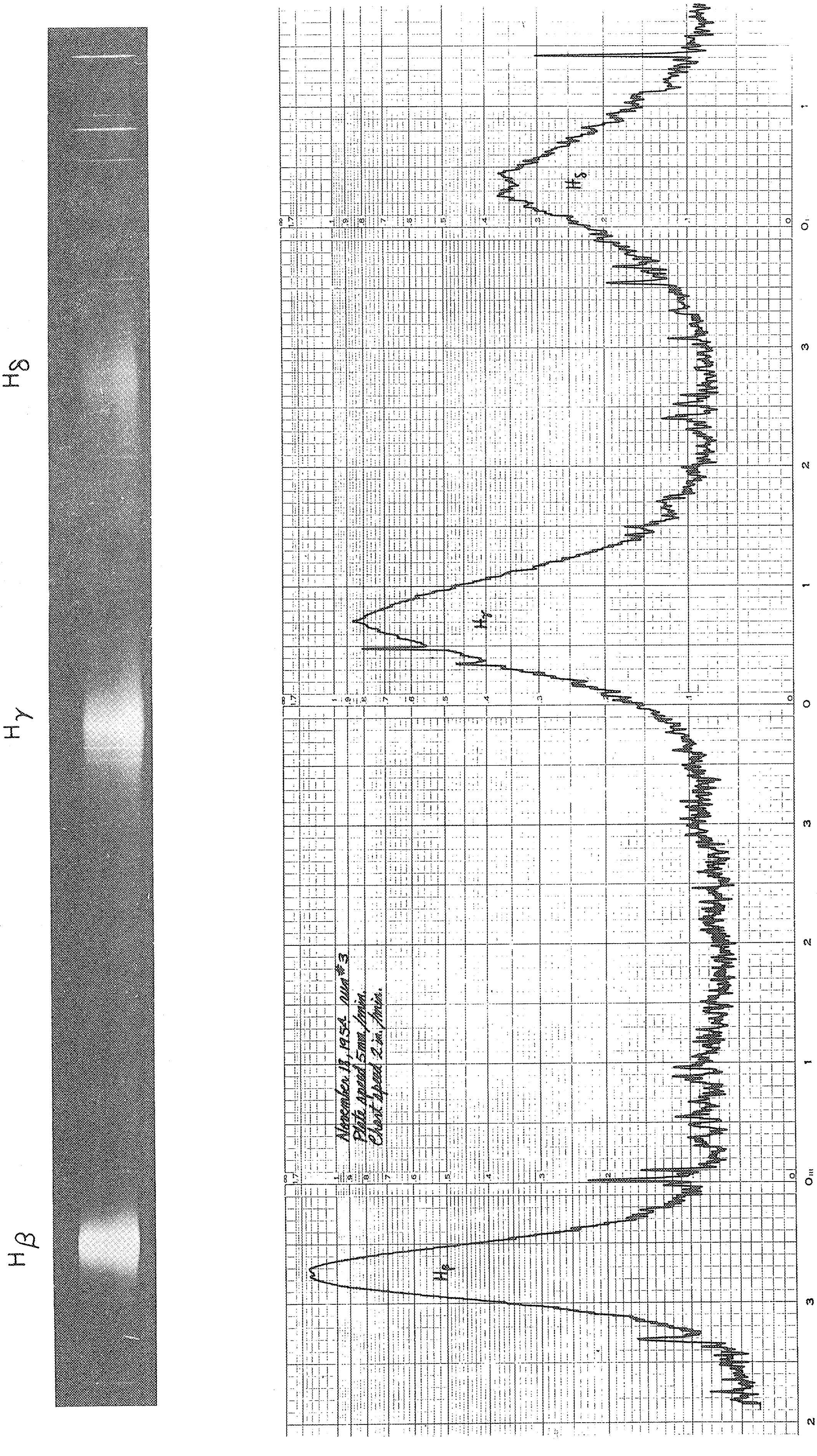

Figure 33. Spectrum of shock-tube luminosity in neon, using a hydrogen driver and microdensitometer trace of spectrum.

the spectrum. The Balmer lines are extremely wide, ~ 70 Å half-width,[*] showing the large susceptibility to broadening by the ions and electrons.

Since the hydrogen lines show up so strongly at the interface, it should be possible to observe them in the region behind the first reflected shock wave if a small amount of hydrogen were added to the neon. This idea was quite successful and the results will be discussed in Section 5. One problem that arises, however, is the estimate of the optimum fraction of hydrogen to give the greatest line intensity. For very small amounts of hydrogen the hydrodynamic variables will be changed very little and the hydrogen line intensity will be proportional to the concentration of hydrogen. For larger fractions of hydrogen, the temperature of the hot flow will be lowered due to the higher sound speed of the mixture of neon and hydrogen and because of the energy required to dissociate the hydrogen behind the primary shock wave. Thus, in spite of the higher concentration of hydrogen, the line intensity will be less because of the lower temperature. Therefore, there is a value of the fraction of hydrogen for which the hydrogen line intensity will be a maximum. This maximum will also change slightly for each different initial pressure ratio, Z. The details of the calculation of the intensity of H_β for different fractions of hydrogen are given in Appendix D. The results are shown in Figure 34, and it appears that about 1.2% of hydrogen gives the maximum H_β intensity for the average initial pressure ratio used.

4. First-Order Stark Broadening of Hydrogen

Before going to the observations of hydrogen line broadening, it is advisable to review briefly the mechanism involved. In 1913 Stark[43] demon-

---

[*] The average electric-field strength required to produce this amount of broadening is more than 200,000 volts per cm.

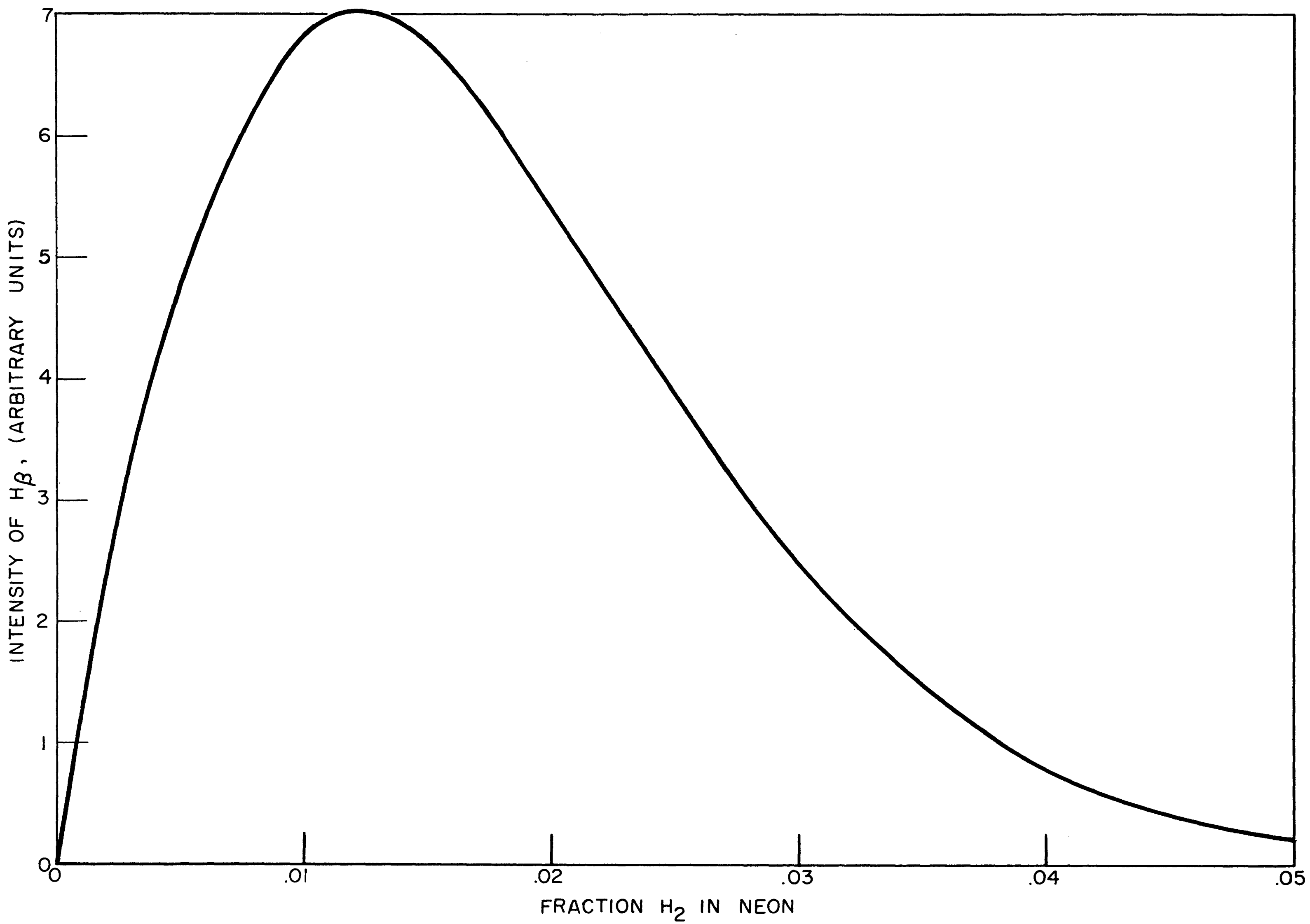

Figure 34. Intensity of H_β vs fraction of hydrogen added to neon.

strated that the Balmer lines of hydrogen are split into a number of components when excited in a strong electric field of around 100 kilovolts per cm. When viewed perpendicular to the field, some components are observed to be plane polarized parallel to the electric field (π - components) and others polarized perpendicular to the field (σ - components). One of the successes of the old Bohr quantum theory was the theoretical explanation of this phenomenon by Epstein[44] and Schwarzschild.[45] The results were little changed with the Schrödinger and Dirac theories. The intensities of the components were calculated by Schrödinger[46] and found to be in good agreement with the measured intensities of Stark. In Figure 35 the displacements and relative intensities calculated by Schrödinger for the Balmer lines H_α, H_β, H_γ, and H_δ are shown. The components are symmetric about λ_0, and the displacement, $\Delta\lambda_i$, of a component is proportional to the field strength ($\Delta\lambda_i = C_iF$, where F is the electric-field strength). For the lines H_β and H_δ all

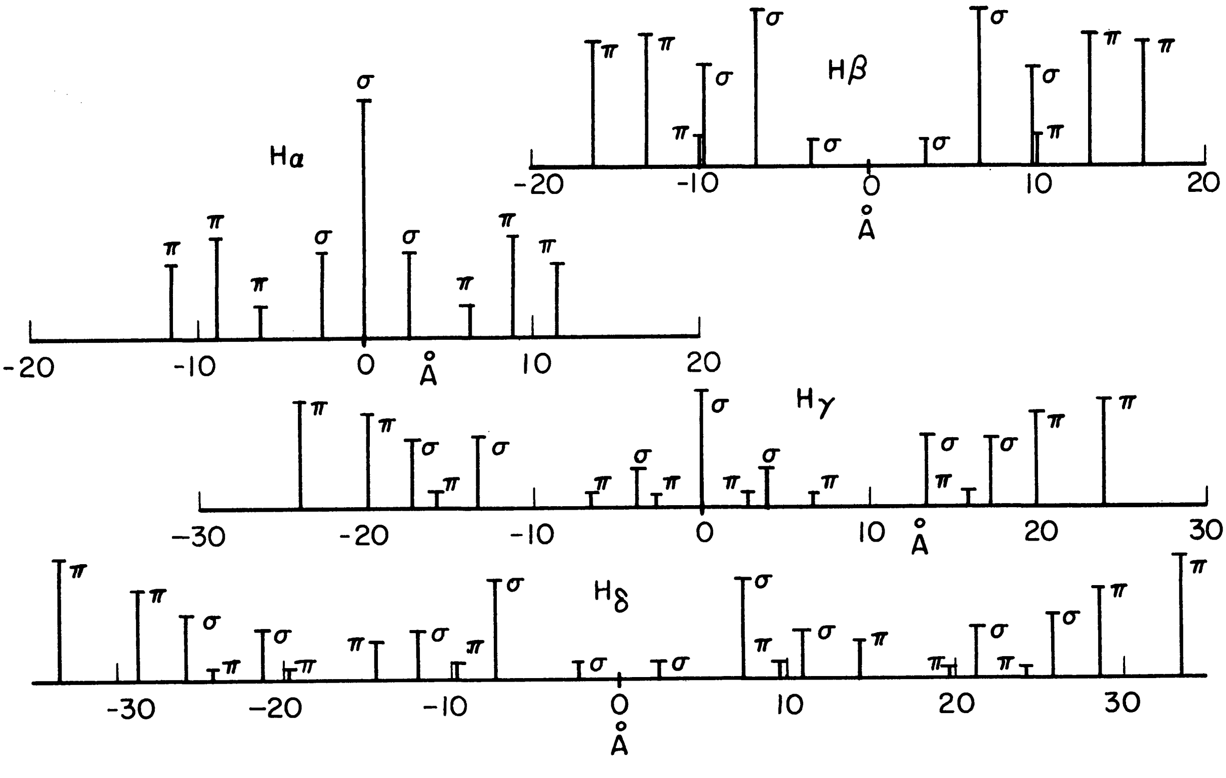

Figure 35. Stark components of H_α, H_β, H_γ, and H_δ.

components are displaced from the center, while H_α and H_γ have components which, to first order, are not shifted by the electric field.

In an ionic plasma the electric field at any point changes rapidly in direction and intensity, so one must consider the probability distribution of the field rather than a given electric-field strength. Each of the Stark components will be smeared out by this distribution, and the sum of the contributions from all the Stark components, properly normalized, will give the line-intensity profile. Holtsmark[47] derived such a field probability distribution for a static distribution of ions, i.e., neglecting the effect of the motion of the ions or electrons. Holtsmark introduces the "normal field strength," F_0, which is given by*

$$F_0 = 2.61 e N^{2/3},$$

where e is the charge of the electron and N is the number of ions per cc. The probability distribution of the electric field is then given as $W(\beta)$, where $\beta = F/F_0$, and is shown in Figure 36. $W(\beta)$ is independent of the ion density, so the shape of a hydrogen line does not change with ion density according to the Holtsmark theory. Schmaljohann,[48] using the Holtsmark distribution, calculated the line-intensity profiles for H_α, H_β, H_γ, and H_δ.** These profiles are given by the function $S(\alpha)$, where $\alpha = \Delta\lambda/F_0$, with $\Delta\lambda$ given in Angstrom units. $S(\alpha)$ for the first four Balmer lines is also shown in Figure 35. $S(\alpha)$ is normalized so that

---

*If the electronic charge is given in electrostatic units, the field strength will be in statvolts, which must be multiplied by 300 to obtain the field strength in volts.

**Pannekoek and Verwey[49,50] also calculated the line profiles according to the Holtsmark theory, but, as pointed out by Schmaljohann, they did not multiply the σ components by 2. Jürgens corrected a numerical error in Schmaljohann's profile of H_β. DeJager[51] has also calculated the Balmer line profiles correctly from the Holtsmark theory.

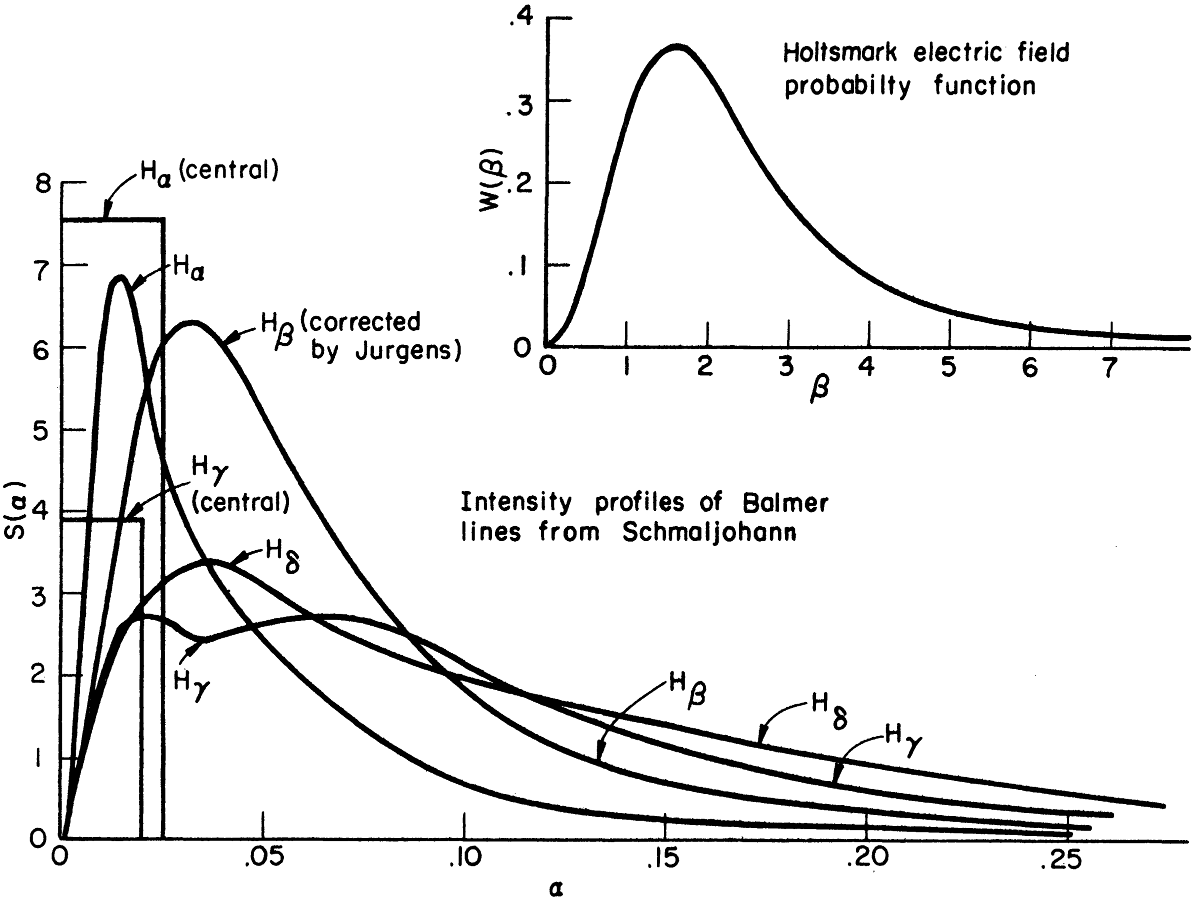

Figure 36. The Holtsmark distribution, $W(\beta)$, and the Schmaljohann $S(\alpha)$ for the hydrogen lines H_α, H_β, H_γ, and H_δ.

$$\int_{-\infty}^{\infty} S(\alpha)\,d\alpha = 1.$$

The Holtsmark theory does not predict any broadening for the central components of H_α and H_γ, so to normalize these lines to unity a rectangular area corresponding to the intensity of these components is shown on the graph. The normalization of $S(\alpha)$ is then understood to include also this area for H_α and H_γ. These central components cause the maximum of the intensity distribution to be at the center for H_α and H_γ, while it appears that the intensities of H_β and H_δ should be zero at the center of the line. Doppler broadening and the quadratic Stark effect fill in the center somewhat, but a very distinct dimple appears for both H_β and H_δ (see Figure 32).

5. Time-Resolved Spectra of Hydrogen

In Section 3 the possibility of observing the Balmer lines of hydrogen in the region behind the first reflected shock by adding a small amount of hydrogen to neon in the low-pressure chamber was discussed. By measuring the velocity of the primary shock wave it is possible to calculate the conditions such as temperature, pressure, and ion density behind the first reflected shock with good accuracy. This will be discussed further in Section 7. Therefore, one has the possibility of observing the broadening of hydrogen lines formed under known conditions and comparing the results with current theories.

In order to observe the true line profiles formed in the region behind the first reflected shock, it is necessary to resolve the luminosity both in space and time. The space resolution is easily accomplished by observing with the spectrograph into the side of the test section and focusing on a region a known distance from the end of the tube. Time resolution is necessary to distinguish the region behind the first reflected shock from subsequent times when the shock reflected from the interface passes through the luminous region and heats the gas further. This is done by focusing the spectrum on film inside a rapidly rotating drum.

For the initial research on the broadening of hydrogen lines, the two-prism glass spectrograph was used together with the revolving drum camera as shown schematically in Figure 16. H_β was chosen for study because it was of sufficient intensity and the dispersion of the spectrograph (~ 25 Å/mm) was fairly good at this wavelength. The dispersion at H_α was too small and the intensity of H_γ was not enough to obtain a good profile. Another advantage was that H_β, because it has no undisplaced Stark components, can be compared completely with the Holtsmark theory.

It is very interesting to compare a time-resolved spectrum of H_β with wave-speed photographs made under the same conditions. In Figure 37 we have on the left a wave-speed photograph made on panchromatic film (Eastman 103-D), using all wavelengths of visible light. The primary shock wave, the reflected shock wave, and streaks from dust particles are all clearly visible. The second wave-speed photograph was made while using an interference filter which transmitted a 130-Å band width centered at H_β. The luminosity due to impurities therefore cannot be seen, so the primary and reflected shock fronts are no longer visible. The luminosity that was recorded on the film came almost entirely from H_β emission. Here one can see, even more clearly than on the first wave-speed picture, the increase in luminosity resulting from the second and third reflected shock waves. The time-resolved spectrum of H_β shown at the right was enlarged to the same time scale as the wave-speed pictures. Equilibrium is reached after about 20 microseconds behind the reflected shock wave and the width of H_β appears fairly constant from that time until the arrival of the shock wave reflected from the interface, which then reflects off the end of the tube. This shock wave passing through the gas increases the temperature and ion density, resulting in an increase in the intensity and width of H_β. Finally the luminosity is quenched by the turbulent hydrogen-neon interface. For all three shots, $p_1 = 0.77$ mm Hg neon + 45μ H_2 and p_4 was from 925 psia to 940 psia of hydrogen. In the region behind the first reflected shock the half-width of H_β was 12.5 Å, and this was approximately tripled in the hotter region.

In order to get sufficient intensity, the spectrograph slit was 100μ wide and 2 mm long. This corresponds to a time resolution of about 20 microseconds. The wide slit resulted in a partial filling in of the cen-

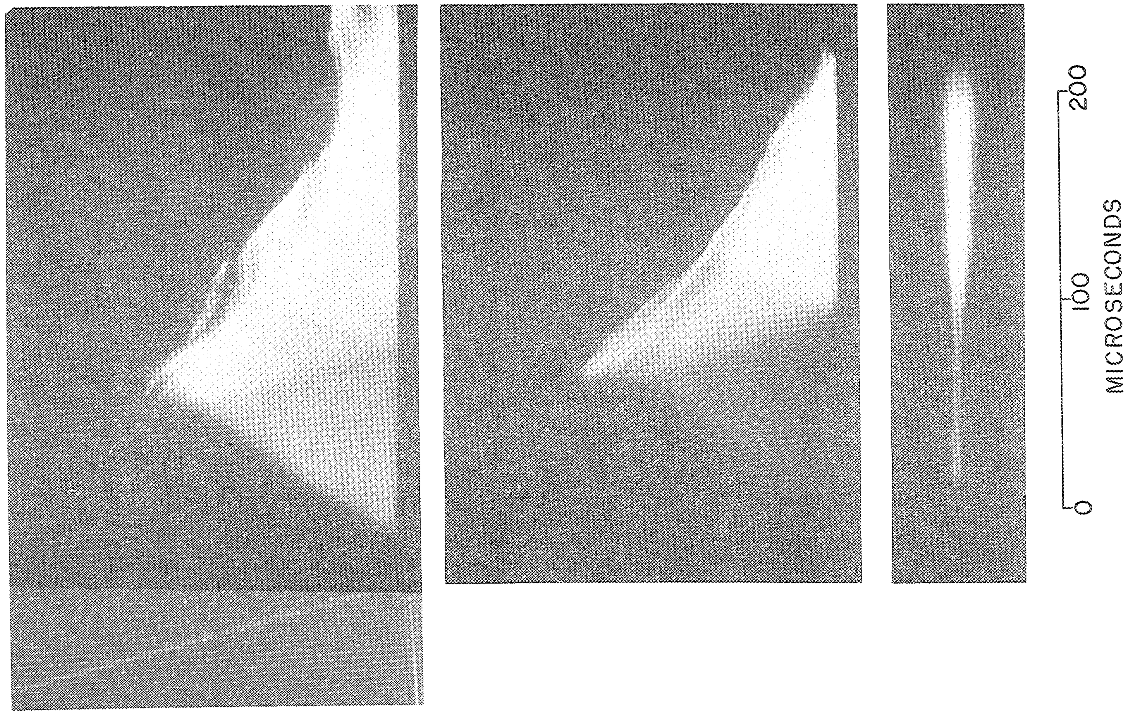

Figure 37. Time-resolved spectrum of H_β with corresponding wave-speed photographs. The left-hand wave-speed photograph was exposed with white light and the center with only the light of H_β.

tral hole in H_β. It is possible, however, to correct the line shape for the slit width, even though it is an appreciable fraction of the line width, by using a histogram method explained in Section 7.

Several time-resolved spectra of H_β were obtained by firing a hydrogen-oxygen explosive mixture into neon plus hydrogen. Half-widths of about 50 Å were obtained for H_β behind the first reflected shock. Lack of reproducibility in the shock velocities from one shot to the next made it impossible to calculate the ion densities accurately, so the data were not used.

For the most recent work the grating spectrograph with a revolving drum camera, shown in Figure 16, has been used. It appears to be just as fast as the two-prism instrument, and any wavelength, e.g., H_α, can be observed with a dispersion of approximately 22.5 Å/mm, using the 300-line/mm grating, and 5.3 Å/mm, using the 1200-line/mm grating.

In order to observe the true profile of a spectral line, even from a homogeneous layer, it is necessary that the luminous gas be optically thin, i.e., that the self-absorption is negligible. The intensity profile of a line emitted from a homogeneous layer of thickness* ℓ is given by

$$I(\nu) = B(\nu,T)[1 - \exp(-\kappa(\nu)\ell)] .$$

$B(\nu,T)$ is the Planck function and $\kappa(\nu)$ is the absorption coefficient. The term $\kappa(\nu)\ell$ is often called the optical depth or thickness, which is a dimensionless quantity. Expanding the exponential term we have

$$I(\nu) = B(\nu,T)\left[\kappa(\nu)\ell - \frac{(\kappa(\nu)\ell)^2}{2!} + \frac{(\kappa(\nu)\ell)^3}{3!} - + \dots\right] .$$

If $\kappa(\nu)\ell \ll 1$ then $I(\nu) = B(\nu,T)\kappa(\nu)\ell$ and the luminous gas is termed optically thin. As $\kappa(\nu)\ell$ becomes larger, the second- and higher-order terms become important. If the core of the line is optically thick and the wings

---

*For side-on observations with the shock tube, $\ell = 4.13$ cm.

optically thin, one obviously will not observe the true line profile.

In order to make an estimate of the optical depth, two simplifying assumptions will be made. First we assume a dispersion line shape so that the well-known equation, given by Aller,* for the absorption coefficient can be used:

$$K(\nu) = \frac{\pi e^2}{mc} Nf \frac{1}{4\pi^2(\nu-\nu_0)^2+\left(\frac{\Gamma}{2}\right)^2} .$$

This gives a peak intensity slightly greater than that of the Holtsmark profile for H_β. The half-width $\Delta\nu_{1/2}$ is $\Gamma/2\pi$. N is the number of atoms per cc that are capable of absorbing a given spectral line and f is called the oscillator strength.** For $H\alpha$, f = 0.6408, and for H_β, f = 0.1193. If N_0 is the number of hydrogen atoms per cc, then for the Balmer lines

$$N = N_0 \cdot 2^2 \cdot e^{-\frac{E_2}{kT}},$$

where E_2 is the energy of the n = 2 level.

The second assumption will be that the half-width is given by the Holtsmark theory*** so that

$$\Delta\nu_{\frac{1}{2}} = CN_i^{2/3} .$$

The constant C is found from the Schmaljohann curves reproduced in Figure 35.

---

*Reference 27, p. 128.

**The f-values, although orginally derived from the old classical concept of harmonic oscillators, are still very convenient to use. The f-values are related to the Einstein transition probabilities by

$$A_{nn'} = \frac{g_{n'}}{g_n} \frac{8\pi^2 e^2 \nu^2}{mc^3} f_{n'n} .$$

***Actually it has been found that the half-width is slightly larger than given by the Holtsmark theory (see Section 8), so the optical depth calculated will be too large.

The following typical set of conditions was chosen for purposes of calculation:

$$1.35\%\ H_2, \quad y_{21} = 67.9, \quad T_5 = 11{,}300°K \quad .$$

$$N_i = 1.35 \times 10^{16}\ \text{ions/cc}, \quad N_o = 5.93 \times 10^{16}\ \text{H atoms/cc} \quad .$$

This corresponds closely to the maximum of the curve shown in Figure 34. For H_β the optical thickness at the center was only 0.019, so the line is less than 1% self-absorbed. Therefore, the shape of H_β is changed very little by self-absorption. For H_α, however, the optical thickness at the peak is estimated to be 0.5. Thus, under the conditions assumed above, the peak of H_α will be considerably lowered by self-absorption. Doherty[52] has devised a method for correcting the line shape for self-absorption if the optical thickness at the line peak is not too great. Thus, it is still possible to obtain the true line shape of H_α, for example, even though it is somewhat self-absorbed.

6. Photometric Methods

In order to obtain an accurate intensity profile from the image of a spectral line on a photographic film, it is necessary that the film be properly calibrated. This work is concerned only with relative intensities at a given wavelength, so it was not necessary to know the absolute intensity or the variation of intensity with wavelength of the calibrating lamp. Although the calibration of the time-resolved spectra was found to be somewhat difficult and filled with many subtle pitfalls, the writer believes that finally a system of calibration has been evolved which is quite adequate.

The first method for calibration was to focus the filament of a tungsten-strip lamp on the spectrograph slit and obtain a range of intensities by the use of different shutter speeds. This, of course, suffered from reciprocity law failure. The calibration film was always developed together with the film containing the time-resolved spectra in a tank which was agitated frequently. Usually the films were developed from 5-6 minutes in Eastman formula D-19 developer. Eastman spectroscopic film type 103-D was used for H_β and 103-F film was used for H_α.

The second method consisted also of focusing the tungsten-strip filament on the spectrograph slit. The shutter, however, was always used at the same speed of 1/100 second and the light was weakened by a filter which was a strip of 35-mm film with steps of increasing density placed in front of the slit. The transmission of each of these steps was measured with a Leeds and Northrup, Vincent-Sawyer type microdensitometer. A special setup was used so that only the specular transmission of the filter was measured.

This method seemed adequate, but in order to check whether the characteristic curve of the film was the same for an exposure of 1/100 sec as for a few microseconds, the following experiment was performed. A 7-step filter* of rhodium evaporated on crystal quartz was placed in front of the slit of the grating spectrograph and a 103-D plate was exposed for 1/100 sec with the strip-filament tungsten-lamp source and for two microseconds with a spark source. Curves of the Seidel function,[53] $S = \log_{10} (1/T - 1)$, were plotted vs the density of the step filter for each exposure time. T is the transmission of the film. These characteristic curves can be represented very well by the expression

$$S = a + \gamma \log_{10} I$$

---

*Purchased from the Jarrell-Ash Co., Newtonville, Mass. Each step was 1.2 mm long and the density steps were approximately 0.2. The density range was from 0(clear quartz) to 1.2.

from S = -0.5 to 1.5. For the 1/100-sec exposure the slope of the curve was 1.70, and for the two-microsecond exposure the slope was 1.33. If the 1/100-sec exposure is designated by the subscript 1 and the two-microsecond exposure by 2, then

$$S_1 = a_1 + \gamma_1 \log I_1$$
$$S_2 = a_2 + \gamma_2 \log I_2 ,$$

where $\gamma_1 = 1.70$ and $\gamma_2 = 1.33$. For an equal blackening of the film,

$$I_2 = I_1^{\gamma_1/\gamma_2} \times \text{constant} .$$

It was assumed that γ varies linearly with log t; $\gamma_1/\gamma_2 = 1.275$ so $\gamma_1/\gamma_3 = 1.20$ where the subscript 3 denotes a 20-microsecond exposure, the effective exposure of a time-resolved spectrum. Therefore the line profile intensities obtained by using the 1/100-sec-exposure calibration were taken to the 1.2 power to obtain the corrected intensity profile.

Also, using the 7-step filter of rhodium on quartz as a standard, it was found that the step filter on the 35-mm film was not neutral (i.e., did not have the same density at all wavelengths), but that the density steps at 4861 Å (H_β) were larger than those measured with the microdensitometer while using white light. The ratios of the density steps measured by the two methods was approximately 1.1, so the spectral line intensities had to be taken to the 1.1 power. The originally measured line intensity profiles were therefore taken to the 1.3 power. This included both the correction to the γ of the characteristic curve for the 20-microsecond exposure time and to the transmission of the step filter on the 35-mm film.

The necessity for all these corrections can be eliminated if the film is calibrated at approximately the same exposure time as that for the time-resolved spectrum, and if the step filter is neutral or the density steps known for each wavelength used. The latter requirement was easily met by using a 7-step rhodium-on-quartz filter, the transmission of which changes very little with wavelength. The first requirement was met by using a xenon flash lamp with the correct voltage and capacity to give an effective exposure time of approximately 20 microseconds.

When using the 7-step filter in front of the slit to calibrate the film, it is very important that the slit be evenly illuminated along its length. The best test is to make an exposure with the filter removed and then to make a microdensitometer trace across the exposed area to see if it is of constant density. The spectrum of the lamp consists of lines and a moderate continuum. A wide slit was used to obtain enough light and to make the lines very wide. A microdensitometer trace across the continuum gives the lower part of the characteristic curve for the film, while a trace across a denser line gives the upper part. Thus, although the range of densities of the filter is only 1.2, a characteristic curve can be obtained for a range of densities of more than 2.0.

The lamp was a war-surplus X-400 flash lamp used with identification equipment for aircraft. It was masked with black tape, except for a 24-mm length. The diameter of the glass tubing was about 5 mm. It was designed to be flashed at 2000 volts with a 50-microfarad capacitor, but only 4 microfarads were used to reduce the flash time to 20 microseconds. Two arrangements were found to give even illumination of the slit. The first is to place the lamp directly in front of the slit. The mask in front of the spherical mirror in the spectrograph is the same size as the grating, so it is necessary to mask off at least 0.5 cm (1/2 the slit height) from the top and bottom of the grating to avoid vignetting at the top and bottom. The other setup is to place the lamp horizontal, about 1/2 meter from the slit. The length of the lamp is sufficient to fill the grating from side to side, but the grating is not quite filled with light at the top and bottom, thus avoiding vignetting. The adjustments have to be made with the quartz window, on which the rhodium steps were evaporated, in place because the quartz window was purposely made with a slight wedge angle to avoid interference fringes. This wedge angle refracted the light downward almost one inch at the grating.

7. Calculations and Results

The work on the hydrogen line broadening consists of two groups of experiments. For the first group, only one revolving drum camera was available, so the wave-speed pictures and the time-resolved spectra were made separately. For the second group of experiments, two revolving drum cameras were utilized—one on the spectrograph for time-resolved spectra and the other for wave-speed pictures. The first group of experiments will be described first.

It is difficult to burst the diaphragm at any preselected pressure, so it was first necessary to determine how the shock velocity varied with the pressure, p_4, of hydrogen. Then for a time-resolved spectrum made when the diaphragm burst at some pressure, p_4, the corresponding shock velocity could be estimated. A series of wave-speed pictures were made at pressures of from 800 psia to 940 psia of hydrogen and the shock velocities were measured as described in Section 2, Chapter IV. For all shots the initial pressure in the low-pressure chamber was 0.769 mm Hg total (neon + 45μ hydrogen) and the diaphragm thickness was the same for all shots. The results are shown in Figure 38. A straight line, which appeared to be the best fit, was drawn through the experimental points. This gave the most probable value of the shock velocity for any given pressure, and the scatter of the

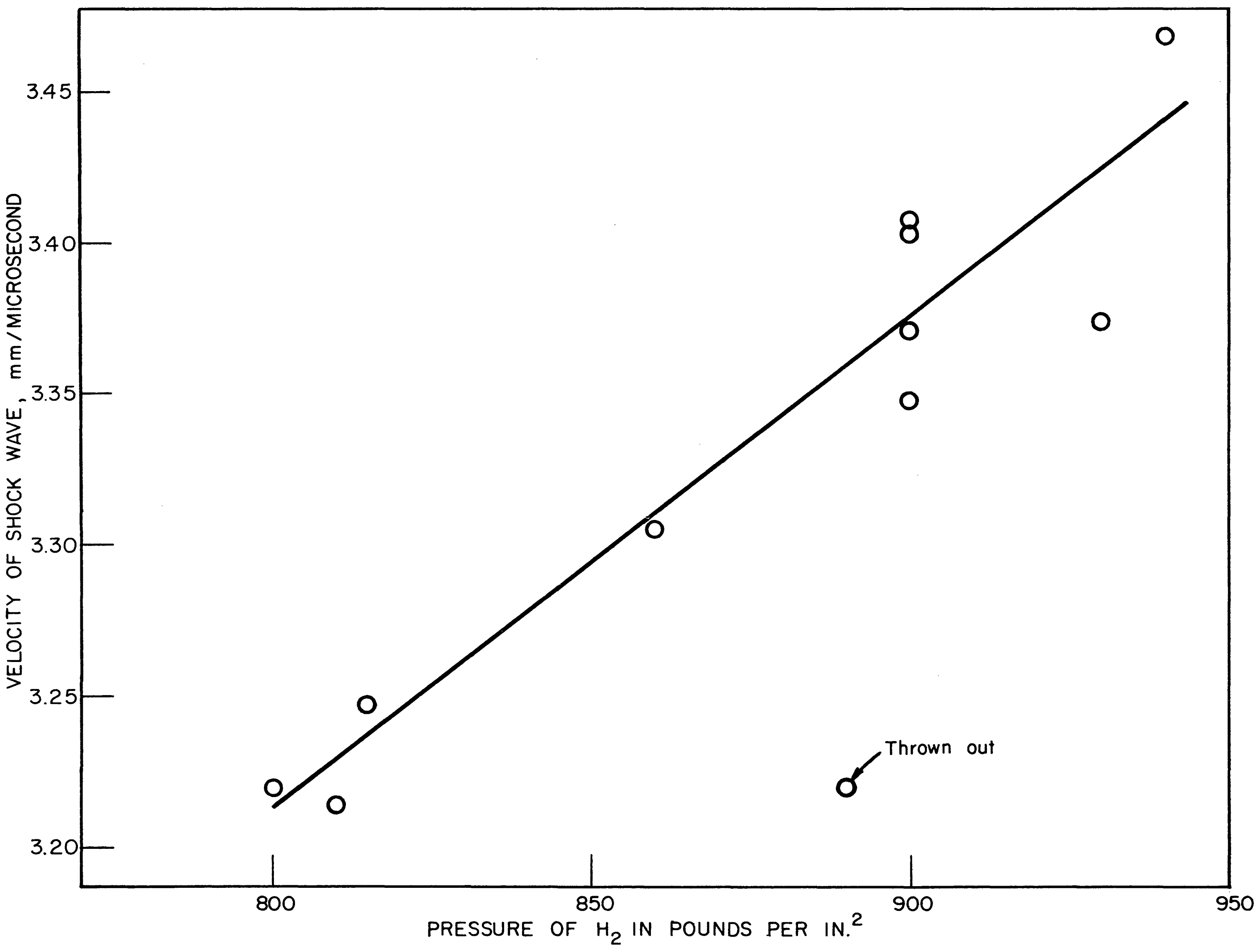

Figure 38. Shock velocity in neon + 45μ hydrogen at 0.769 mm Hg total pressure vs pressure of hydrogen driver gas.

experimental points was used to get an estimate of the probable error.

Several time-resolved spectra of H_β were made, using the setup shown in Figure 16, and the best ones were traced with a microdensitometer for reduction to intensity profiles. Two very good spectra were obtained with a pressure of 935 psia of hydrogen in the high-pressure chamber and one with a pressure of 870 psia. From the graph of Figure 38, the first corresponds to a primary shock velocity of 3.433 mm per microsecond and the second to a velocity of 3.326 mm per microsecond. The conditions behind the first reflected shock were then calculated as follows.

From equation (2.44) in Chapter II we can write

(7.1) $$y_{21} = \frac{1}{8}\left\{3+5\frac{U^2}{\frac{5}{3}R_1T_1}+5\sqrt{\left(\frac{U^2}{\frac{5}{3}R_1T_1}-1\right)^2+\frac{32}{15}\delta\frac{U^2}{\frac{5}{3}R_1T_1}\left(\frac{\Phi_{H_2}}{T_1}-1\right)}\right\},$$

where δ is the fraction of H_2 and Φ_{H_2} is the dissociation energy divided by the Boltzmann constant. Denoting the universal gas constant by R_0, R_1 is given by

(7.2) $$R_1 = \frac{R_0}{20.183(1-\delta)+2.016\delta}.$$

After finding y_{21} the density ratio is calculated from the Rankine-Hugoniot equation* [see equation (2.42)],

(7.3) $$X_{21} = \frac{4y_{21}+1}{y_{21}+4-2\delta\left(\frac{\Phi_{H_2}}{T_1}-1\right)}$$

and T_2 from

(7.4) $$\frac{T_2}{T_1} = \frac{1}{(1+\delta)}\frac{y_{21}}{X_{21}}$$

---

* $y_{21} = \frac{p_2}{p_1}$, $X_{21} = \frac{\rho_2}{\rho_1}$, etc. See Figure 1 for the numbering of the regions of the flow.

The flow velocity is then calculated, using the expression

$$U_2^2 = R_1 T_1 \left(\frac{X_{21} - 1}{X_{21}} \right) (y_{21} - 1) , \tag{7.5}$$

which comes from equation (2.22).

Next, one calculates the conditions behind the reflected shock. This cannot be done in closed form as above, but requires an iteration technique. Let ϵ be the fraction of atomic hydrogen, assuming that the molecular hydrogen is completely dissociated behind the primary shock.* Then

$$\varepsilon = 2\delta / (1 + \delta) .$$

The gas constant behind the primary shock wave is given by

$$R_2 = \frac{R_0}{20.183(1-\varepsilon) + 1.008\varepsilon} .$$

Using equations (2.33) and (2.36) given in Section 4 of Chapter II, we can write

$$X_{52} = \frac{4 y_{52} + 1}{y_{52} + 4 - 2 \dfrac{\alpha_{Ne}(1-\varepsilon)\theta_{Ne} + \alpha_H \varepsilon \theta_H}{T_2}} \tag{7.6}$$

and

$$\frac{T_5}{T_2} = \frac{1}{1 + (1-\varepsilon)\alpha_{Ne} + \varepsilon \alpha_H} \frac{y_{52}}{X_{52}} . \tag{7.7}$$

Using these, together with the Saha equations** [see equation (2.13)],

$$\begin{aligned} \log \frac{\alpha_H}{(1-\alpha_H)} (\alpha_{Ne} p_{Ne} + \alpha_H p_H) &= -13.60 \frac{5040.4}{T_5} + \frac{5}{2} \log T_5 - 0.477 \\ \log \frac{\alpha_{Ne}}{(1-\alpha_{Ne})} (\alpha_{Ne} p_{Ne} + \alpha_H p_H) &= -21.47 \frac{5040.4}{T_5} + \frac{5}{2} \log T_5 + 0.589 \end{aligned} \tag{7.8}$$

---

*For the reaction $2H \rightleftharpoons H_2$ the dissociation constant is given by $K = p_H^2 / p_{H_2}$. According to Lewis and von Elbe,[54] this constant at 5000°K is log K = + 1.64, where the pressures are given in atmospheres. For an initial pressure of H_2 of 45 microns and a shock strength of 68, the hydrogen is more than 99.96% dissociated at equilibrium.

**The logarithms are taken to the base 10. The expression $(\alpha_{Ne}\, p_{Ne} + \alpha_H\, p_H)$ is the electron pressure.

one calculates T_5, α_H, α_{Ne} for an assumed value of y_{52}. Then using

$$(7.9) \qquad (u_5 - u_2)^2 = R_2 T_2 \left(\frac{x_{52} - 1}{x_{52}}\right)(y_{52} - 1),$$

which comes from equation (2.22), the corresponding flow velocity u_5 can be calculated. This should, of course, be zero. One usually calculates T_5, α_H, α_{Ne}, and u_5 for two or three values of y_{52} and then interpolates to $u_5 = 0$.

The results of these calculations for the first group of experiments are given in Table V.

Using the calibration procedures described in the previous section, several intensity profiles of the H_β line were obtained. For the spectra obtained in the first group of experiments, the film was calibrated with a tungsten lamp at 1/100 sec and corrections were made for the change in γ with exposure time and for the transmission of the filter. A wavelength calibration was easily obtained by exposing the film with the spectrum of a neon Geissler tube. The line profile finally obtained for $p_4 = 935$ psia was a composite of a shot using a 100-micron slit to resolve the core of the line and a second shot using a 200-micron slit to bring up the wing intensity. The initial pressures were the same for the two shots. For $p_4 = 870$ psia, only one spectrum was obtained with a slit width of 100 microns. The slit widths were an appreciable fraction of the line widths. Therefore, it was necessary to correct the observed intensity profiles for the smearing-out caused by the wide slits.

A standard procedure for correcting the line shape for the slit width is to use a histogram method. The observed line intensity profile is divided up into wavelength units such that 5 (or some other odd integer) units are equivalent to the instrumental slit width. This is shown in Figure 39.

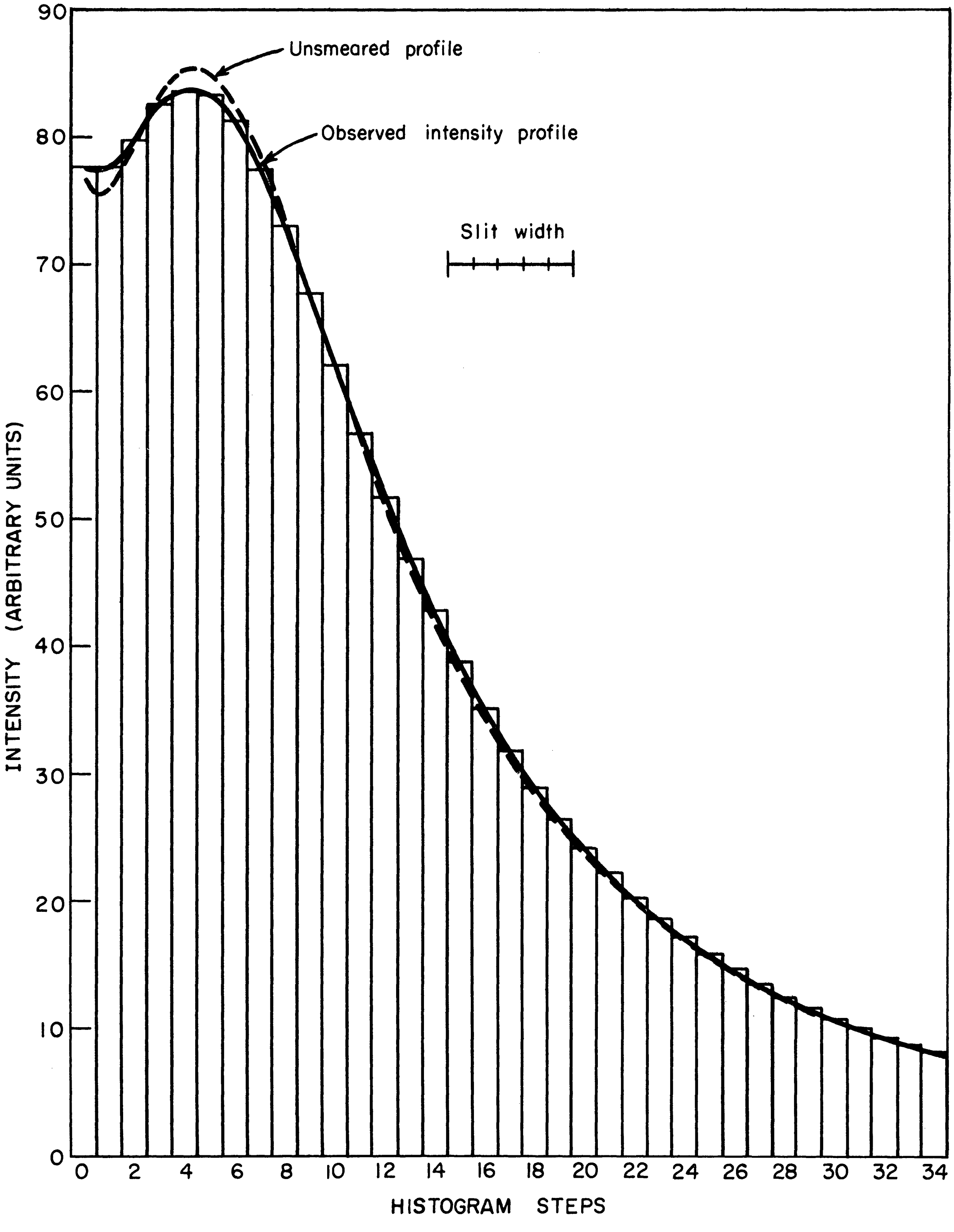

Figure 39. Histogram method of correcting line profile for slit width.

Then one calculates, using the histogram steps, the profile that would result if the observed line intensity profile were smeared out by the slit width. This is done by adding the intensity of each step to the two steps on either side and dividing the total by 5. Let us denote the observed line intensity by $I_1(\lambda)$ and the intensity of the smeared-out profile by $I_2(\lambda)$. Then, as a first-order approximation, the true line profile, $I_3(\lambda)$, is given by

$$I_3(\lambda) = I_1(\lambda) + \left[I_1(\lambda) - I_2(\lambda)\right] . \tag{7.10}$$

Further corrections can be made by smearing out $I_3(\lambda)$ and adding the difference between this and $I_1(\lambda)$, etc. As can be seen from Figure 37, however, the slit width has a very small effect on the line intensity profile, except in the core.

For the second group of experiments the time-resolved spectrum and the wave-speed picture were obtained simultaneously. For a time-resolved spectrum a revolving drum camera is mounted on the grating spectrograph as shown in Figure 16. The Bausch and Lomb grating with 1200 lines per mm was used to give a dispersion of 5.32 Å per mm at 4861 Å. The slit width was 500 microns.

The spectrum of H_β obtained was very good, but there was some difficulty with the intensity calibration of the film. The xenon flash lamp and the 7-step filter were used as described in Section 6, but the grating was not masked, so the ends of slit image were of reduced intensity due to vignetting. Afterwards a good calibration was made and the film was developed under the same conditions as the original. For the most accurate results, however, the film with the time-resolved spectrum and the calibration film should be developed together in the same tank. The writer feels, however, that even with this difficulty the calibration for the second group of spectra is better than for the first group.

The hydrodynamic variables were calculated in the same manner as before and the results are summarized in Table V. A comparison of the results of the second group with those of the first shows the effect of adding more hydrogen to the neon. The ion density, however, is changed very little.

The three intensity profiles of H_β which we have discussed are shown in Figure 40. One sees the blue maximum slightly higher than the red. This effect was reported by Griem,[55] describing his experiments with the whirling-water arc at Kiel.* He attributed the difference in the heights of the maxima to the second-order Stark effect, the dependence of the intensity on the frequency, and the transformation from the frequency to the wavelength scale.

The experimental results reported here are confined to a rather narrow range of ion densities. There are several reasons for this. The lower limit is due to the marginal amount of light available for time-resolved spectroscopy and also to the increasing time for the establishment of ionization equilibrium behind the reflected shock. The upper limit could have been extended slightly by the use of even higher pressures of the hydrogen driver, but for a significant increase one would have to use an explosive driver of hydrogen and oxygen. At the time these experiments were made, the methods of setting off the explosive driver gave inconsistent results. Also, the profiles of H_β were somewhat self-absorbed in the core.

With new techniques for burning the explosive driver, with the use of two drum cameras for simultaneously obtaining a wave-speed picture and a

---

*The work by Griem will be discussed in more detail in Chapter VI.

Table V. Results of Hydrodynamic Calculations

	Group I Experiments		Group II Experiments
p_1 (cm Hg)	0.769	0.769	0.777
T_1	295°K	295°K	299.5°K
δ	0.00585	0.00585	0.0135
U (mm/μ sec)	3.433	3.326	3.330
y_{21}	72.8	68.35	67.88
T_2	5454°K	5158°K	4948°K
u_2 (mm/μ sec)	2.555	2.474	2.508
y_{52}	5.708	5.703	5.916
T_5	12,050°K	11,555°K	11,300°K
α_5^{H}	0.309	0.254	0.165
α_5^{Ne}	0.0025	0.00136	0.00067
N_{ions} (1/cm^3)	1.55×10^{16}	1.08×10^{16}	1.345×10^{16}
$\Delta\lambda_{1/2}$ (Experimental)	12 Å	10.5 Å	13.8 Å

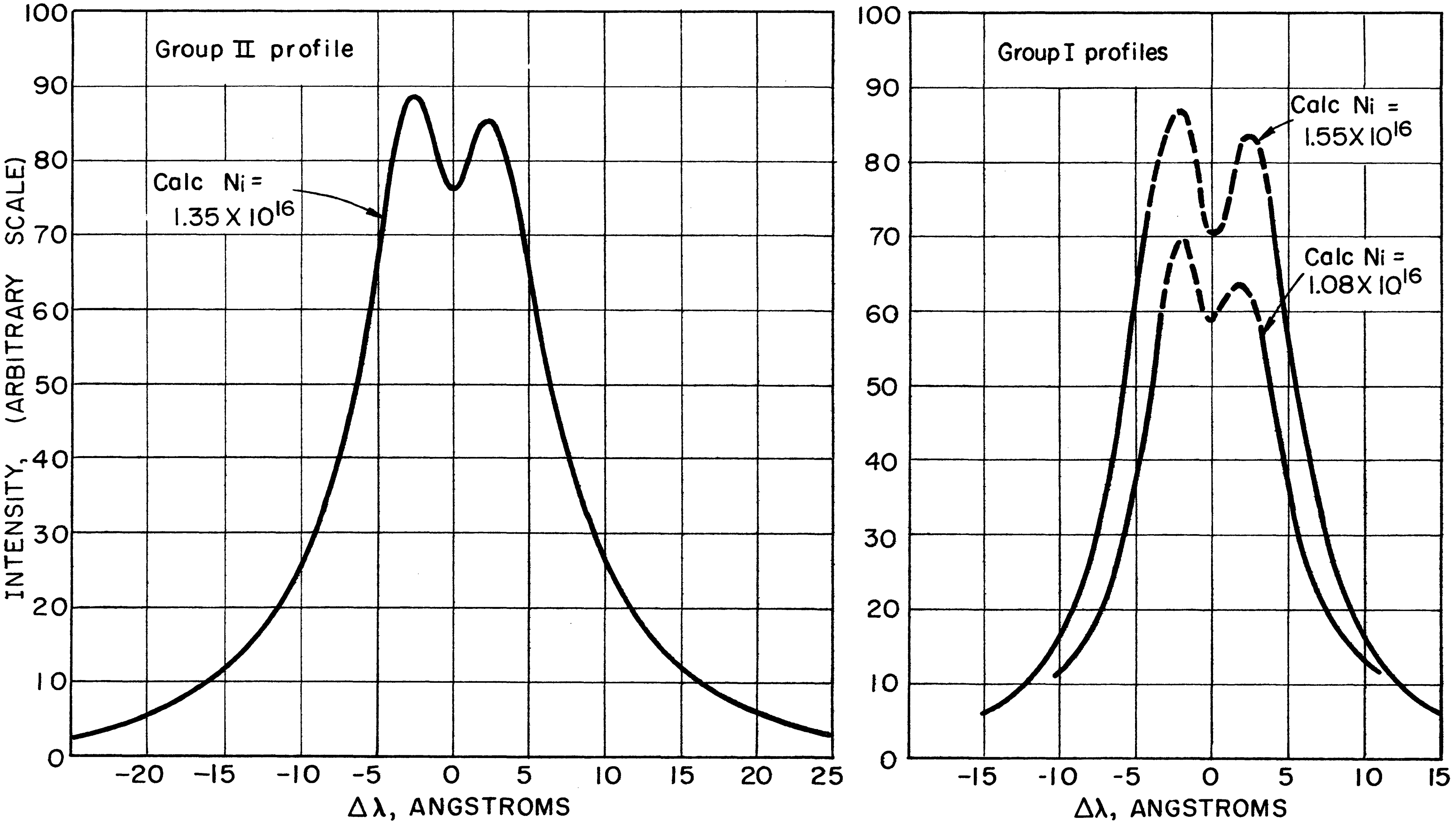

Figure 40. Experimental line intensity profiles of H_β.

time-resolved spectrum, and with the proper correction of the line profiles for self-absorption it should be possible to obtain reliable results at ion densities of ten times as great as reported here.

This section on calculations and results would not be complete without a discussion of the errors of measurement and their effect on the calculated values of the ion density. Also, the effect of photometric errors on the line shape will be discussed.

The pressure, p_1, was measured with a di-butyl phthalate manometer which was accurate to ± 0.5 mm or ± 0.5% in 100 mm. The measurement of the amount of hydrogen added to the neon was somewhat less accurate—probably ± 5%. The pressure in the high-pressure chamber was known to within 1/2 of a scale division or ± 5 psia. This does not consider the total accuracy of the gauge at about 900 psia, which was 10 psia, but only the accuracy of the difference between two readings in a narrow range. The revolution counter, with which the drum speed of the camera was measured, was accurate to ± 1/4%, according to the manufacturer. There were also errors in the measurement of the shock velocity, using the method described in Section 2, Chapter IV. Several measurements of the same film brought this error down to ± 0.4%.

All of these errors can be reduced. A film comparator would reduce the error in the film measurement and an electronic revolution counter probably would decrease the error of the drum speed to less than ± 0.1%. Refinements also could be made in the manometer scales.

To find the effect of these errors on the calculated ion density is a somewhat subtle problem. The worst error was in the determination of the amount of hydrogen added to the neon, but calculations have shown that this has very little effect on the ion density. For a typical initial pressure ratio, the ion density changed by only 7% over the range of $\delta = 0$ to $\delta = 0.015$, i.e., from no hydrogen to 1-1/2%. An error in δ of ± 10% has almost no effect on the primary shock velocity. The error in the initial pressures causes an uncertainty in shock velocity for the Group I experiments but not for Group II. From Figure 38 it was determined that an error of ± 5 psia in the high-pressure reading results in a shock-velocity error of ± .008 mm/microsecond. The error in reading the low-pressure manometer results in about the same uncertainty in the velocity. According to the scatter of points in Figure 38, the probable error of a point on the curve is ± .006 mm/microsecond for a given pressure. The probable error in the camera drum speed contributes an uncertainty of ± .008 mm/microsecond. The cumulative effect of all of these is a probable error in the shock velocity of ± 0.015 mm/microsecond.

The determination of the uncertainty in the ion density is a tedious process. The best method is to make two complete sets of calculations, one for U and one for $U + \Delta U$. Using this procedure we have found that for Group I, where $\Delta U = 0.015$ mm/microsecond, the probable error in the ion density is ± 15%. The Group II experiments were inherently more accurate because the shock velocity was measured simultaneously with the exposure of the time-resolved spectrum. The only errors which contributed to an uncertainty in the shock velocity were the drum-speed measurement and the measurement of the shock velocity from the film. The additive effect of these two was to give a probable error of ± 0.013 mm/microsecond in the shock velocity, resulting in an error in the calculated ion density of ± 10%. By using the suggestions given previously, this error probably could be made less than ± 5%.

The errors of photometry are the most difficult to evaluate. In the absence of any systematic experimental investigation of these errors, the best that can be done is to make a conservative estimate. The photometry for the Group II experiments is the best. The error varies from ± 5% at the line maximum to perhaps ± 30% at 25 Å from the line center. This, however, affects the observed half-width by only ± 3%. The photometry for the Group I experiments was somewhat worse, as it involved two corrections to the original data.* The error at maximum intensity could be ± 10% with ± 50% error on the far wings. The reason for the large error in the wings of the line is the difficulty in measuring small film densities accurately. The grain of the film causes a very irregular microdensitometer trace through which it is difficult to draw an accurate mean value.

8. Comparison of H_β Profiles with Theory

The calculated ion densities and the corresponding experimental half-widths of H_β have been plotted as points on a log-log graph shown in Figure 41. If these points were accurate, they should lie on a smooth curve which, in the narrow range represented here, would be close to a straight line. As one can see, this is not the case, and the errors are somewhat greater than those which were previously estimated (indicated by error flags). In order to get the most out of the these results, the following averaging procedure was employed.

It was assumed that the half-widths are proportional to $N_i^{2/3}$, as in the Holtsmark theory, so lines of slope 3/2 were drawn through the points. First, the two points from the first group of experiments were averaged together by drawing a line (not shown), with slope 3/2, halfway in between the lines through these points. Then an average curve was drawn halfway

---

*See Section 6 of this chapter.

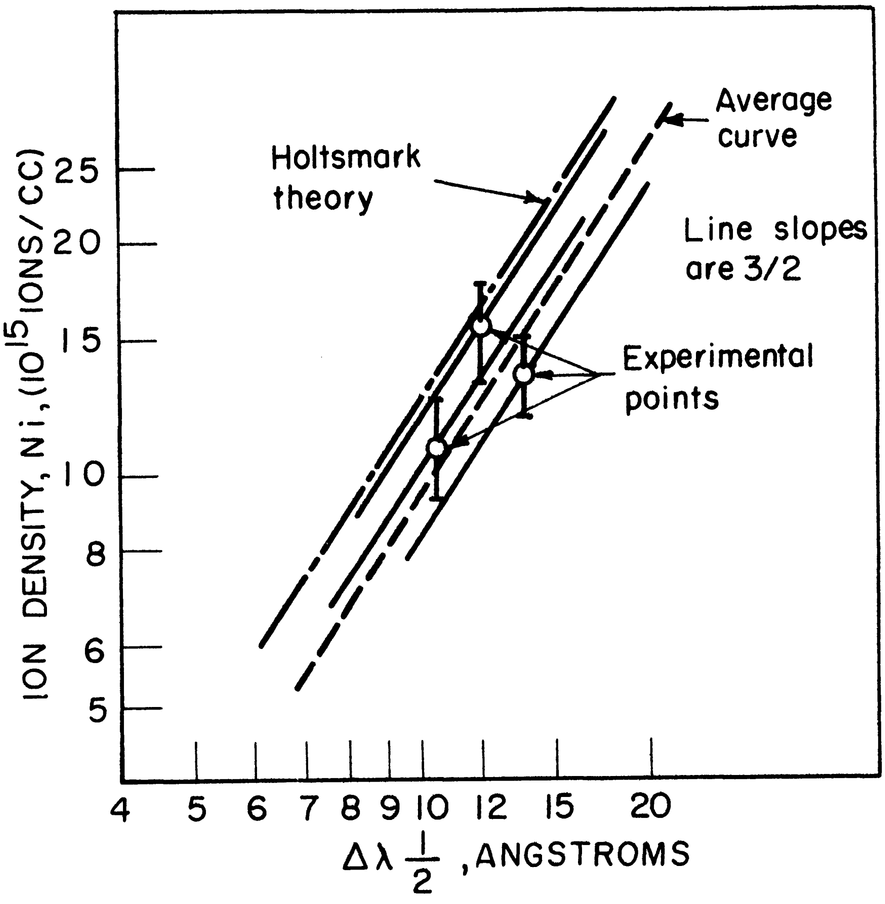

Figure 41. Method of averaging ion densities and comparison of experimental points with Holtsmark theory.

between this and the line through the point from the second group of experiments, effectively giving double weight to the latter point because of its greater accuracy. Also shown is a curve for the Holtsmark theory.

The average curve has a probable error of about 10% in ion density or 8% in half-width, according to the scatter of the points. This, however, does not include any possible systematic error. According to the average curve obtained, the observed half-widths were approximately 20% larger than predicted by the Holtsmark theory. More accurate data are needed before it can be stated definitely that the Holtsmark theory predicts too small a half-width, but, nevertheless, it is indicated that there must be another broadening mechanism, besides the static field of the ions, to account for the increased width.

Besides the half-widths, it is also very interesting to compare the experimental and Holtsmark line profiles for H_β in more detail. The profile from the second group of experiments is used for comparison because of the better photometry, but the ion density used to plot the Holtsmark profile is not the calculated value but the value given by the average curve in Figure 41 for the observed half-width of 13.8 Å—namely, 1.55×10^{16} ions per cc. The experimental and Holtsmark profiles are shown in Figure 42. They are normalized to the same total intensity. Two features are evident. First, the position of the maximum is the same for the two profiles. Second, the experimental profile is much less intense in the core of the line but has almost twice the intensity in the wings as the Holtsmark profile.

Kolb[56] has reconsidered the theory of hydrogen line broadening and has included the effects of the fast-moving electrons as well as the static field of the ions. The electrons were considered in the classical path approximation without restricting the theory to binary collisions. Non-adiabatic as well as adiabatic effects were considered and were shown to be comparable in their contribution to the electron broadening. Although Kolb has not computed a profile for H_β at the time of the writing of this dissertation, several features of his theory fit the experimental results rather well. Kolb's theory predicts an additional half-width of only 20% for H_γ (it should be a little less for H_β), but he finds that the intensity on the wings is increased by an amount comparable to the intensity of the Holtsmark profile. This additional intensity in the wings will cause a reduced intensity in the core since the total line intensity must remain constant. Also, Kolb has found that the intensity of H_β does not go to zero in the center of the line. It can therefore be said that the experimental

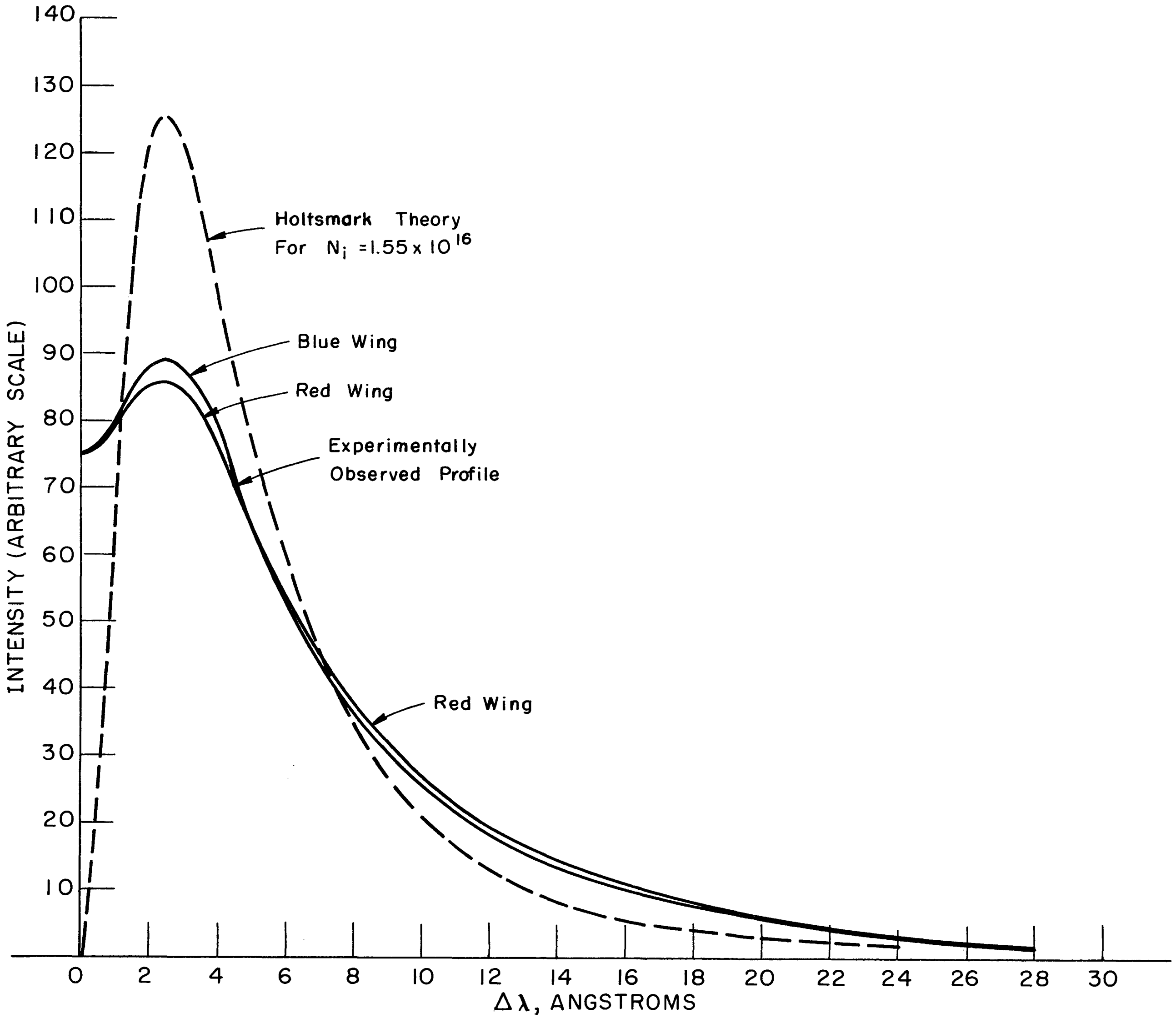

Figure 42. Comparison of an experimental profile with the Holtsmark theory for H_β.

results obtained so far with the shock tube fit the Kolb theory somewhat better than the Holtsmark theory.

CHAPTER VI

SUMMARY, CRITIQUE, AND SUGGESTIONS FOR FUTURE EXPERIMENTS

The data obtained from the luminous shock tube fall into two general categories, namely, hydrodynamics and spectroscopy. The first part of this chapter is devoted to a discussion of the hydrodynamic results.

Measurements were made of the primary shock velocity in all the rare gases, using a wave-speed camera. A comparison with the theory showed that the observed shock velocities were considerably less than those predicted for given initial pressure ratios. The main reason for this probably is attenuation of the shock wave by boundary layer and heat conduction at the walls. It has been shown by Hollyer[11] and others that this attenuation causes a nonhomogeneity in the conditions from the shock front back to the interface for medium shock strengths. In order to minimize these effects, the spectral observations were made very close to the end of the tube. Thus the conditions probably are quite close to those calculated when using the shock velocity measured near the end of the tube. More information on the attenuation at these high shock strengths and on the effect on the flow variables would be very valuable. It should be determined, for example, if the shock attenuation can be decreased by the use of very smooth walls.

The reflected shock velocities were also measured in argon in an effort to find the effect of ionization behind the reflected shock wave. The measured velocities were somewhat less than those predicted by the ideal theory, clearly showing the effect of ionization, but they were slightly greater than those predicted by the theory including ionization, thus appearing to indicate a little less than equilibrium ionization. The results of Kantrowitz and co-workers show that ionization equilibrium is reached behind the primary shock in argon, so our results probably can be attributed to another cause such as radiation cooling and the effects of attenuation mentioned above. The question of thermodynamic equilibrium behind the reflected shock wave is quite important, and therefore a suitable explanation should be found for this discrepancy in the reflected shock velocities.

A study was also made of the very interesting phenomenon of the delay time for ionization behind the primary shock in xenon. This delay time is somewhat analogous to the relaxation times for vibration and dissociation in diatomic gases. The xenon used for these experiments was from a steel cylinder of mass-spectrometer-checked gas, a gift of the Linde Air Products Co. Measurements were made at a series of shock strengths for three initial pressures, $p_1 = 0.5$, 1.0, and 2.0 cm Hg. These measurements seemed quite self-consistent and the delay time for any given shock velocity was found to vary inversely with density, as one would expect. More recent results obtained with a sample of spectroscopically pure xenon from a pyrex flask (also from Linde Air Products Co.) gave delay times approximately five times as great for a given shock velocity. Since both gas samples were quite pure, this indicates a strong dependence of the delay time on rather small amounts of impurities. Further investigations into this phenomenon should prove quite fruitful. The writer has learned that H. E. Petschek of Cornell University has recently written a doctoral dissertation on the subject of the approach to ionization equilibrium behind a strong shock wave in argon. Petschek has found that the electron temperature is lower than the effective temperature of the atoms and ions in the nonequilibrium region,*

---

*The effective translational temperature of the atoms in the nonequilibrium region is considerably higher than the equilibrium temperature attained after ionization.

which contradicts one of Bond's assumptions. The writer has not yet read the completed dissertation and therefore is not able to comment further on the work.

Some studies were also made on the interface between the cold and hot flow in the shock tube. It was found to be quite extended and turbulent, as one might expect from the finite time required to burst the diaphragm. In spite of the width of the interface, however, it was found that the hydrogen does not diffuse into the hot flow, so one can be sure of the purity of the luminous gas.

An investigation was made in an effort to find out why the shock front, for a strong shock wave in a rare gas, appears as a thin luminous line, even though there may be no luminosity immediately behind the front. First of all it was found, by taking a wave-speed picture with the revolving drum camera placed a few degrees from the perpendicular to the tube, that the luminosity of the front was not confined to the walls but extended across the tube. Then, by using a special spectrographic arrangement, a spectrum of the luminous front was obtained which showed the C_2 and the CN bands. Therefore, the luminosity of the front is due merely to molecular vapors in the tube.

Most of the spectroscopic observations were made of the luminous region behind the reflected shock at the end of the tube. In this region it is possible to obtain relatively high temperatures ($\sim$ 12,000°K), even in a fairly light gas such as neon, with a high-pressure hydrogen driver. Subsequent shocks, however, are produced by the interaction of the first reflected shock with the interface. These cause an increase in the temperature of the luminous gas. This problem was studied both theoretically and experimentally.

Spectra of the rare gases were obtained for a wide range of shock strengths. They show many qualitative features such as the recombination continuum, the lines of metallic impurities, and the broadening of the rare-gas lines. The argon lines were symmetric in shape and shifted to the red as predicted by the Lindholm-Foley theory of collision broadening, but the xenon lines exhibited a very definite red asymmetry. The strong infrared lines were too self-absorbed to draw any conclusions about the line shapes. This self-absorption could be made negligible by using mixtures of the rare gases (i.e., 5% xenon in argon). This has the additional advantage that one might discover whether the asymmetry of the xenon lines is due to the ions or to the characteristics of the xenon lines. If the slow-moving xenon ions cause the asymmetry, then the argon lines would also be asymmetric. To the writer's knowledge, no quantitative line intensity profiles have been obtained for the rare-gas lines. This measurement requires time resolution of the spectra and a good film calibration. Using the techniques that have been recently developed, such measurements should not be too difficult and would provide line intensity profiles of the rare gases that could be checked in more detail with the current theories of second-order Stark broadening.

Several line intensity profiles were obtained of the hydrogen line H_β from time-resolved spectra of the luminosity of gas mixtures. About 1% hydrogen was added to neon, and the temperatures and ion densities behind the first reflected shock were calculated from the measured primary shock velocities, taking into account both the effect of the dissociation of hydrogen and the effect of ionization. Comparison with the Holtsmark theory of first-order Stark broadening showed the observed profiles to be about 20% wider as well as somewhat different in shape. Kolb has attributed this additional broadening to the effects of the fast-moving electrons. In the opinion of the writer, much work still remains to be done on the study of hydrogen lines in the shock tube. So far only H_β has been studied in detail and the spectrograph used was too slow to obtain accurate intensities on the wings, but the intensity profile of the wings is far more important for astrophysical applications than the profile of the core. Therefore, additional work should be done on the wings of H_β with a fast spectrograph. Intensity profiles should also be obtained for the other relatively strong Balmer lines, i.e., H_α, H_γ, and H_δ. In addition it would be worthwhile to determine the last discrete Balmer line and thus check the Inglis-Teller[57] formula, to measure the ratio of intensities of the Balmer lines in order to make sure the Boltzmann distribution is established among the excited levels, and to measure the intensity distribution of the continuum beyond the Balmer limit.

A discussion of experimental work on hydrogen line broadening would not be complete without mentioning the work done by Jürgens,[58] Griem,[55] and others at the Institut für Experimentalphysik at Kiel, Germany, under Prof. W. Lochte-Holtgreven. At this laboratory a unique tool for the investigation of high-temperature gases has been developed. It is a high-current arc which is stabilized by an envelope of whirling water. The water is dissociated and the hydrogen and oxygen are partially ionized. Temperatures of approximately 12,000°K and ion densities of about 8×10^{16} have been obtained. This arc has the advantage that exposures may be made over a relatively long period of time, but it has the disadvantage of most arcs in that the temperature and ion density are not homogeneous across the arc. Assuming cylindrical asymmetry, Jürgens used several independent methods, including the use of the Holtsmark line profiles, for the determination of the temperatures and ion densities at the axis of the arc and obtained excellent internal agreement. His experiments appeared to show the validity of the Holtsmark theory. Shortly thereafter, Griem developed a theory of hydrogen line broadening* which included the effect of the fast-moving electrons. The agreement between the theory and the experimentally determined line profiles was also quite good, and the ion densities determined in this manner were about 30% lower than those of Jürgens. One discrepancy between Griem's results and ours was in the shape of H_δ. Both his theory and observations show no minimum in the center of H_δ, but this minimum shows up clearly in the shock-tube spectrum (see Figure 33). This shows that Griem's theory is not adequate and that the arc, even when viewed end-on through a hole in the electrode as Griem has done, is not homogeneous along the axis. Nevertheless, Griem's work is very significant and shows that the shock-tube results which indicate a broadening slightly greater than the Holtsmark theory are not in disagreement with the results of the whirling-water arc, in spite of the results reported by Jürgens.

Several features of Kolb's theory of hydrogen line broadening are in agreement with the shock-tube line profiles, but, because of the difficulty of the calculations, he has not yet given a complete line intensity profile of H_β which could be compared with the shock-tube results. An approximate form of the Kolb theory, which is quite accurate on the far wings, has been derived. Because of the rather large absorption in the core of the hydrogen lines, the far wings contribute most to the absorption line shape observed in stellar spectra, and it is in the far wings, according to Kolb, that the electron broadening is most important. This approximate form of Kolb's

---

*The theory developed by Griem is not the same as the theory by Kolb. The differences will be discussed in Kolb's dissertation.[56]

theory has been applied to B-stars by Elstie, Jugaku, and Aller,[58] and the agreement with the observed profiles was far better than could be obtained with the Holtsmark theory.

APPENDICES

APPENDIX A. DERIVATION OF SHOCK-WAVE EQUATIONS

APPENDIX B. THE FLOW VELOCITY CHANGE ACROSS A RAREFACTION WAVE

APPENDIX C. THE PROPERTIES OF $\phi(p)$ AND $\psi(p)$

APPENDIX D. CALCULATION OF THE H_β INTENSITY BEHIND THE REFLECTED SHOCK

APPENDIX A

DERIVATION OF SHOCK-WAVE EQUATIONS

Consider a shock wave in a tube of constant cross section as shown in the diagram below. Let p_a, ρ_a, h_a, and u_a be the pressure, density, specific enthalpy, and flow velocity ahead of the shock wave, and let p_b, ρ_b, h_b, and u_b be the corresponding variables behind the shock wave. It is not

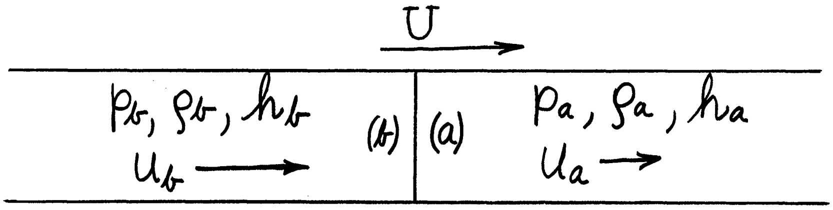

necessary to state at this point whether side (a) or side (b) has the higher pressure, and the equations derived below will indeed apply to either case. It is more convenient to consider the flow velocities relative to the shock wave. If we denote the shock velocity by U, the flow velocities relative to the shock wave will be

$$v_a = u_a - U$$

$$v_b = u_b - U$$

where velocities are considered positive toward the right.

We will start with the well-known conservation conditions across a normal shock wave.

(A.1) $\rho_a v_a = \rho_b v_b$ conservation of mass

(A.2) $\rho_a v_a^2 - \rho_b v_b^2 = p_b - p_a$ conservation of momentum

(A.3) $\frac{1}{2} v_a^2 + h_a = \frac{1}{2} v_b^2 + h_b$ conservation of energy.

Courant and Friedrichs[22] (Chapter III, C) have derived these equations in an elegant manner and have shown that they are valid under the assumptions that heat is not added to or removed from the gas and that viscosity and heat conduction are negligible.

From these three so-called "jump conditions" one can proceed to derive relations between the variables across a shock wave. Squaring equation (2.1), multiplying equation (2.2) by ρ_a, and subtracting gives

$$v_b^2 = \frac{\rho_a}{\rho_b} \frac{(p_b - p_a)}{(\rho_b - \rho_a)}$$

and in a similar manner

$$v_a^2 = \frac{\rho_b}{\rho_a} \frac{(p_b - p_a)}{(\rho_b - \rho_a)} .$$

Putting these expressions for v_a^2 and v_b^2 into equation (2.3) results in the well-known Hugoniot relation

$$h_b - h_a = \frac{1}{2}\left(\frac{1}{\rho_b} + \frac{1}{\rho_a}\right)(p_b - p_a) . \tag{A.4}$$

The specific enthalpy is defined as

$$h = e + p/\rho$$

where e is the specific internal energy. Assuming a gas with constant specific heat, the internal energy is $e = C_vT$. Then the enthalpy is

$$h = C_v \frac{p}{R\rho} + \frac{p}{\rho} = \frac{C_v + R}{R} \frac{p}{\rho} = \frac{C_p}{C_p - C_v} \frac{p}{\rho} = \frac{\gamma}{\gamma - 1} \frac{p}{\rho} .$$

R is the universal gas constant divided by the molecular weight and $\gamma = C_p/C_v$. Putting this expression for the enthalpy into the Hugoniot equation (2.4) and solving for the density ratio, one gets

(A.5)
$$\frac{\rho_b}{\rho_a} = \frac{1 + \frac{\gamma+1}{\gamma-1} \frac{p_b}{p_a}}{\frac{\gamma+1}{\gamma-1} + \frac{p_b}{p_a}} .$$

This is known as the Rankine-Hugoniot equation. It is convenient to set

$$\frac{\gamma+1}{\gamma-1} = \mu .^{*}$$

Then the above equation is written

(A.6)
$$\frac{\rho_b}{\rho_a} = \frac{1 + \mu \frac{p_b}{p_a}}{\mu + \frac{p_b}{p_a}} .$$

The density ratio asymptotically approaches the limit μ as the pressure ratio becomes infinite.

---

*The symbol μ is equal to the number of degrees of freedom plus one. For a monatomic gas $\mu = 4$ and for most diatomic gases at room temperature $\mu = 6$. This is not the same as the μ used in the book by Courant and Friedrichs.[22] They use $\mu^2 = \frac{\gamma-1}{\gamma+1}$.

By using the equation of state for an ideal gas

$$p = \rho R T,$$

the temperature ratio across a normal shock can be found from equation (2.6).

(A.7) $$\frac{T_b}{T_a} = \frac{p_b}{\rho_b}\frac{\rho_a}{p_a} = \frac{p_b}{p_a}\frac{\mu + \frac{p_b}{p_a}}{1 + \mu\frac{p_b}{p_a}} .$$

Next we will derive expressions for the shock and flow velocities as a function of the pressure ratio. The mass flow through the shock is

$$m = -\rho_a v_a = -\rho_b v_b ,$$

using equation (2.1) and considering the sign convention that has been adopted. The conservation-of-momentum equation (2.2) can then be written

$$m(v_b - v_a) = p_b - p_a$$

from which

(A.8) $$m = \frac{p_b - p_a}{v_b - v_a} = \frac{p_b - p_a}{u_b - u_a} .$$

The expressions u_b and u_a are the absolute velocities. The conservation-of-momentum equation can also be written

$$m^2\left(\frac{1}{\rho_a} - \frac{1}{\rho_b}\right) = p_b - p_a \quad \text{or} \quad m^2 = \frac{\left(\frac{p_b}{p_a} - 1\right)}{\left(1 - \frac{\rho_a}{\rho_b}\right)} p_a \rho_a .$$

Equation (2.8) is then squared and set equal to the above.

$$\text{(A.9)} \qquad \frac{\left(\frac{p_b}{p_a}-1\right)}{\left(1-\frac{\rho_a}{\rho_b}\right)}\, p_a \rho_a = \left(\frac{p_b-p_a}{u_b-u_a}\right)^2 .$$

Putting in the expression for the density ratio from the Rankine-Hugoniot equation (2.6) and solving for $(u_b - u_a)^2$ gives

$$\text{(A.10)} \qquad (u_b-u_a)^2 = \frac{(\mu-1)\left(\frac{p_b}{p_a}-1\right)^2}{\left(1+\mu\frac{p_b}{p_a}\right)}\,\frac{p_a}{\rho_a} .$$

The sound speed of an ideal gas is

$$c = \sqrt{\gamma\frac{p}{\rho}} = \sqrt{\frac{\mu+1}{\mu-1}\,\frac{p}{\rho}}$$

or

$$\frac{p}{\rho} = c^2\,\frac{\mu-1}{\mu+1} .$$

Substituting for p_a/ρ_a in equation (2.10) and taking the square root gives

$$\text{(A.11)} \qquad u_b = u_a \pm \frac{(\mu-1)\left(\frac{p_b}{p_a}-1\right)c_a}{\sqrt{(\mu+1)\left(1+\mu\frac{p_b}{p_a}\right)}} .$$

To obtain an expression for the shock velocity we use the continuity equation (A.1) and the Rankine-Hugoniot equation (A.6).

$$\frac{1+\mu\frac{p_b}{p_a}}{\mu+\frac{p_b}{p_a}}=\frac{\rho_b}{\rho_a}=\frac{v_a}{v_b}=\frac{u_a-U}{u_b-U}\,.$$

Using equation (A.11) for u_b in the above and solving for U one gets

$$U=u_a\pm\sqrt{\frac{1+\mu\frac{p_b}{p_a}}{\mu+1}}\,c_a\,. \qquad \text{(A.12)}$$

Again the plus sign is used for shock waves facing to the right and the minus sign for shock waves facing to the left. One can see from this last equation that the pressure ratio across the shock wave, which we will hereafter call the shock strength, is easily calculated from the shock velocity, a quantity that can be readily measured. Then from equations (A.6), (A.7), and (A.11) the density, temperature, and flow velocity may be calculated. Therefore all the variables behind a shock wave are determined once the shock velocity and, of course, the conditions ahead of the shock are known.

APPENDIX B

THE FLOW VELOCITY CHANGE ACROSS A RAREFACTION WAVE

As for the case of shock waves we will consider the rarefaction wave to be bounded by constant states (a) and (b). The problem is to find the flow-velocity difference across such a rarefaction wave for a given pressure ratio, p_a/p_b. The rarefaction wave is included between the rarefaction head on the high-pressure side and the rarefaction foot on the low-pressure side. The head of the rarefaction moves into the gas on the left with a constant velocity $(u_a - c_a)$ since all signals in an isentropic flow are propagated with the speed of sound. Similarly, the foot of the rarefaction moves with the velocity $(u_b - c_b)$. In the diagram above the rarefaction is said to be facing toward the left since the fluid is moving into the wave from the left. This definition is similar to that for shock waves. Conversely, a rarefaction is said to be facing to the right if the fluid enters the front from the right-hand side.

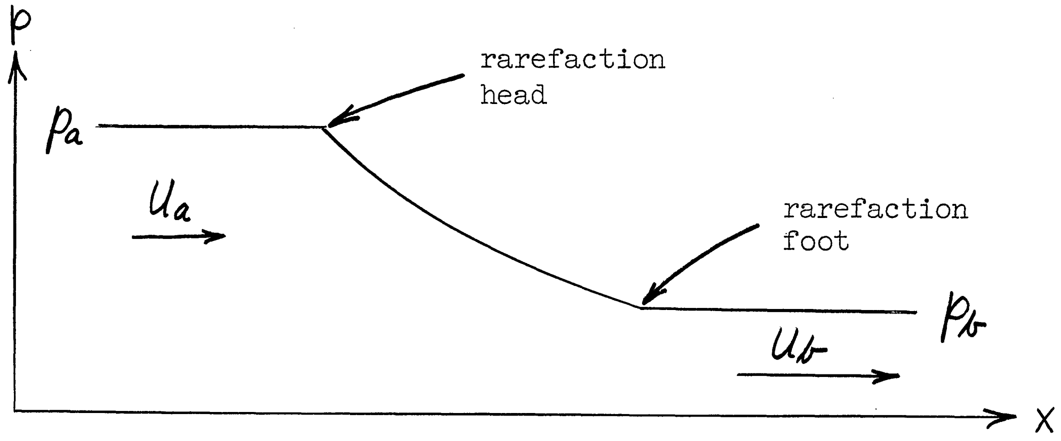

Now in order to solve for the flow-velocity difference across a rarefaction, we first write down the one-dimensional time-dependent differential equations for compressible flow:

(B.1) $$\frac{\partial \rho}{\partial t} + u\frac{\partial \rho}{\partial x} + \rho\frac{\partial u}{\partial x} = 0$$ continuity equation.

(B.2) $$\rho\frac{\partial u}{\partial t} + \rho u\frac{\partial u}{\partial x} + \frac{\partial p}{\partial x} = 0$$ equation of motion.

(B.3) $$\frac{\partial S}{\partial t} + u\frac{\partial S}{\partial x} = 0$$ for an adiabatic and reversible process.

S is the specific enthalpy. Assume that the pressure is a function of the density and specific enthalpy.

$$p = p(\rho, S) .$$

Then

$$dp = \frac{\partial p}{\partial \rho} d\rho + \frac{\partial p}{\partial S} dS = c^2 d\rho + \frac{\partial p}{\partial S} dS .$$

since the sound velocity is given by

$$c^2 = \left(\frac{\partial p}{\partial \rho}\right)_S .$$

Solving for the density

$$d\rho = \frac{dp}{c^2} - \frac{1}{c^2}\frac{\partial p}{\partial S} dS .$$

Substituting this expression for dρ into equation (B.3) gives

$$\frac{\partial p}{\partial t}+u\frac{\partial p}{\partial x}+c^2\rho\frac{\partial u}{\partial x}-\frac{\partial p}{\partial S}\left\{\frac{\partial S}{\partial t}+u\frac{\partial S}{\partial x}\right\}=0.$$

The term in brackets is zero by equation (B.3) so the above reduces to

(B.4) $$\frac{\partial p}{\partial t}+u\frac{\partial p}{\partial x}+c^2\rho\frac{\partial u}{\partial x}=0.$$

Now equation (B.2) is multiplied by c and added to and subtracted from equation (B.4). This results in two new equations.

(B.5) $$\frac{\partial p}{\partial t}+(u+c)\frac{\partial p}{\partial x}+\rho c\left[\frac{\partial u}{\partial t}+(u+c)\frac{\partial u}{\partial x}\right]=0$$

(B.6) $$\frac{\partial p}{\partial t}+(u-c)\frac{\partial p}{\partial x}-\rho c\left[\frac{\partial u}{\partial t}+(u-c)\frac{\partial u}{\partial x}\right]=0.$$

A derivative of the form

$$\frac{\partial}{\partial t}+(u+c)\frac{\partial}{\partial x}$$

is a directional derivative in the direction

(B.7) $$dx=(u+c)dt$$

so that equation (B.5) can be written as

(B.8) $$dp+\rho c\,du=0$$

where the derivatives are taken in the direction defined by equation (B.7).

Similarly, equation (B.6) can be written as

(B.9) $$dp - \rho c\, du = 0$$

where the derivatives are taken in the direction

(B.10) $$dx = (u - c)dt.$$

Also dS = 0 along the direction dx = udt, which is the particle path.

The curves which are defined by the directions dx = (u + c) dt and dx = (u - c) dt are called the C_+ and C_- characteristic curves, respectively. Integrating to obtain the curves, we have

(B.11) $$\begin{aligned} x &= (u+c)t + C_1 \quad \text{and} \\ x &= (u-c)t + C_2 \ . \end{aligned}$$

Therefore the C_+ characteristic curves are a one-parameter family in C_1, the constant of integration, and the C_- characteristics are a one-parameter family in C_2. These two families of curves then form a net throughout the flow field. For a rarefaction wave facing to the right the head and foot of the rarefaction are clearly C_+ characteristics, and for a rarefaction facing to the left they are C_- characteristics.

The problem is to find the flow-velocity change across a rarefaction wave. This can be done by integrating du from one constant state (a) to the other constant state (b). If the rarefaction is facing to the right, one can integrate along any C_- characteristic curve. Then using equation (B.9), we get

(B.12) $$u_b - u_a = \int_a^b \frac{dp}{\rho c} \, .$$

For a rarefaction facing to the left, du can be integrated along a C_+ characteristic which, from equation (B.8), then gives

(B.13) $$u_b - u_a = -\int_a^b \frac{dp}{\rho c} \, .$$

The sound speed of a polytropic* gas is

$$c = \sqrt{\gamma \frac{p}{\rho}}$$

and for an isentropic** process

$$\frac{p}{\rho^\gamma} = \text{constant}.$$

Substituting for ρ and c into the integral of equations (B.12) and (B.13) and performing the integration, we get

(B.14) $$\int_{p_a}^{p_b} \frac{dp}{\rho c} = \frac{2 c_a}{\gamma - 1} \left[\left(\frac{p_b}{p_a} \right)^{\frac{\gamma-1}{2\gamma}} - 1 \right] .$$

By substituting $\mu = \frac{\gamma+1}{\gamma-1}$, the above equation can be written

(B.15) $$\int_{p_a}^{p_b} \frac{dp}{\rho c} = (\mu - 1) c_a \left[\left(\frac{p_b}{p_a} \right)^{\frac{1}{\mu+1}} - 1 \right] .$$

---

*A polytropic gas is one for which the specific heat is constant.
**Isentropic means adiabatic and reversible.

APPENDIX C

THE PROPERTIES OF $\phi(p)$ AND $\psi(p)$

In Chapter II, equation (2.1), the function $\phi_a(p)$ is defined as

$$\phi_a(p) = \frac{(\mu-1)\left(\frac{p}{p_a}-1\right)c_a}{\sqrt{(\mu+1)\left(1+\mu\frac{p}{p_a}\right)}} .$$

The properties of $\phi(p)$ are:

(C.1) $$\phi_b(p_a) = -\phi_a(p_b)$$

Proof: $$\phi_b(p_a) = \left(\frac{p_a}{p_b}-1\right)\frac{(\mu-1)c_b}{\sqrt{(\mu+1)\left(1+\mu\frac{p_a}{p_b}\right)}}$$

$$= \left(1-\frac{p_b}{p_a}\right)\frac{(\mu-1)}{\sqrt{(\mu+1)\left(\mu+\frac{p_b}{p_a}\right)\frac{p_b}{p_a}}}\,\frac{c_b}{c_a}c_a .$$

But

$$\frac{c_b}{c_a} = \sqrt{\frac{T_b}{T_a}} = \sqrt{\frac{\left(\frac{p_b}{p_a}+\mu\right)\frac{p_b}{p_a}}{\left(1+\mu\frac{p_b}{p_a}\right)}} .$$

So

$$\varphi_b(p_a) = \left(1-\frac{p_b}{p_a}\right)\frac{(\mu-1)\,C_a}{\sqrt{(\mu+1)\left(\mu\frac{p_b}{p_a}+1\right)}} = -\varphi_a(p_b).$$

The second property of $\phi(p)$ is that

(C.2) $$\varphi_a(p) \longrightarrow \infty \quad \text{as} \quad p \longrightarrow \infty,$$

which is obvious.

Next

(C.3) $$\frac{d\varphi_a(p)}{dp} \longrightarrow 0 \quad \text{as} \quad p \longrightarrow \infty .$$

Proof:

$$\frac{d\varphi_a(p)}{dp} = \frac{C_a}{p_a}\frac{(\mu-1)}{\sqrt{(\mu+1)\left(\mu\frac{p}{p_a}+1\right)}}$$

$$-\frac{1}{2}C_a\left(\frac{p}{p_a}-1\right)\frac{(\mu-1)}{\sqrt{\mu+1}}\left(\mu\frac{p}{p_a}+1\right)^{-\frac{3}{2}}\frac{\mu}{p_a}$$

which goes to zero as $p^{-1/2}$ as $p \to \infty$.

The fourth property is that

(C.4) $$\varphi_a(0) = -\frac{(\mu-1)C_a}{\sqrt{\mu+1}} .$$

The function $\psi_a(p)$ for rarefaction waves is defined by equation (2.2).

$$\psi_a(p) = (\mu-1)C_a\left[\left(\frac{p}{p_a}\right)^{\frac{1}{\mu+1}} - 1\right] .$$

Some of its properties are the following:

First:

(C.5) $$\psi_b(p_a) = -\psi_a(p_b)$$

Proof:

$$\psi_b(p_a) = (\mu-1)\frac{c_b}{c_a}c_a\left[\left(\frac{p_a}{p_b}\right)^{\frac{1}{\mu+1}} - 1\right].$$

$$\frac{c_b}{c_a} = \sqrt{\frac{T_b}{T_a}} = \sqrt{\frac{p_b}{p_a}\frac{\rho_a}{\rho_b}} = \left(\frac{p_b}{p_a}\right)^{\frac{\gamma-1}{2\gamma}} = \left(\frac{p_b}{p_a}\right)^{\frac{1}{\mu+1}}$$ for isentropic flow.

$$\psi_b(p_a) = (\mu-1)c_a\left[1 - \left(\frac{p_b}{p_a}\right)^{\frac{1}{\mu+1}}\right] = -\psi_a(p_b).$$

Second:

(C.6) $$\psi_a(p) \longrightarrow \infty \quad \text{as} \quad p \longrightarrow \infty.$$

This is obvious.

Third:

(C.7) $$\frac{d\psi_a(p)}{dp} \longrightarrow 0 \quad \text{as} \quad p \longrightarrow \infty.$$

Proof:

$$\frac{d\psi_a(p)}{dp} = (\mu-1)c_a\frac{1}{(\mu+1)}\frac{p^{-\frac{\mu}{\mu+1}}}{p_a^{\frac{1}{\mu+1}}} \longrightarrow 0 \quad \text{as} \quad p \rightarrow \infty,$$

Fourth:

(C.8) $\psi_a(p)$ touches the ψ-axis tangentially at $-(\mu - 1)\, c_a$.

This follows from the above expression for $\dfrac{d\psi_a(p)}{dp}$.

Fifth:

(C.9) $$\psi_a'(p_a) = \varphi_a'(p_a)$$

Proof:

$$\psi_a'(p_a) = \frac{\mu-1}{\mu+1} c_a \frac{p_a^{-\frac{\mu}{\mu+1}}}{p_a^{\frac{1}{\mu+1}}} = \frac{\mu-1}{\mu+1} c_a p_a^{-1}.$$

$$\varphi_a'(p_a) = \frac{c_a}{p_a} \frac{\mu-1}{\sqrt{(\mu+1)(\mu+1)}} = \frac{\mu-1}{\mu+1} c_a p_a^{-1}.$$

APPENDIX D

CALCULATION OF THE H_β INTENSITY BEHIND THE REFLECTED SHOCK

The intensity of the spectral line H_β is proportional to the concentration of neutral hydrogen atoms and to the fraction of hydrogen atoms in the upper level, which is given by the Boltzmann distribution.

$$I_\beta = constant \times N_H \, e^{-\frac{E_4}{kT_5}}, \tag{D.1}$$

where E_4 is the energy of the n = 4 level. The partial pressure of hydrogen atoms behind the first reflected shock wave is

$$\frac{2\delta}{1+\delta} \, p_1 y_{21} y_{52} (1-\alpha_5^H),$$

where δ is the fraction of H_2 added to the neon, y_{21} and y_{52}* are the shock strengths of the primary and reflected shocks, respectively, and α_5^H is the fraction of hydrogen ionized. The number of hydrogen atoms per cc is therefore

$$N_H = \frac{2\delta}{1+\delta} \, \frac{p_1 y_{21} y_{52}}{kT_5} (1-\alpha_5^H), \tag{D.2}$$

where p_1 must be given in dynes per cm^2.

In this calculation it was assumed that the initial pressures p_4 and p_1 were not changed as the fraction of hydrogen added to the neon was varied.

---

* $y_{21} = \frac{p_2}{p_1}$ and $y_{52} = \frac{p_5}{p_2}$. Refer to Figure 1 for the numbering of the regions of the flow.

Typical experimental values of p_4 = 860 psia and p_1 = 0.769 mm Hg were chosen, while the fraction of hydrogen was varied from $\delta = 0$ to $\delta = 0.05$. First of all a family of curves of the flow velocity, u_2, vs the primary shock strength, y_{21}, were plotted for various values of the parameter δ. The Rankine-Hugoniot equation

$$X_{21} = \frac{4y_{21}+1}{y_{21}+4-2\delta\left(\frac{\Phi_{H_2}}{T_1}-1\right)}$$

and the equation for the flow velocity

$$u_2^2 = R_1T_1\left(\frac{X_{21}-1}{X_{21}}\right)(y_{21}-1)$$

were used for this calculation. For the Rankine-Hugoniot equation above it was assumed that the hydrogen is completely dissociated but that no ionization takes place behind the primary shock wave. The intersections of these curves with the u_3-vs-p_3 curve for the cold flow gives the shock strengths and flow velocities for different values of the parameter, δ. It would have been unrealistic to plot the u_3-vs-p_3 curve for the cold flow according to the ideal theory because the experiments have shown that the initial pressure ratio Z may be several times larger than the theoretical value for a given shock strength. Therefore, the experimental data of M_s vs Z were used to construct a u_3-vs-p_3 curve in the region of interest. From the primary shock strengths the density ratios were calculated, using the Rankine-Hugoniot equation given above and the temperatures behind the primary shock were obtained from the relation

$$T_2 = \frac{T_1}{1+\delta}\,\frac{y_{21}}{x_{21}}\,.$$

The calculation of the temperatures and pressures behind the first reflected shock wave was simplified by neglecting the effect of ionization on the hydrodynamics. The error thus introduced is not very large since less than 1/3% of the atoms are ionized. A further simplification was to use the same reflected shock strength, y_{52}, and hence the same temperature ratio, T_5/T_2, for all values of the parameter, δ. The equations used were

$$y_{52} = \frac{6y_{21}-1}{4+y_{21}} \quad \text{and} \quad \frac{T_5}{T_2} = \frac{y_{52}(y_{52}+4)}{4y_{52}+1}\,.$$

The fractions of hydrogen ionized were calculated, using the Saha equation with the values of y_{52} and T_5 found above. Then, with all the hydrodynamic variables known, the H_β intensities were calculated, using equations (D.2) and (D.1) for the values of δ from 0 to 0.05. The results are given in the curve of Figure 34.

BIBLIOGRAPHY

1. Paul Vieille, "Sur les discontinuités produites par la détente brusque des gas comprimés," Comptes Rendus, 129, 1228-1230 (1899).

2. K. Kobes, "Die Durchschlagsgeschwindigkeit bei den Luftsauge - und Druckluftbremsen," Zeitschrift des Osterreichischen Ingenieur - und Architekten - Vereines, 62, 558 (1910).

3. H. Schardin, "Bemerkungen zum Druckausgleichvorgang in einer Rohrleitung," Physik. Zeit., 33, 60 (1932).

4. W. Payman and W. F. C. Shepherd, "Explosion waves and shock waves IV. The disturbance produced by bursting diaphragms with compressed air," Proc. Roy. Soc. London, A-186, 293-321 (1946).

5. George T. Reynolds, "A Preliminary Study of Plane Waves Formed by Bursting Diaphragms in a Tube," OSRD Report No. 1519, June, 1943.

6. Lincoln G. Smith, "Photographic Investigation of the Reflection of Plane Shocks in Air," OSRD Report No. 6271, November, 1945.

7. C. W. Mautz, F. W. Geiger, and H. T. Epstein, "On the Investigation of Supersonic Flow Patterns by Means of the Shock Tube," Phys. Rev., 74, 1872 (1948).

8. C. W. Mautz, "The Use of the Shock Tube in the Production of Uniform Fields of Transsonic and Supersonic Flow," Thesis, Univ. of Mich., 1949.

9. F. W. Geiger, "On the Shock Tube as a Tool for the Investigation of Flow Phenomena," Thesis, Univ. of Mich., 1949.

10. Russell E. Duff, "The Use of Real Gases in a Shock Tube," Thesis, Univ. of Mich., 1951.

11. Robert N. Hollyer, Jr., "A Study of Attenuation in the Shock Tube," Thesis, Univ. of Mich., 1953.

12. R. N. Hollyer, Jr., A. C. Hunting, Otto Laporte, E. H. Schwarcz, and E. B. Turner, "Luminous Effects in the Shock Tube," Phys. Rev., 87, 911 (1952).

13. R. N. Hollyer, Jr., A. C. Hunting, Otto Laporte, and E. B. Turner, "Luminosity Generated by Shock Waves," *Nature*, *171*, 395 (1953).

14. E. L. Resler, Shao-Chi Lin, and Arthur Kantrowitz, "The Production of High Temperature Gases in Shock Tubes," *Jour. Applied Physics*, *23*, 1390 (1952).

15. G. Shreffler and R. H. Christian, "Boundary Disturbances in High Explosive Shock Tubes," *Jour. Applied Physics*, *25*, 324 (1954).

16. Richard G. Fowler, William R. Atkinson, and Luther W. Marks, "Ion Concentrations and Recombination in Expanding Low Pressure Sparks," *Phys. Rev.*, *87*, 966 (1952).

17. H. E. Petschek, Peter H. Rose, Herbert S. Glick, Ann Kane, and Arthur Kantrowitz, "Spectroscopic Studies of Highly Ionized Argon Produced by Shock Waves," *Jour. Applied Physics*, *26*, 83 (1955).

18. Shao-Chi Lin, E. L. Resler, and Arthur Kantrowitz, "Electrical Conductivity of Highly Ionized Argon Produced by Shock Waves," *Jour. Applied Physics*, *26*, 95 (1955).

19. A. C. Kolb, "Broadening of Hydrogen Lines by Ions and Electrons," *Bull. Amer. Phys. Soc. II*, *1* (1956).

20. L. Tonks and I. Langmuir, *Phys. Rev.*, *33*, 195 (1929)

21. Lawrence H. Aller," The Luminous Shock Tube, A Tool for Experimental Astrophysics, "*Sky and Telescope*, XIV, 2, December, 1954.

22. R. Courant and K. O. Friedrichs, *Supersonic Flow and Shock Waves*, Interscience Publishers, 1948.

23. J. von Neumann, "Progress Report on the Theory of Shock Waves," OSRD Report No. 1140 (1943).

24. Shao-Chi Lin, "Electrical Conductivity of an Ionized Gas Produced by Strong Shock Waves," Thesis, Cornell Univ., 1952.

25. D. H. Menzel, *Proc. Natl. Acad. Sci.*, *19*, 40 (1933).

26. John W. Bond, Jr., "The Structure of a Shock Front in Argon," Los Alamos Scientific Laboratory, Report LA-1693, 1954.

27. L. H. Aller, *The Atmospheres of the Sun and Stars*, Ronald Press, 1953.

28. W. Döring, "Die Geschwindigkeit und Structur von intensiven Stosswellen in Gasen," *Annalen der Physik*, *5*, 133-150 (1949).

29. Otto Laporte and E. B. Turner, "On the Interaction of Two Plane Shocks Facing in the Same Direction," *Jour. Applied Physics*, *25*, 678 (1954).

30. Richard F. Jarrell, "Stigmatic Plane Grating Spectrograph with Order Sorter," *Jour. Opt. Soc. Amer.*, *45*, 259 (1955).

31. H. E. Petschek, *Phys. Rev.*, *84*, 614 (1951).

32. R. J. Rosa, "Shock Wave Spectroscopy," *Phys. Rev.*, *99*, 633 (1955).

33. E. B. Turner, "Radiation from a Strong Shock Front in Krypton," *Phys. Rev.*, *99*, 633 (1955).

34. E. B. Turner, "Radiation from a Strong Shock Front in Krypton," Report No. 2189-1-T, Engineering Research Institute, Univ. of Mich.

35. H. M. Foley, *Phys. Rev.*, *69*, 616 (1946).

36. E. Lindholm, *Arkiv Mat., Astron. Fysik*, *28B* (1942).

37. L. Minnhagen, "The Stark Effect in Argon I," *Arkiv für Fysik*, *1*, 425-457 (1950).

38. H. A. Lorentz, *Proc. Acad. Sci. (Amsterdam)*, *8*, 591 (1906).

39. V. Weisskopf, *Z. Physik*, *80*, 423 (1933).

40. M. Baranger, Abstract of Paper, *Phys. Rev.*, *91*, 436 (1953).

41. C. E. Moore, "Atomic Energy Levels, Vol. 1," Circular 467, U. S. Dept. of Commerce, Natl. Bur. of Std.

42. W. H. Harkness and J. F. Heard, *Proc. Roy. Soc. of London*, *139*, 416 (1933).

43. J. Stark, *Berl. Akad. Wiss.*, *40*, 932 (1913).

44. P. S. Epstein, *Ann. der Physik*, *50*, 489 (1916); also, *Physik. Zeit.*, *17*, 148 (1916).

45. K. Schwarzschild, *Sitzungsber. Berl. Akad. Wiss.*, 1916, p. 548.

46. E. Schrödinger, *Annalen der Physik*, *80*, 467 (1926).

47. J. Holtsmark, *Z. Physik*, *20*, 162 (1919); *ibid.*, *25*, 73 (1924); *Annalen der Physik*, *58*, 577 (1919).

48. P. Schmaljohann, Unpublished State Examination Work, Kiel, 1936. See A. Unsold, *Physik der Stern-atmospheren*, Berlin, 1938.

49. A. Pannekoek and S. Verwey, *Proc. Amsterdam Akad.*, *38*, 2 (1935).

50. S. Verwey, "The Stark Effect of Hydrogen in Stellar Spectra," Dissertation, Amsterdam, 1936.

51. C. DeJager, *Rech. Astron. Obs. Utrecht*, *13*, 1 (1952).

52. L. R. Doherty, Unpublished Work, Univ. of Mich., 1956.

53. H. M. Crosswhite and G. H. Dieke, "Simplified Techniques for Calibrating Photographic Emulsions," Bumblebee Series, Report No. 202, Johns Hopkins Univ., September, 1953.

54. B. Lewis and G. von Elbe, "Heat Capacities and Dissociation Equilibria," *Jour. Amer. Chem. Soc.*, *57*, 612 (1935).

55. H. Griem, "Starkeffekt-Verbreiterung der Balmer-Linien bei grossen Electronendichten," *Z. Physik*, *137*, 280 (1954).

56. A. C. Kolb, Ph.D. Thesis (in preparation), Univ. of Mich.

57. D. R. Inglis and E. Teller, *Astrophys. Jour.*, *90*, 439 (1939).

58. G. Jürgens, *Z. Physik*, *134*, 21 (1952).

59. G. Elstie, J. Jugaku, and L. H. Aller, "Theoretical Line Intensities and the Spectrum of Tau Scorpii," *Publ. of the Astron. Soc. of the Pacific*, *68*, 23 (1956).